ABSTRACT

Title of dissertation: UNUSUAL ELECTRONIC TRANSPORT AND MAGNETISM IN TITANIUM OXIDE BASED SEMICONDUCTORS AND METALS

Shixiong Zhang, Doctor of Philosophy, 2007

Dissertation directed by: Professor T. Venky Venkatesan
Department of Physics

The main objective of this thesis was to explore the structural, electrical, magnetic and optical properties of titanium based novel oxide thin films, such as transparent conducting oxides (TCOs) and diluted magnetic semiconductors (DMSs), so as to be able to realize optoelectronics and spintronics applications.

I demonstrated that niobium doped titanium dioxide (TiO_2) in its epitaxial anatase phase grown at certain condition is an intrinsic transparent conducting oxide, with both its conductivity and transparency comparable to that of the commercial transparent electrode In-Sn-O being widely used in current optoelectronic devices.

I investigated the growth parameter dependence of structure and conductivity of this material. It was found that the growth temperature is a crucial parameter for the structural quality as well as the electron mobility, while the oxygen partial pressure is essential for the conduction electron concentration. The excellent

conductivity of niobium doped TiO_2 should be attributed to the extremely high solubility of niobium in the TiO_2 matrix as well as a very shallow donor level created in the TiO_2 band gap.

I investigated several important oxide based DMS systems, such as niobium and cobalt dual doped TiO_2, transition metal (TM) element doped $SrTiO_3$ etc. I found that niobium dual doping is an effective way to introduce carriers into the classical Co: TiO_2 system, which provides the feasibility of studying the RKKY interaction in this system by chemical doping. Our detailed characterization of TM doped $SrTiO_3$ questioned the intrinsic nature of the ferromagnetism observed by other groups.

By a systematic study of Hall effect on superparamagnetic Co-(La,Sr)TiO_3 thin films, I was able to demonstrate that the magnitude of the anomalous Hall effect is a way to distinguish between intrinsic and extrinsic DMS.

A Kondo effect was observed in niobium doped TiO_2 grown at certain condition. The origin of magnetic moments in this system was suggested to be from the cation vacancy defects. This observation of defect magnetism in conventional non-magnetic TiO_2 may shed light on the occurrence of ferromagnetism in oxide diluted magnetic semiconductors.

UNUSUAL ELECTRONIC TRANSPORT AND MAGNETISM IN TITANIUM OXIDE BASED SEMICONDUCTORS AND METALS

by

Shixiong Zhang

Dissertation submitted to the Faculty of the Graduate School of the
University of Maryland, College Park in partial fulfillment
of the requirements for the degree of
Doctor of Philosophy
2007

Advisory Committee:

Professor T. Venky Venkatesan, Chair/Advisor
Professor Richard L. Greene
Professor Lourdes G. Salamanca-Riba
Professor Christopher Lobb
Professor J. Robert Anderson

Acknowledgement

Many people have helped me during the entire process of graduate school. I would like to extend my gratitude to all of them.

First and foremost, I would like to thank my advisor Prof. T. Venky Venkatesan. With his outstanding guidance and encouragement, and always valuable suggestions, I had great opportunities to investigate the physical properties of functional oxide thin film systems. In addition to physics, Venky has taught me many things about life, which I think will be very useful to my future career.

Dr. Satish B. Ogale is my initial mentor who I worked the most closely with. He is an essential part of my education who has advised and guided my scientific growth in these three years. He has been an invaluable resource for me.

Prof. Richard L. Greene is the one who initially introduced me into Venky's group. He is a very nice person and has given me almost unlimited access to his lab facilities. Without his help, many of my projects could not have been finished on time.

I thank Professors Anderson, Lobb and Salamanca-riba for taking interest in my work and serving on my committee. I would also like to thank the entire faculty and staff of the CSR (now as CNAM) at UMD. I highly acknowledge CSR for the financial support.

I owe a lot to my lab-mates, Sanjay Shinde, Darshan Kundaliya, Sankar Dhar, Wegdan Ramadan, Betsy Pugel, Greg Glangham and Arun Lukyx. Sanjay taught me a lot of physics and material science. He gave me many useful suggestions on my

work even after he left Venky's group. Darshan is the one who I also worked closely with. I learnt many technique skills from him. I thank Sankar for his assistance in RBS measurements. I would like to thank Betsy for sharing her thesis writing experience with me.

I would like to thank my collaborators, Darren Young and Prof. Salamanca-riba at material science, Lianfeng Fu and Prof. Nigel Browning at University of California, Davis for their help on TEM and EELS meausurements. I thank Xingyu Gao and Prof. Lee at National University of Singapore for XPS, UPS and XAS measurements.

I would also like to acknowledge several Chinese fellows in the center. Weiqiang Yu helped me a lot on the electronic transport measurements, and the discussion with him is a very important source to understand physics. Bing Liang gave me much of her assistance on SQUID measurements. I could easily get help from Pengcheng Li, Hua Xu and Zhengli Li whenever I had trouble with the experiment techniques.

I enjoyed my discussion on material growth with several graduate fellows, Shengqiang Ren, Sung Hwan Lim, Yi Qi, Shige Fujimoto, and Makoto Murakami, all from material science department. I thank Josh Higgins for helping me with PPMS measurements and sharing his thesis with me. I thank James Tse for helping me understand the physics behind spin Hall effect as well as anomalous Hall effect.

I thank my internship manager Eric Granstrom, mentor Konstantin R. Nikolaev at seagate for giving me the opportunity to work in the industrial environment. I thank my friend Jenny Gao and Paul Henny for helping me understand the physics and applications of CPP-spin valve and TMR stacks. I thank Wei Tong (one of my

best friends) currently at Colorado State University for his continuous help.

I would like to thank my girlfriend Meijuan and my family. Their love is the most important support in my life.

Table of Contents

List of Figures

List of Abbreviations

TCO	transparent conducting oxide
DMS	diluted magnetic semiconductor
VB	valence band
CB	conduction band
DOS	density of states
PDOS	partial density of states
SP	semiconductor photocatalyst
FPD	flat panel display
LED	light emitting diode
ITO	In-Sn-O
STO	$SrTiO_3$
NTO	Nb:TiO_3
LAO	$LaAlO_3$
XRD	x-ray diffraction pattern
FWHM	full width at half maximum
AFM	atomic force microscopy
TEM	transmission electron microscopy
RBS	Rutherford backscattering
EDP	electron diffraction patterns
PPMS	physical property measurement system
RT	room temperature
CBM	conduction band minimum
VBM	valence band maximum
PLD	pulsed laser deposition
XPS	x-ray photoelectron spectroscopy
FM	ferromagnetism
GMR	giant magnetoresistance
MTJ	magnetic tunnel junction
MRAM	magnetic random access memory
FET	field effect transistor
RKKY	Ruderman-Kittel-Kasuya-Yosida
EELS	electron energy loss spectroscopy
LSTO	(La, Sr)TiO_3
NSTO	Nb: $SrTiO_3$
MTE	magnetic transition element
SPM	superparamagnetism
ZFC	zero field cooled
FC	field cooled
ZFCM	zero field cooled magnetization
FCM	field cooled magnetization

SSG	super-spin glass
AHE	anomalous Hall effect
WLE	weak localization effect
MR	magnetoresistance
MPMS	magnetic property measurement system
SQUID	superconducting quantum interference devices
DC	direct current
UHV	ultra-high vacuum
UV	Ultraviolet

Chapter 1

Introduction

This thesis deals with the fundamental electronic transport and magnetic properties of titanium oxide based semiconductors and metals (here as degenerate semiconductors). In Chapter 1, I present a brief introduction to semiconductors and titanium dioxide. In Chapters 2 and 3, I show the detailed electronic transport of the titanium oxide based transparent conducting oxides (TCO). In Chapter 4, I give an introduction to diluted magnetic semiconductors. In Chapters 5, 6, 7, and 8, I focus on both the electronic transport and magnetism of the titanium oxide based DMSs. Finally, in Chapter 9, I give a summary of this thesis and suggest some future work.

1.1 A Brief Introduction to Semiconductor Physics

Semiconductors are a class of materials which have electrical conductivity in between that of a metal ($> 10^4 Scm^{-1}$) and that of an insulator ($< 10^{-10} Scm^{-1}$)[1, 2]. However this definition of semiconductor is not completed. Another definition is made by considering the existence of a gap between occupied and empty states: no such an energy gap exists in a metal (Fig. 1.1 (a)); an energy gap with its width less than 4 eV exists in a semiconductor (Fig. 1.1 (b)); an energy gap with its width larger than 4 eV exists in an insulator (Fig. 1.1(c)).

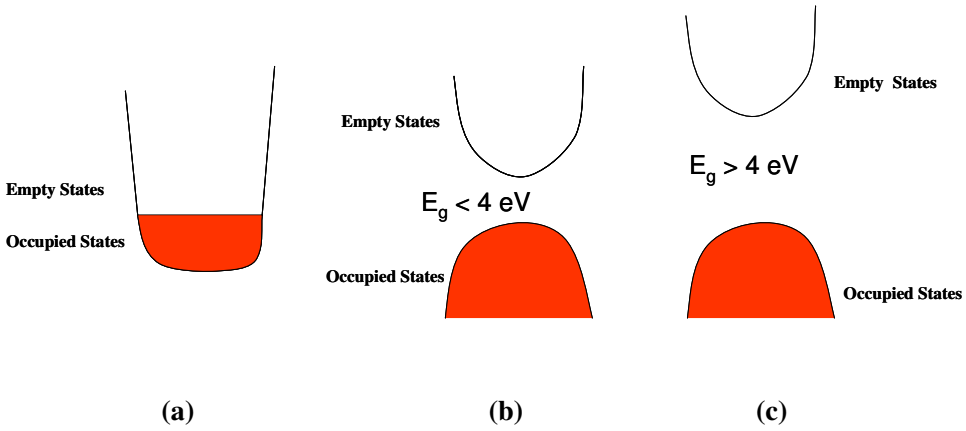

Figure 1.1: Schematic band structures of (a) metal, (b) semiconductor, and (c) insulator.

The energy of free electrons is given by[3]

$$E = \frac{\hbar^2 k^2}{2m_0} \tag{1.1}$$

where $\hbar = 1.05 \times 10^{-34} Js$ is the Dirac's constant, k is the electron wave vector, and $m_0 = 9.11 \times 10^{-31} kg$ is the electron mass. The energy of an electron in a semiconductor near the maximum or minimum of the band structure can be expanded in a power series of k with the leading term of the order k^2 (the k-term vanishes near a maximum or minimum). Therefore, we can describe the electrons in a semiconductor as free electrons with an effective mass m^* of[1, 2]:

$$m^* = \hbar^2 \frac{1}{d^2E/dk^2} \mid_{dE/dk=0} \tag{1.2}$$

In semiconductors at zero temperature, the conduction band is completely empty and the valence band is completely filled. As in an empty or full filled band, the electrons do not carry any current, there isn't any conductance in semiconductors at T = 0 K. While with the increase of temperature, the electrons at the top

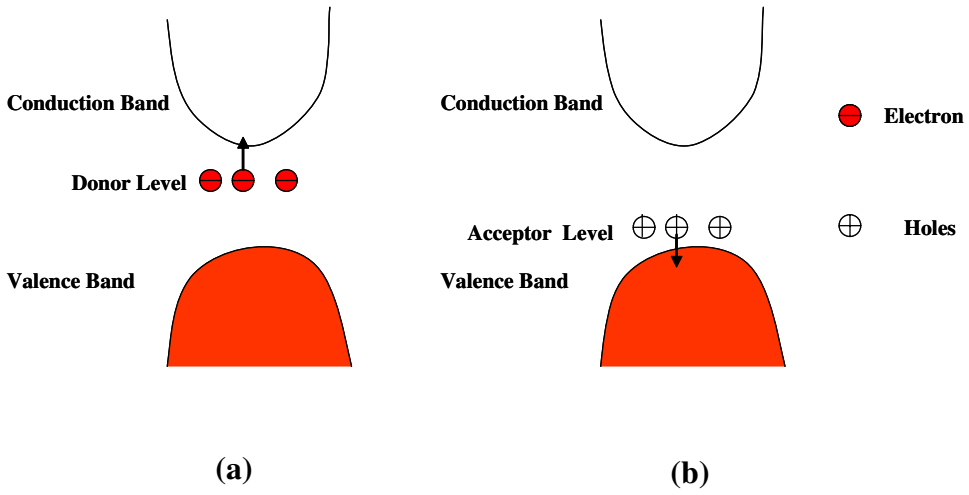

Figure 1.2: Schematic band structure of a semiconductor with (a) n-type doping, and (b) p-type doping.

of valence band are thermally excited to the bottom of conduction band, leaving empty states in the valence band. The valence band with some empty states can be considered as a full filled valence band along with some positive charges (+ e), called 'holes', occupying the top of the valence band. Therefore, conductance is induced by the motion of electrons in the conduction band and the holes in the valence band.

Another effective way to introduce charge carriers (electrons or holes) is to dope some impurities into the host semiconductor. The number of outer shell electrons of the impurity atoms should be different from that of the constituent atoms. If the impurity atoms have more outer shell electrons, they will provide or 'donate' extra electrons in the semiconductor, accordingly, they are called n-type dopants or 'donors'. While if the impurity atoms have less outer shell electrons, they will require or 'accept' electrons from the host atoms, or they provide extra holes in the semiconductor, thereby they are called p-type dopants or 'acceptors'. From

a band structure point of way, n-type dopants create donor impurity levels below the bottom of the conduction band, while p-type dopants create acceptor impurity levels above the top of the conduction band (Fig. 2). Due to thermal activation, electrons in the donor levels will be excited to the conduction band, or the holes in the acceptor levels will be excited to the valence band, which can give rise to a large number of charge carriers.

Besides the number of charge carriers, the mobility of carriers determines the conductivity as well. In a simple Drude model, the conductivity is written as[1, 2]

$$\sigma = ne\mu_e + pe\mu_p \tag{1.3}$$

where n and p are the electron and hole densities; respectively, μ_e and μ_p are the electron and hole mobilities, respectively. The mobility can be written as[3]

$$\mu = \frac{e < \tau >}{m^*} \tag{1.4}$$

where $< \tau >$ is the average relaxation time.

More details about the specific physics of semiconductor related to our work are presented in Chapters 3 and 4. In the next two sections, I give an introduction to the fundamental properties and potential applications of titanium dioxide as this material is the host compound of the novel semiconductors we investigated in this work.

1.2 Fundamental Physical Properties of TiO_2

1.2.1 Crystalline Structural Polymorphs

In nature, titanium dioxide (TiO_2) forms in three distinct structural polymorphs: rutile, anatase and brookite, among which, rutile is the most stable and well studied one[4]. The rutile structure is very simple as illustrated in Fig. 1.3 (a). It is characterized by the tetragonal space group $P4_2/mnm$[4, 5]. The unit cell contains two TiO_2 units with Ti at (0,0,0), (1/2 , 1/2 , 1/2), and O at ± (u,u,0), ± (u+1/2 , 1/2-u, 1/2). The lattice parameters are: a=b=4.587 $\AA$, c=2.954 $\AA$, and u=0.305 $\AA$[6, 7, 8]. Each Ti ion is octahedrally coordinated to six O ions and this TiO_6 octahedron is distorted. The four equatorial O ions are in the plane of (110). The equatorial Ti-O bond length is $\sim$ 1.95 $\AA$, while the apical Ti-O bond length is $\sim$ 1.98 $\AA$. The octahedra form chains that share edges along the [001] direction and share vertices in the (001) plane.

The anatase structure, as shown in Fig. 1.3 (b), belongs to the tetragonal space group $I4/amd$[5, 9]. The unit cell contains two TiO_2 units. The Ti ions are at (0, 0 ,0) and (0, 1/2, 1/4) and the O ions are at (0, 0, u), (0, 0,-u), (0, 1/2, u+1/4) and (0, 1/2, 1/2-u). The lattice parameters are: a=b=3.782 $\AA$, c = 9.502 $\AA$, and u = 0.208 $\AA$[6, 7, 8]. Similar to that in rutile structure, each Ti ion is octahedrally coordinated to six O ions. The octahedrons are also distorted, with the short Ti-O bond length of $\sim$ 1.93 $\AA$ and long bond length of $\sim$ 1.98 $\AA$, and they form zigzag chains along the [100] and [010] directions.

The brookite phase of TiO_2 is very unstable and has a complex structure as

shown in (Fig. 1.3 (c))[5, 9]. It is characterized by the orthorhombic space group P*bca*. The Ti ion is octahedrally coordinated to six O ions as well. In contrast to that of rutile and anatase, the Ti-O bond length in the octahedron is different from each other and ranges from 1.87 to 2.04 $\mathring{A}$. The O-Ti-O bond angle ranges from 77^0 to 105^0.

1.2.2 Electronic Structure

The initial theoretical calculations[10, 11, 12, 13, 14] on the electronic properties of TiO_2 were mainly on its rutile phase, since rutile is the easiest formed phase and its structure is the simplest and best-known. A detailed theoretical study on all of these three phases was done by S.-D. Mo and W. Y. Ching [9]using a first principle orthogonalized linear-combination-of-atomic-orbitals (OLCAO) method. Fig. 1.4 shows their calculated band structures along the symmetry lines of the Brillouin zone. For rutile, the top of valence band (VB) and the bottom of conduction band (CB) both locate at Γ, and the band gap is $\sim$ 1.78 eV. For anatase, the top of VB locates at M, while the bottom of CB locates at Γ. The calculated indirect band gap is $\sim$ 2.04 eV, which is 0.26 eV larger than that of rutile phase. For brookite, both the top of VB and bottom of CB are at Γ and the calculated direct band gap is $\sim$ 2.20 eV.

Mo and Ching also calculated the total density of states (DOS) and partial density of states (PDOS) for each component (O_{2s}, O_{2p} and Ti_{3d}) of TiO_2 (as shown in Fig 1.5). For rutile, the upper VB mainly consists of O_{2p} with a width of $\sim$ 6.22

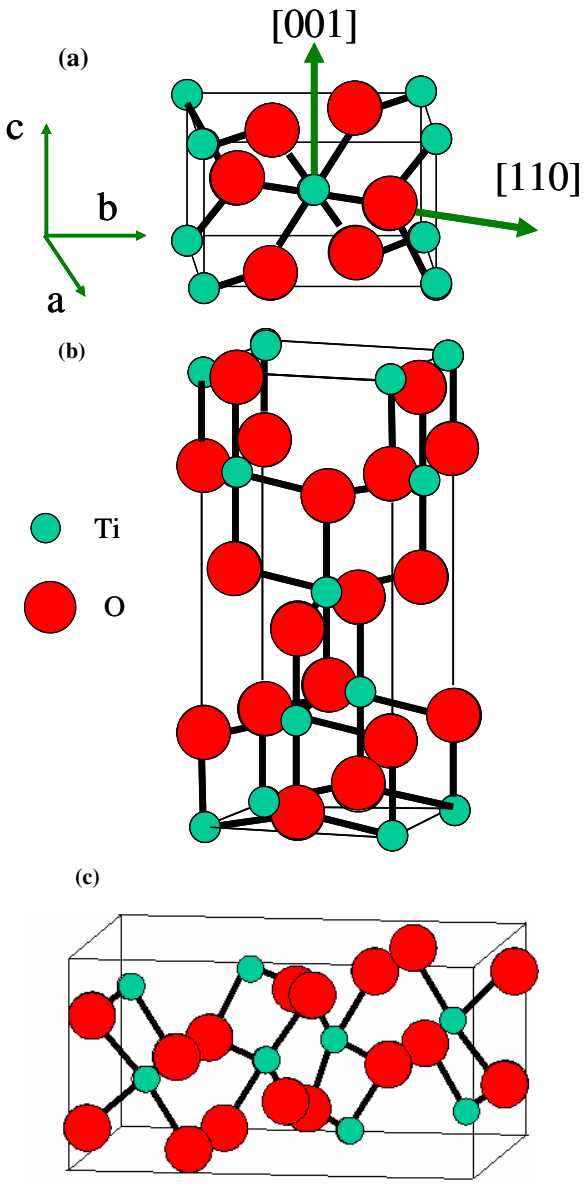

Figure 1.3: The crystal structures of (a) rutile; (b) anatase; and (c) brookite.

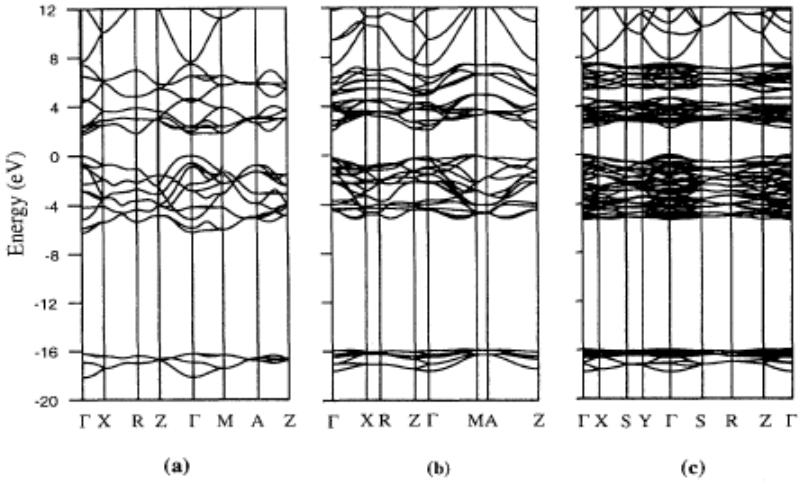

Figure 1.4: The calculated band structures of (a) rutile; (b) anatase; and (c) brookite [9].

eV and the lower VB consists of O_{2s} with a width of $\sim$ 1.94 eV. The lowest CB is mainly composed of Ti_{3d} with a width of 5.9 eV. These Ti_{3d} bands are characterized into two sets of bands, one of which is from the hybridized states of t_{2g} and another one is from e_g. There is essential hybridization between O_{2p} and Ti_{3d} in both the VB and CB region. For anatase, the general features are similar to that of rutile, though the upper VB has a width of 5.17 eV and the lower VB has a width of 1.76 eV, both of which are narrower than the same of rutile. there is significant hybridization between O_{2p} and Ti_{3d} bands as well. The DOS and PDOS of Brookite caculated by Mo and Ching show very close band structure to that of anatase.

From Mo and Ching's calcualtion, it appears that rutile and anatase are supposed to have similar electrical properties except that anatase has a slightly larger band gap ($\sim$ 0.2 eV). Indeed, the X-ray absorption experiment shows that rutile has

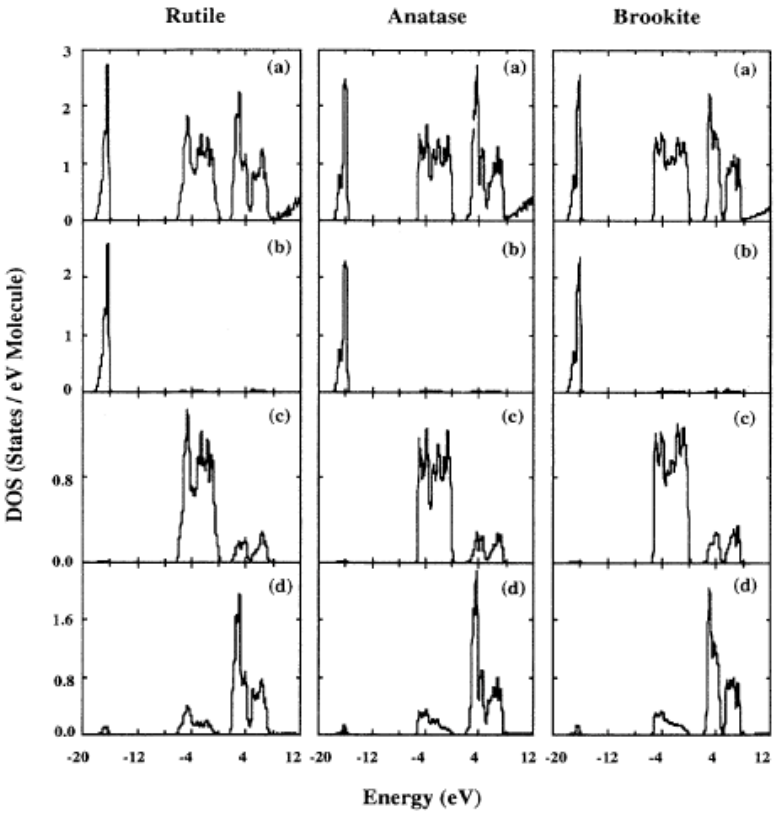

Figure 1.5: The calculated total and partial density of states (DOS) for three different phases of TiO_2. (a)total; (b)O_{2s}; (c)O_{2p} and(d)Ti_{3d} [9].

a direct band gap of $\sim$ 3.0 eV[15], while the anatase has a band gap of 3.2 eV [16] (the relative smaller band gap of theoretical calculation is due to the well-known shortcoming of local density approximation[17]). However, significant differences of electrical properties were found between these two phases[16, 18, 19, 20, 21], for example, a very shallow donor level and a much higher electron mobility were found in anatase[20], and the nature of exciton states of antatse is self trapped instead of free as in rutile[20]. These differences require further investigation of the band structure of rutile and anatase.

1.3 Potential Applications of TiO_2

Titanium dioxide is probably one of the most important oxides having great applications, i.e. as semiconductor photocatalyst[22, 23], additive to pigments[24], sensor devices and novel solar cells[25]. Fig. 1. 6 shows how a semiconductor photocatalyst (SP) works. Due to optical excitation, an electron is activated from the valence band to the conduction band of a semiconductor, meanwhile a hole is created in the valence band. These excited carriers diffuse to the surface and chemically react with the surrounding medium, for example, electrons react with oxygen to form O_2^- and holes react with surface hydroxyl groups to form OH radicals. These radical species then attack and decompose the nearby organic molecules. This process is commonly applied to photocatalytic oxidation, hydrogen transfer, water detoxification, air purification and other environmental applications[26]. The anatase TiO_2 was discovered as an excellent photocatalyst in 1972 [22], and has

become the most important semiconductor photocatalyst. Compared to other SPs, TiO_2 has great advantages, such as non-toxicity, high photo-activity, mechanical stability, low cost and favorable overlap with the ultra-violet portion of the solar spectrum.

Another important function of TiO_2 is as an essential material in novel solar cell device, i. e. *Grätzel* cell, which is named after its inventor *Grätzel* cell[25]. Fig. 1. 7 shows how a Gratzel cell works. The porous TiO_2 nano-particles with a large surface area are coated with dye molecules which are able to absorb at a wide range of wavelengths given off by sunlight. These particles are then placed between two transparent conducting electrodes in a redox electrolyte solution(iodide/tri-iodide ions or I^-/I_3^-). when excited by a photon of light, the electron escapes from the dye molecule to the TiO_2 particle and further diffuses into one of the electrodes. The oxidized dye can be reduced to its original state by regaining electrons from iodide ion, with the iodide ion being oxidized to tri-iodide ion. Electrons from the counter electrodes are able to reduce the tri-iodide ions back to their iodide state. After this cycle, the system returns to its original form and is then ready for the next cycle. The greatest advantage of this dye-sensitized solar cell is the low cost of the widely available TiO_2 material and the electrolyte.

Titanium dioxide is also an important pigment widely used nowadays due to its excellent whiteness and opacity. The stoichiometric TiO_2 is an insulator, while with oxygen deficiency, it becomes a semiconductor and its conductivity strongly depends on the oxygen content which is sensitive to the atmosphere. Therefore titanium dioxide has been used in gas sensors to measure the oxygen content in the

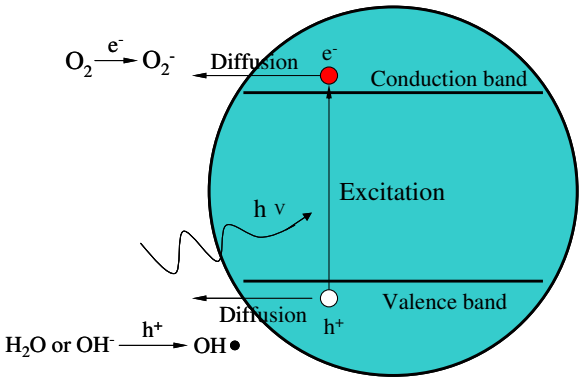

Figure 1.6: A skematic picture shows how semiconductor photocatalyst (SP) works

atmosphere.

The above applications are mainly based on the nano-particle form of TiO_2. Recently, there have been a lot of interests in investigating the thin film properties of TiO_2. The objective of this thesis is to study the structural, magnetic and electronic transport properties of TiO_2 based semiconducting and metallic thin films with a goal of realizing optoelectronics and spintronics applications.

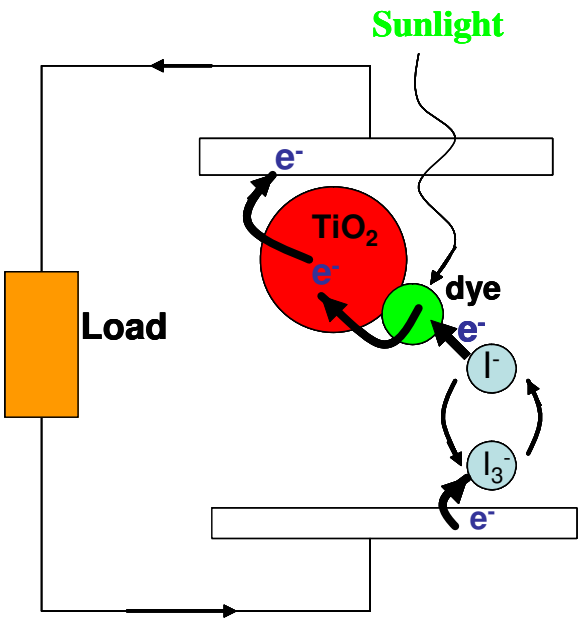

Figure 1.7: A skematic picture shows how a typical Gratzel cell works

Chapter 2

Niobium doped TiO_2: Transparent Conducting Anatase vs Highly Resistive Rutile

2.1 Introduction

2.1.1 Transparent Conducting Oxides

Transparent conducting oxides (TCOs) are a class of oxides which have transmittance as high as 80% in the visible range and resistivity as low as 10^{-3} Ω cm at room temperature[27, 28]. In the field of electronics, TCOs have been widely used as transparent electrodes (Fig. 2.1(a)) for solar cells and most optoelectronic devices such as flat panel displays (FPDs) (Fig. 2.1 (b)) and light emitting diodes (LEDs) (Fig. 2.1 (c))[27, 28, 29, 30].

Unfortunately, most of the normal metals are usually not transparent because there is a large number of conduction electrons in these materials, and the energy of light can be absorbed by the conduction electrons, hence very little light could pass through them. To avoid absorbing light, the band gap of a material should be larger than the energy of the photon. The energy of visible light is about 3 eV. Therefore the band gap of a material should be no less than 3 eV in order to be transparent. These types of materials are usually called wide-band gap semiconductors. Without extrinsic doping, only very few electrons are excited into the conduction band via

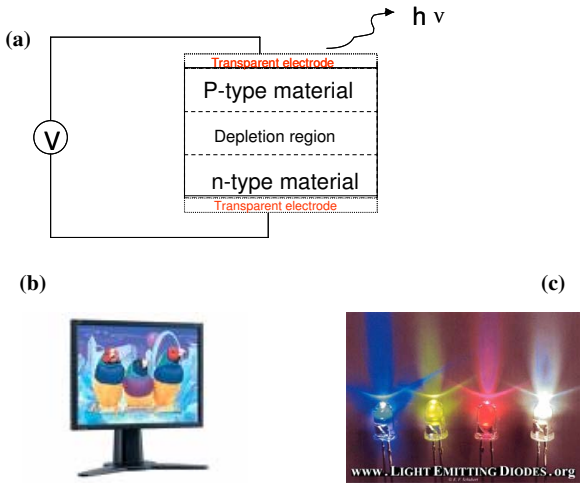

Figure 2.1: (a) A schematic picture shows TCOs as transparent electrodes in optoelectronic devices[31]; (b) a flat panel display; (c) light emitting diodes[32].

thermal activation, hence its conductivity is rather poor. In general, various types of extrinsic doping are employed to improve the conductivity of semiconductors. The dopants chosen are either shallow donors which can produce additional electrons into conduction band, or acceptors which can produce additional holes into valence band. To realize a resistivity as low as 10^{-3} Ω cm, the density of conduction carriers (electrons or holes) usually should reach $\sim 10^{20}$ cm^{-3}[30].

The current commercial transparent conducting oxide used for most transparent electrode applications is tin doped indium oxide(In-Sn-O, or ITO)[27, 28]. However, ITO may not be able to satisfy the demands in the speedy development of future optoelectronic devices since indium, the principle material of ITO, due to its low terrestrial abundance has become very costly. Therefore, the search for a new type of TCO material has become extremely urgent. Indeed, a lot of efforts

have been dedicated in search for novel TCOs. Table 2.1 shows various types of new TCO materials discovered during the past decades[30].

Table 2.1 Recently discovered TCO materials for transparent electrodes [30]

Material	Dopant or Compound
SnO_2	Sb, F, As, Nb, Ta
In_2O_3	Sn, Ge, Mo, F, Ti, Zr, Hf, Nb, Ta, W, Te
ZnO	Al, Ga, B, In, Y, Sc, F, V, Si, Ge, Ti, Zr, Hf
CdO	In, Sn
$ZnO\text{-}SnO_2$	Zn_2SnO_4, $ZnSnO_3$
$ZnO\text{-}In_2O_3$	$Zn_2In_2O_5$, $Zn_3In_2O_6$
$In_2O_3\text{-}SnO_2$	$In_4Sn_3O_{12}$
$CdO\text{-}SnO_2$	Cd_2SnO_4, $CdSnO_3$
$CdO\text{-}In_2O_3$	$CdIn_2O_4$
$MgIn_2O_4$	
$GaInO_3$, $(Ga, In)_2O_3$	Sn, Ge
$CdSb_2O_6$	Y
$ZnO\text{-}In_2O_3\text{-}SnO_2$	$Zn_2In_2O_5\text{-}In_4Sn_3O_{12}$
$CdO\text{-}In_2O_3\text{-}SnO_2$	$CdIn_2O_4\text{-}Cd_2SnO_4$
$ZnO\text{-}CdO\text{-}In_2O_3\text{-}SnO_2$	
InGa(ZnO)	

2.1.2 Mott Transition

As we discussed above, to introduce a large number of carriers into a wide-band gap semiconductor, an extrinsic doping with shallow donors or acceptors is required. Since 1950s, It has been noticed that when the concentration of shallow impurities in a semiconductor increases to a critical value, an abrupt semiconductor-to-metal transition occurs. This transition was named "Mott transition" later because of the significant contribution of N. F. Mott in explaining the underlying physics of this phenomenon[33].

Mott pointed out three main features of this transition(n-type semiconductors for example)[33, 34]:

1. When the donor concentration n_d is below a critical value n_c, the electrons are loosely bound to the donors, and they form a single donor level in the band gap(as shown in Fig. 2.2 (a))

2. When n_d is above n_c, the orbit of bounded electron starts to overlap with each other and hence they are delocalized, giving rise to a metallic behavior. The approximate expression for n_c is derived by Mott as the following:

$$n_c \cong (0.25/a_H^*)^3 \tag{2.1}$$

where $a_H{}^*$ is the Bohr radius of the hydrogen-like donor state. From the band structure point of view, the single impurity level spreads into an impurity band (Fig. 2.2 (b)).

3. when n_d is above a second characteristic concentration n_{c2}, the impurity band overlaps with the conduction band (CB) of the host crystal, and the Fermi

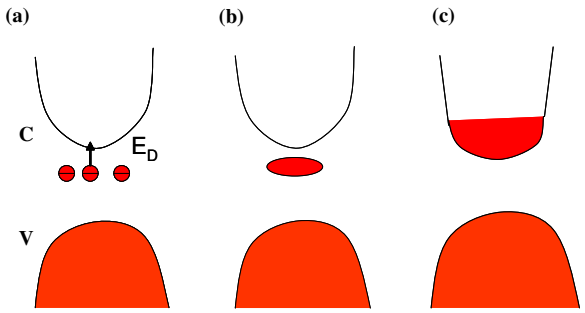

Figure 2.2: (a) A schematic band structure for an extrinsic doped semiconductor when (a) $n_d < n_c$; (b)$n_c < n_d < n_{c2}$; (c) $n_d > n_{c2}$.

level of the electron system moves up to CB as well (Fig. 2.2 (c)). This feature is not inherent in the metallic transition itself. It arises from the practical matter that one must embed the impurity system in a matrix in order to hold it together[34].

This Mott-transition picture is a useful guidance for the development of transparent conducting oxides. According to this picture, to achieve good conductivity in a transparent wide-band gap semiconductor, one should have: 1) shallow donors or acceptors; 2) considerable high concentration of these shallow impurities.

2.1.3 Optical Transitions

When light shines on a material, the electrons in the valence band of the material absorb the light energy and jump to higher energy levels, leaving holes in the original states. Generally, this optical transition, depending on the band structure of a material itself, includes two types: 1) direct band transition; 2) indirect band transition.

For a direct band semiconductor, the direct band transition dominates. The

top of the valence band and the bottom of conduction band have the same k value. Therefore, when an electron at the top of the valence band is excited to the bottom of the conduction band due to the absorption of light energy, its momentum ($\hbar k$) does not change. In this case, the absorption constant α has the following expression[35]:

$$(\alpha h\nu)^2 = A(h\nu - E_{og}) \tag{2.2}$$

where, hν is the photon energy, E_{og} is the optical band gap of a semiconductor (or optical absorption edge), and A is a constant.

In contrast, for an indirect band semiconductor, the top of valence band and the bottom of conduction band have different k values. Since the momentum of a photon is zero, the phonon interaction should be involved in order to satisfy the change of electron momentum during the transition from the top of valence band to the bottom of conduction band. In this case, the absorption constant is given by[35]:

$$(\alpha)^{1/2} = B(h\nu - E_{og}) \tag{2.3}$$

where, B is a constant.

Therefore, to obtain the optical band gap of a material E_{og}, one could plot $(\alpha h\nu)^2$ vs hν (for direct optical transition) or $(\alpha)^{1/2}$ vs hν (for indirect optical transition) and the intercept energy of the extrapolation of the data on the horizontal axis is the optical band gap.

An interesting optical effect called the Burstein-Moss effect[36] is often ob-

served in degenerate semiconductors. As discussed in section 2. 1.2, when the concentration of the shallow donors (n-type for example) is high enough, the Fermi level of the system passes through the conduction band and there are considerable conduction carriers at the bottom of the CB. Therefore, the electrons in the VB can only be excited to above the Fermi level instead of to the bottom of CB, which is occupied by conduction electrons. As a result, the optical band gap of the doped degenerate semiconductor is larger than that of the corresponding undoped semiconductor. This blue shift due to doping in a semiconductor is called the Burstein-Moss shift[36]. One can approximately calculate the effective mass of the charge carrier from the blue shift and conduction electron density. The blue shift can be written as[3]

$$\Delta E = \frac{\hbar^2 k_F^2}{2m^*} \tag{2.4}$$

where k_F is the Fermi wave vector. The total number of states (the concentration of conduction electrons in this case) is[3]

$$n = \frac{k_F^3}{3\pi^2} \tag{2.5}$$

Substituting eq. 2.4 into eq. 2.5, we have

$$n = \frac{1}{3\pi^2}(\frac{2m^*\Delta E}{\hbar^2})^{3/2} \tag{2.6}$$

or

$$m^* = \frac{\hbar^2}{2\Delta E}(3\pi^2 n)^{2/3} \tag{2.7}$$

2.1.4 Motivation

Most recently, niobium doped TiO_2 (NTO) was discovered as a new type of TCO with a room temperature resistivity of $10^{-4}\ \Omega cm$ and visible light transmittance as high as 90%[37]. And due to its promising properties, this material was proposed to be a replacement of ITO in the future. However, those works were focused on the films grown on $SrTiO_3$ (STO) substrates and the intrinsic properties of the films are under debate[37, 38, 39]. One reason for this is that niobium has great chance to diffuse into $SrTiO_3$ substrate and may form a thin layer of the well-known conductor Nb:$SrTiO_3$[40], which could contribute to the excellent conductivity observed in NTO/STO sample. In this work, we systematically studied the structural, electronic transport, and optical properties of Nb: TiO_2 thin films grown on different substrates. Depending on the substrates, different phases of NTO were formed. Our experimental results suggest the intrinsic transparent conducting nature of niobium doped anatase TiO_2, in contrast to the highly insulating nature of the rutile phase.

2.2 Sample Preparation

Thin films studied in this work were prepared by a pulse laser deposition (PLD) technique (See Appendix 1). The material targets ($Ti_{1-x}Nb_xO_2$ with different niobium concentration, x=0.00, 0.01, 0.03, 0.05, 0.07) for ablation were prepared by solid state reaction method. The mixed powder of Nb_2O_5 and TiO_2 with stoichiometric ratio was ground for several hours, and then pressed into 2 inch diameter

pellets under a pressure of 200000 Kpa for 15 min. Finally, these pellets were fired at 1250 ^{0}C in air for 24 hours.

The targets were laser ablated by a pulsed excimer laser deposition (KrF, λ=248 nm) with a repetition rate of 2 Hz. The energy density of the laser spots inside of the chamber is 2 J/cm^2. The substrates used in this work are: single crystal (001) $LaAlO_3$ (LAO), $SrTiO_3$ (STO), r-plane ($\bar{1}011$), c-plane (0001) sapphire (Al_2O_3) and quartz (SiO_2). The substrate temperature during deposition is ∼550 ^{0}C. The chamber was pumped for 24 hours in order to achieve a base pressure of $\sim 10^{-7}$ Torr. Then oxygen was introduced into the chamber to obtain a stable oxygen partial pressure of $\sim 10^{-5}$ Torr during deposition.

2.3 Structural Characterization

2.3.1 X-ray Diffraction

The 5% Nb: TiO_2 (NTO) thin films grown on various substrates were first characterized by X-ray diffraction (XRD) technique (See Appendix 2). Fig. 2.3 shows the $\theta - 2\theta$ patterns for all the films. For those films grown on (001) LAO and STO substrates, the XRD patterns only show anatase (004) and (008) peaks besides the substrate peaks. This suggests that these films are epitaxial with single anatase TiO_2 phase. However, the films grown on r-sapphire and c-sapphire substrates are epitaxial and of rutile phase with the (101) and (L00) orientations, respectively. The NTO film on quartz (SiO_2) forms polycrystalline rutile phase. The rocking curves of the anatase NTO (004) peak show that the full width at half maximum (FWHM)

of this peak are 0.420^0 and 0.930^0 for NTO/LAO and NTO/STO, respectively. This result indicates that NTO/LAO has a much better structural quality, which may be due to the lower lattice mismatch between TiO_2 and LAO ($\sim$ -0.26%) than that between TiO_2 and STO ($\sim$ -3.1%)[46].

2.3.2 Rutherford-back Scattering Channeling

To further bring out the information of crystalline quality and niobium distribution of NTO thin films, the Rutherford-back scattering channeling technique (See Appendix 3) was employed for detailed structural characterization. Fig 2.4 (a) and (b) show the Rutherford backscattering spectra (random and channeled) for 5% Nb: TiO_2 films grown on (001) LAO and STO respectively. The elemental positions are indicated on the spectra. The minimum channeling yield of Ti and Nb in NTO/LAO are both $\sim$ 10%, indicating that about 90% Nb substitutes into Ti site, while those for NTO/STO are only about 50%, suggesting that NTO/LAO has a much better crystalline quality than NTO/STO, consistent with the XRD results. Fig 2.4 (c) shows the spectrum for rutile NTO film grown on c- sapphire substrate. The minimum channeling yield of Ti and Nb in this film are both $\sim$ 10%, indicating the excellent crystalline quality as well as high solubility of niobium in rutile TiO_2

2.3.3 Atomic Force microscopy

Atomic force microscopy (AFM) (See Appendix 4) is a useful technique to study the surface morphology of thin films on the nanometer scale. Fig. 2.5 (a)

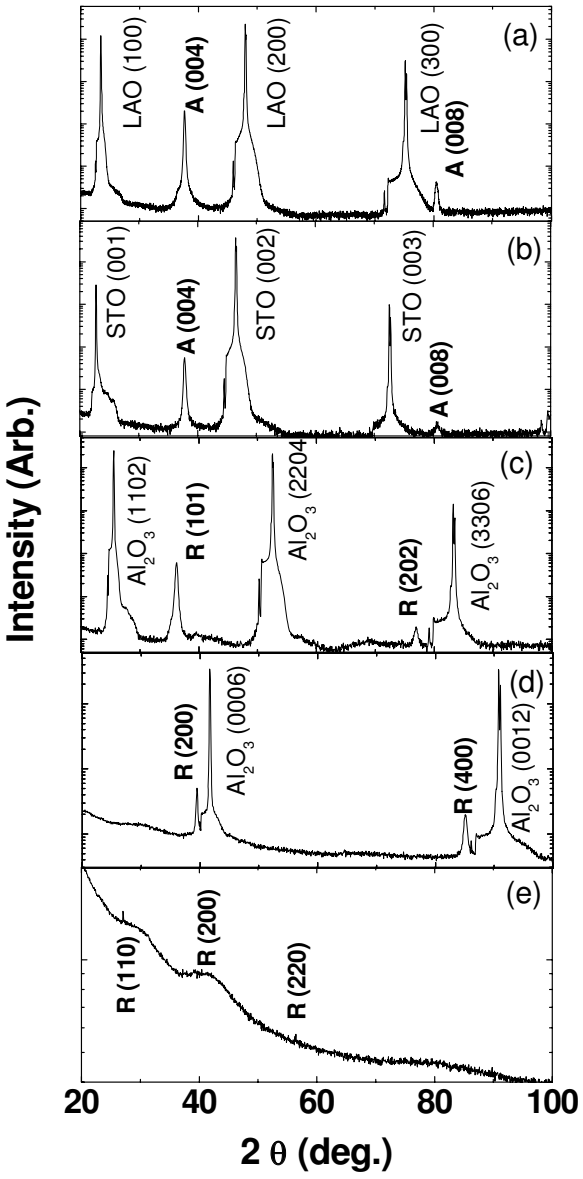

Figure 2.3: X-ray diffraction patterns for (a) NTO/LAO, (b) NTO/STO, (c) NTO/r-Al_2O_3, (d) NTO/c-Al_2O_3, and (e) NTO/quartz thin films. "A" denotes anatase phase, and "R" denotes rutile phase.

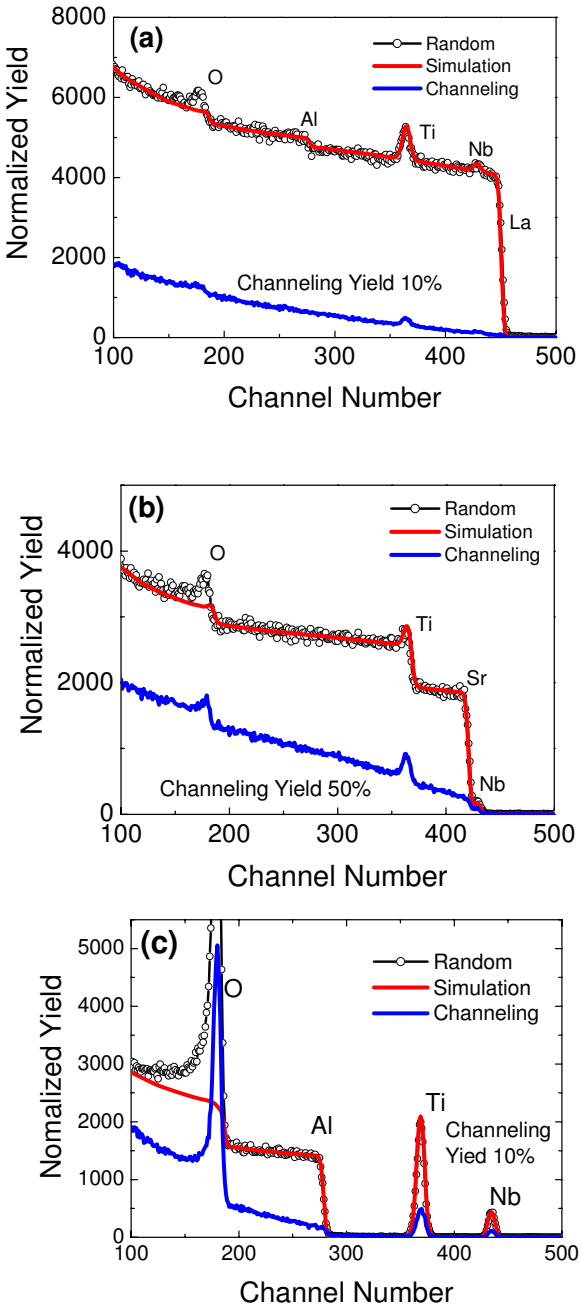

Figure 2.4: The 3.05-Mev He+ Rutherford backscattering (RBS) random, simulation and channeling spectra of the 5% Nb: TiO_2 films grown on (a) $LaAlO_3$, (b) $SrTiO_3$, and (c) c-Al_2O_3 substrates

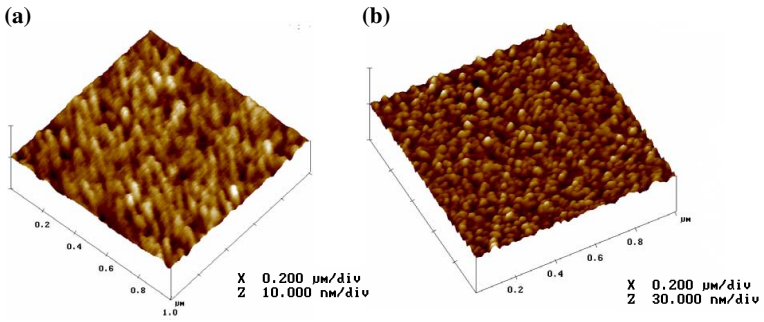

Figure 2.5: AFM images of (a) NTO/LAO and (b) NTO/STO films.

and (b) show the AFM image of NTO/LAO and NTO/STO films respectively. The stripe-like structure observed in NTO/LAO image is due to the step features on LAO substrate during production. Apparently, viewed from the images, the surface of NTO/LAO film is much smoother than that of the NTO/STO film. Indeed the mean roughness is ~ 0.344 nm for NTO/LAO, while it is ~ 1.050 nm for NTO/STO. This result should also be attributed to the lattice mismatch between film and substrate.

2.3.4 Transmission Electron Microscopy

We investigated the interface nanostructure of NTO/STO by using transmission electron microscopy (TEM)(See Appendix 5). Fig. 2.6 (a) shows the large-scale TEM cross-section image. The interface between the film and substrate is denoted by a red arrow. The high resolution TEM image (Fig. 2. 6. (b)) at an interface area shows a slightly distorted NTO nanostructure along the interface, which may be caused by the misfit dislocations, stress at early stage deposition and 2$\sim$3 atomic-level steps on the original STO substrate surface. Fig. 2. 6 (c) shows the

electron diffraction patterns (EDP) taken at both the substrate (the lower panel) and interface (the upper panel). We separated out the EDP of film from that of the interface as shown in Fig. 2. 6. (d). The EDP of film indicates that NTO is in an epitaxial anatase structure. Unfortunately, due to the lack of proper technique for the chemical distribution analysis, we were unable to conclude whether there is any interdiffusion of niobium in STO and thereby contributing to the excellent conductivity of NTO/STO sample. However, no extrinsic conducting layer forms when Nb diffuses into LAO and moreover our cobalt doped NTO/LAO has been shown not to exhibit interdiffusion even when grown at very high temperature (discussed in chapter 6). Therefore, the intrinsic property of Nb doped anatase TiO_2 discussed below will refer to the NTO/LAO samples.

2.4 Conductivity

The samples were patterned into a Hall geometry by ion milling with a mechanical Hall bar (i.e. Hall mask). The electronic transport measurements were performed by using a Quantum Design Physical Property Measurement System (PPMS)(See Appendix 6). The measurement temperature is from 300 K down to 5 K.

Fig. 2.7 (a) shows the temperature dependence of resistivity for NTO/LAO and NTO/STO. Both samples show metallic behavior and the room temperature (RT) resistivity is 4.95×10^{-4} Ωcm for the NTO/LAO and 5.59×10^{-4} Ωcm for the NTO/STO (The calculation based on the assumption that no interface Nb: $SrTiO_3$

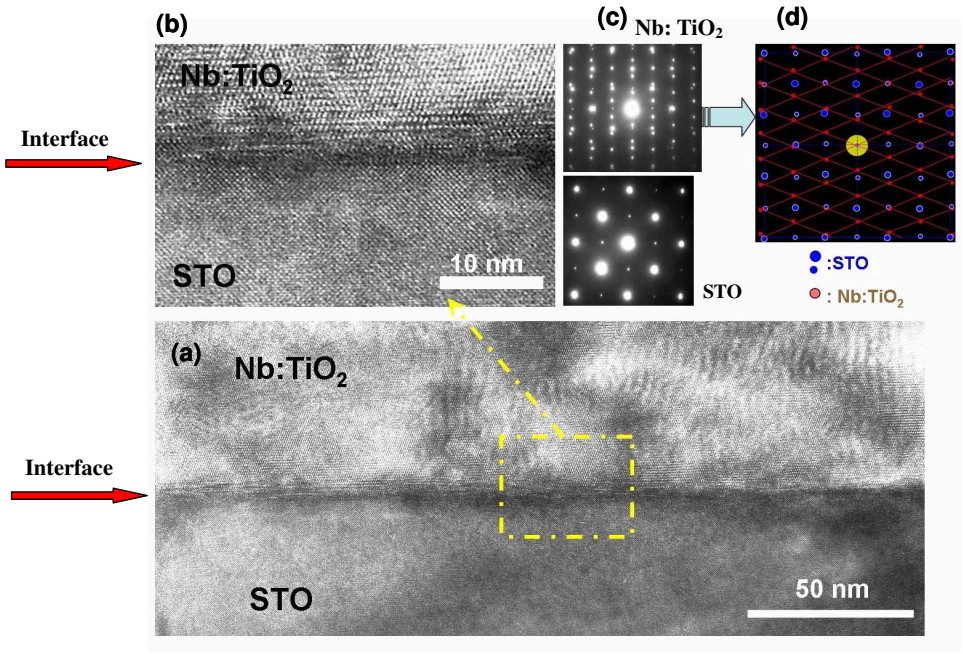

Figure 2.6: (a)Large-scale TEM image of NTO/STO sample; (b) high resolution TEM image at an interface area of NTO/STO; (c) lower panel: electron diffraction pattern taken at the substrate regime; upper panel: electron diffraction pattern taken at the interface; (d) the simulation of interface electron diffraction pattern.

contribution is present in NTO/STO). We performed Hall measurements on these samples. The Hall constants were found to be negative, which indicates that the carriers are electrons. The carrier density calculated from the Hall constant (see Appendix 6) in the film on LAO (shown in Fig. 2.7 (b)) is $\sim 1.25\times10^{21}$ cm^{-3} at room temperature. Since the Nb impurity concentration is $\sim 1.45\times10^{21}$cm^{-3}, the carrier density vs Nb concentration is $\sim$ 90%. This number is close to the Nb substitution rate ($\sim$90%) in NTO/LAO obtained from channeling, which indicates that the carriers are almost all from niobium donor (the detailed discussion will be presented in Chapter 3). Fig. 2.7 (b)shows the Hall mobilities μ as a function of temperature (see Appendix 6 for the details of how the mobility is determined). The mobility for NTO/LAO increases from 10 cm^2 V^{-1}S^{-1} to 33 cm^2 V^{-1}S^{-1} as temperature decreases from RT to 10 K. On the assumption that no contribution emanates from the interface Nb: $SrTiO_3$ layer, the Hall mobility for NTO/STO film increases from 9 cm^2 V^{-1}S^{-1} to 25 cm^2 V^{-1}S^{-1} during cooling from RT to 5 K. Since the carrier concentration is almost temperature independent, the increase of mobility with cooling gives rise to the metallic property of the NTO system.

Fig. 2.8 (a) shows the resistivity data of three rutile NTO thin films grown on r-sapphire, c-sapphire and quartz substrates. All the R-T curves show negative slope indicating semiconducting (or insulating) properties. The room temperature resistivities are found to be 0.066 Ω cm for NTO/ r-Al_2O_3, 0.08 Ω cm for NTO/c-Al_2O_3, and 0.13 Ω cm for NTO/SiO_2. Fig. 2.8 (b) shows the carrier density n as a function of 1/T for these three samples (Hall measurements could only be performed above 230 K due to the high resistance at low temperatures, carrier density was

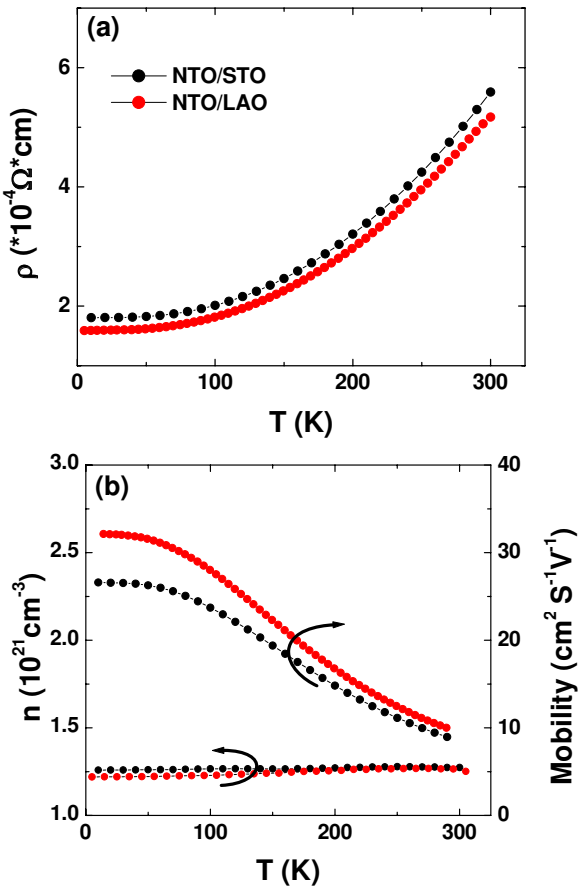

Figure 2.7: Temperature dependence of (a) resistivity and (b) carrier density & Hall mobility for NTO/STO (black curves) and NTO/LAO (red curves)

obtained by simply assuming Hall mobility is amost equal to drift mobility). In contrast to the case of anatase, carrier density decreases quickly as temperature decreases and ln(n) is almost linear in 1/T. By fitting the data to $\ln(n) \sim \frac{\varepsilon}{k_B T}$, we found the electron activation energy ε to be $\sim$ 0.075 eV for NTO/c-sapphire and 0.088 eV for NTO/r-sapphire. This indicates that rutile NTO is a thermally activated semiconductor, while anatase NTO is a degenerate semiconductor. In Table 2.2, we compared the room temperature resistivity, carrier density, and Hall mobility of all the samples. The room temperature resistivities of rutile NTO films are $2 \sim 3$ orders higher than that of the epitaxial anatase film grown on (001) LAO. However, it is found that the RT carrier densities ($\sim 2.4 \times 10^{20}$ cm^{-3}) of these three rutile films are only 5 times lower than that of the single crystalline anatase phase. This result suggests that the origin of higher resistivity of rutile phase is due to its significantly lower ($\sim$30 times) carrier mobility. In a simple Drude approximation, the mobility is given by: $\mu = \mathrm{e}\ \tau\ /\mathrm{m}^*$, where τ is the relaxation time, and m^* is the effective mass of the carriers. It is noticed that the effective mass of rutile ($8\sim20$ m_0)[15] is much larger than that of anatase ($\sim\mathrm{m}_0$)[19], therefore it is reasonable that rutile has a much lower mobility.

The different transport behaviors between anatase and rutile phases can be attributed to the different Bohr radius of the hydrogen-like donor state in this matrix. According to the Mott transition picture in semiconductors (as discussed in section 2. 1. 2), the relation between the critical donor concentration (n_{dc}) for the Mott transition and the Bohr radius ($\mathrm{a}_H{}^*$) of the hydrogen-like donor state is described by eq. 2.1 [33]. From their systematic electrical studies, Tang et al. [19] has found

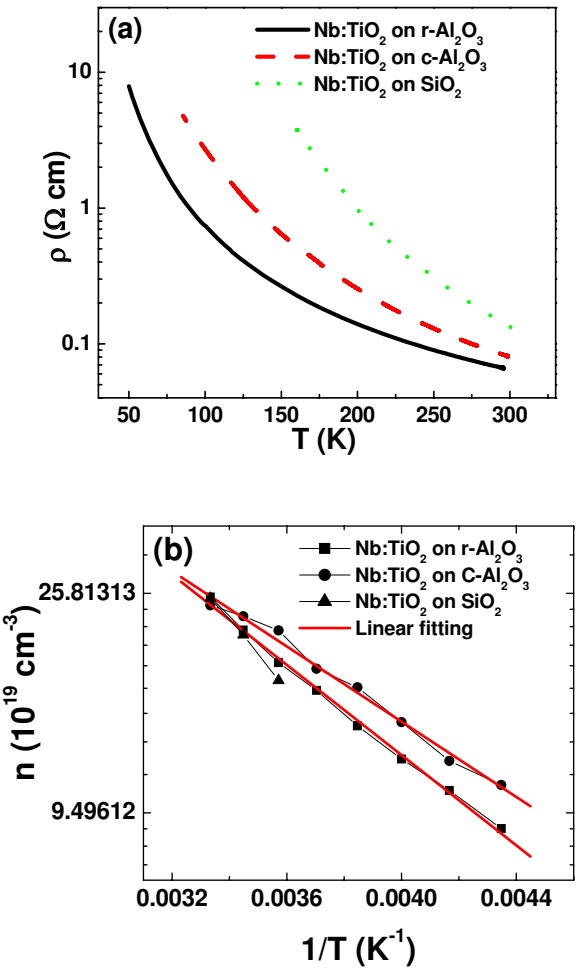

Figure 2.8: (a) Temperature dependence of resistivity for NTO/ r-Al_2O_3 (black solid line), NTO/ c-Al_2O_3 (red dashed line), and NTO/Quartz (green dotted line); (b) Carrier density as a function of 1/T for NTO/ r-Al_2O_3 (square dots), NTO/ c-Al_2O_3 (round dots), and NTO/Quartz (up triangle dots). red curves are fitting data.

that anatase TiO_2 has a much larger effective Bohr radius ($\sim 15\mathring{A}$) than rutile does ($\sim 2.6\mathring{A}$). Therefore the critical donor density of anatase is much lower (5×10^{18} cm^{-3}) than that of rutile ($> 10^{21}$ cm^{-3}). With the effective donor concentration (niobium substitutional concentration) of $\sim 1.25\times 10^{21}$ cm^{-3}, the anatase phase falls into a degenerate semiconductor region and hence shows metallic behavior.

Table 2. 2 The comparison of room temperature resistivities, carrier densities and Hall mobilities of 5% Nb: TiO_2 thin films grown on various substrates.

Samples	RT resistivity (Ω cm)	RT carrier density (cm^{-3})	RT Hall mobility (cm^2 S^{-1} V^{-1})
Anatase NTO on LAO	4.95×10^{-4}	1.25×10^{21}	10
Anatase NTO on STO	5.59×10^{-4}	1.26×10^{21}	8.9
Rutile NTO on r-Al_2O_3	0.066	2.55×10^{20}	0.379
Rutile NTO on c-Al_2O_3	0.08	2.42×10^{20}	0.323
Rutile NTO on Quartz	0.13	2.40×10^{20}	0.199

2.5 Optical properties

In Fig 2.9 (a), we show the transmittance spectra of the anatase TiO_2 and NTO thin films together with LAO, STO substrates. We evaluated the internal transmittance of all films by subtracting the absorption and reflection of the substrate. These internal transmittances found in both NTO/LAO and NTO/STO are above 80% in the visible range, suggesting these epitaxial metallic anatase NTO films are considerately transparent to visible light. Interestingly, the absorption edge of the film grown on LAO shows a blue shift with niobium doping. This shift

may be attributed to the Burstein-Moss effect[36], usually observed in degenerate semiconductors, as discussed in section 2.1.3. Since the optical transition in antase TiO_2 is indirect[16], we plot $\alpha^{1/2}$ as a function of hν in the inset of Fig. 2.9 (a). The extrapolated optical absorption edge of TiO_2 and Nb: TiO_2 are found to be 3.22 eV and 3.37 eV respectively. If a single parabolic conduction band is assumed, one can roughly evaluate the effective mass of the conduction electrons. Our calculation shows this effective mass m^* is $\sim$2.5 m_0, where m_0 is the electron mass. For the sample grown on STO, the absorption edge is dominated by the band edge of the STO substrate itself, forbidding the observation of the expected similar shift in this case.

Fig. 2.9 (b) shows the transmittance spectra of the rutile samples with different substrates. The evaluated internal transmittance of the films is $\sim$70%. Assuming the indirect optical transition of rutile TiO_2[15, 16], we plot $\alpha^{1/2}$ as a function of hν in the inset of 2.5 (b). The extrapolated optical absorption edges of TiO2 grown on c-sapphire, r-sapphire and quartz are $\sim$3.09 eV, while those of the NTO films are $\sim$ 3.18 eV. We would like to point out that this shift of rutile NTO films with a magnitude of 0.09 eV is surprising, given the low carrier density (2.5×10^{20} cm^{-3}) of these films. If this blue shift is also from the Burstein-Moss effect, calculation based on the simple conduction band assumption will give rise to a very small effective mass m^* $\sim$1.5 m_0, which is unexpected since the effective mass of rutile TiO_2 in the literatures is usually about 8$\sim$20 m_0[19], indicated also by the significantly low Hall mobility in our rutile samples. This large shift may very well arise from the widening of band gap with niobium doping, as indicated by X-ray photoemission

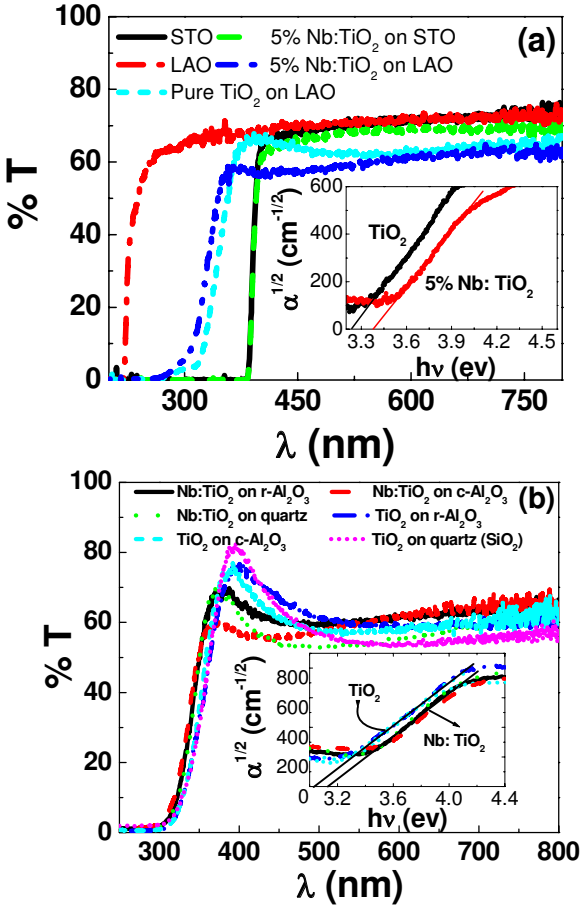

Figure 2.9: (a) transmittance spectra of anatase TiO_2, NTO samples and LAO, STO substrates. Inset shows $\alpha^{1/2}$ vs hv for TiO_2/LAO and NTO/LAO thin films. (b) Transmittance spectra of rutile TiO_2 and NTO samples. Inset shows $\alpha^{1/2}$ vs hv.

studies[42]. However, the precise origin of this unusual blue shift requires further investigations.

2.6 Summary

In conclusion, we have grown 5%Nb: TiO_2 films on LAO (001), STO (001), r-Al_2O_3, c-Al_2O_3 and quartz. RBS channeling data directly reveal the substitution of

Nb into Ti lattice (∼90%) for the epitaxial anatase NTO/LAO film, which is found to be an excellent intrinsic conducting oxide ($\rho_{RT} \sim 4.95\times10^{-4}$ Ω cm). In contrast, the rutile phase of NTO shows much higher resistivity (2 ∼ 3 orders higher room temperature resistivity than that of the anatase phase) and a considerably lower mobility. A blue shift in the optical absorption edge is observed in both phases, and the magnitude of this shift in rutile is surprisingly large.

Chapter 3

The Growth Parameter - Property Phase Diagram of Anatase Nb: TiO_2

In Chapter 2, we demonstrated that epitaxial anatase Nb: TiO_2 thin films grown at 550 ^{0}C and oxygen partial pressure of 10^{-5} Torr were intrinsic transparent conducting oxides, with a room temperature resistivity of $5\times10^{-4}\Omega$ cm and visible light transmittence of above 80%. Given the growing significance of NTO as an electronic material, it is of interest to understand and optimize the corresponding film growth by exploring the growth parameter-property phase diagram. In the commonly used pulsed laser deposition technique, the deposition temperature and oxygen partial pressure are the crucial parameters in the context of optimization, because they can modify the crystalline structure, native defects and charge states. Therefore, in this work, we performed a systematic study of the growth condition dependent structural and electrical properties of Nb doped TiO_2 thin films.

3.1 Practical Doping Rules

Before addressing the experimental details, I introduce some theoretical conclusions on the growth parameter dependence of doping ability in semiconductors. Some practical doping rules have been summarized by A. Zunger [43]based on the basic formation energy equation. This equation, describing the formation energy of

dopant D of charge state q in host crystal, is written as[43]:

$$\Delta E^{D,q}(\mu, E_F) = qE_F + n_D(\mu_D - \mu_{host}) + E^{total}(host + D) - E^{total}(host) \quad (3.1)$$

where q E_F is the electro-chemical potential of charge q, n_D is the concentration of dopants, μ_D and μ_{host} are the chemical potentials of the dopants and host respectively, E^{total}(host+D) is the total energy of host crystal with dopant D, E^{total}(host) is the total energy of the host crystal without dopant. The $\Delta E^{D,q}(\mu, E_F)$ represents the ability of forming a impurity/defect in the host material (The lower the $\Delta E^{D,q}(\mu, E_F)$ is, the easier the impurity/defect is formed).

As we know, the Fermi energy of a semiconductor is shifted upwards due to n-type doping, while downwards for p-type doping. From eq. 3.1, the formation energy of n-type defects (producing electron, $q > 0$) increases linearly with E_F, while the same for p-type defects (capturing electron, $q < 0$) decreases linearly with E_F. Accordingly, when we are trying to dope a material n-type by introducing extrinsic donors, the E_F of the material moves towards the conduction band; therefore the formation energy of native acceptors, such as cation vacancies V_C and anion interstitial A_i, would decrease to a point such that "electron-killers" will form spontaneously. Similarly, when we are trying to dope a material p-type by introducing extrinsic acceptors, E_F of the material moves towards the valence band, and thereby the formation energy of native donors, such as anion vacancies V_A and cation interstitial C_i, would decrease to a point that such "electron-killers" will form spontaneously. This particular Fermi energy at which compensative native defects start to form is called pinning energy. If the conduction band minimum (CBM)

of the host is above the pinning energy for n-type extrinsic doping (E_F^n), then the Fermi energy encounters E_F^n before it enter into the conduction band, which means p-type native defects form and hence kill the electrons produced by n-type doping. This material is thus very difficult to be doped n-type. Similarly, If the valence band maximum (VBM) of the host is above the pinning energy for p-type extrinsic doping (E_F^p), then the Fermi energy encounters E_F^p before it enters into the valence band, which means n-type native defects form and hence kill the holes produced by p-type doping. This material is thus very difficult to be doped p-type. Therefore, the following doping principles can be derived:

Rule 1: n-type doping is favorable in materials whose CBM are far from the vacuum level, whereas p-type doping is favorable in materials whose VBM is close to the vacuum level[43].

Rule 2: As p-type native defects such as cation vacancies V_C impede n-type doping, one can overcome it by designing growth conditions, such as host cation-rich growth conditions, which destabilize cation vacancies. And as n-type native defects such as anion vacancies V_A impede p-type doping, one can overcome it by designing growth conditions, such as host anion-rich growth conditions, which destabilize these hole-killer defects[43].

The second term in eq. 3.1 indicates that the defects which donate host anions (or cations) to the chemical reservoir e.g., anion vacancy V_A (or cation vacancy V_C), are easier to form at anion-poor (or cation-poor) growth condition at which this reservoir has low anion (cation) chemical potential. Therefore, the following rule can be derived:

Rule 3: Anion-substituting dopants is more soluble under host anion poor (host cation rich) growth conditions, whereas cation-substituting dopants is more soluble under host-cation poor (host anion rich) growth conditions[43].

Now let's look at the last term in eq. 3.1 ($\Delta E^b = E^{total}(host+D) - E^{total}(host)$). Apparently, to obtain a low formation energy, the total energy of host with dopant respective to the total energy of host without dopant must be as small as possible, which leads to the following rule:

Rule 4: The cation (or anion) dopant is easier to substitute into the host-cation site if the chemical bonding between dopant and host-anion (or host-cation) is stronger than that between the host-cation and anion[43].

3.2 Basic Growth Parameters

The $Ti_{0.95}Nb_{0.05}O_2$ (NTO) thin films were grown on single crystal (001) $LaAlO_3$ (LAO) via pulsed laser deposition (PLD). The laser energy density was kept at 2J/cm^2 during growth. The substrate temperature was varied from 350 ^{0}C to 850 ^{0}C when oxygen partial pressure was kept at 10^{-5} Torr. The oxygen partial pressure was varied from 5×10^{-6} Torr to 1×10^{-3} Torr when the substrate temperature was kept at 850 ^{0}C. X-ray diffraction and Rutherford-back scattering channeling measurements were performed for structural characterization. Four probe resistivity and Hall measurements were carried out for electrical analysis by using Quantum Design Physical Property Measurement System (PPMS).

3.3 Substrate Temperature Effects

3.3.1 Niobium Substitutional Fraction

X-ray diffraction results (not shown here) indicate that the film grown at 350 ^{0}C and 10^{-5} Torr is polycrystalline and the one grown at 400 ^{0}C shows a mixture of anatase and rutile phase. All the other films show epitaxial anatase phase with (00L) orientation except for the one grown at 850 ^{0}C and 5×10^{-6} Torr which shows an impurity phase of Nb_2O_5.

Fig 3.1 (a) shows the Rutherford back-scattering (RBS) spectra of the NTO/LAO films grown at various temperatures, with the oxygen partial pressure of 10^{-5} Torr. From the simulation of the random spectra, we found that the thickness of these films is $\sim$ 60 nm, thinner that our previous samples ($\sim$ 80nm in Chapter 2). It is clearly noted (Fig. 3.1 (b)) that the minimum channeling yields of both Ti and Nb, obtained from RBS spectra, decrease as the substrate temperature (T_S) during film deposition is increased, which indicates the improvement of structural quality as well as substitutional fraction. We can obtain the absolute substitutional fraction of niobium using the formula of S_{Nb} = 1-χ_{minNb}, where χ_{minNb} is the minimum channeling yield of niobium. Fig. 3.1 (c) shows S_{Nb} vs $1/T_s$ in NTO/LAO films (The same for the rutile NTO films grown on c-sapphire are also plotted for comparison). We can obtain the activation energy by fitting the data using the Arrhenius-like equation:

$$S_{Nb} \sim e^{\frac{-E_A}{RT}} \tag{3.2}$$

where R = 8.62 $\times$ 10^{-5} eV$\cdot$ $K^{-1}\cdot$ $atom^{-1}$ is the universal gas constant. It is found that the activation energy for Nb incorporation into Ti site in anatase is $\sim$ 0.068 eV/atom, while in rutile is $\sim$ 0.074 eV/atom. The activation energies are low, which indicates that it is easy to substitute Nb into Ti for both phases even at low growth temperatures. This is in contrast to other transition metal doped TiO_2, such as diluted magnetic semiconductors[44, 45, 46], in which the dopants are found to be very difficult to incorporate substitutionally. The high solubility of Nb may be attributed to the close ionic radius of Nb^{5+} (0.78 $\mathring{A}$) and Ti^{4+} (0.75 $\mathring{A}$) in the octahedral coordination.

3.3.2 Carrier Concentration and Hall Mobility

It is found that all the films grown at 10^{-5} Torr are metallic. Fig. 3.2 shows the temperature dependence of resistivity for NTO/LAO sample grown at 850 ^{0}C as an example. We performed Hall measurements in order to get the carrier concentration and Hall mobility (see Appendix 6 for detailed information). The inset of Fig. 3.2 shows the temperature dependence of carrier concentration (n_c) and mobility (μ) of this sample . The room temperature carrier concentration is $\sim$ 1.21$\times 10^{21}$ cm^{-3} and it decreases slightly as the temperature decreases (from 1.21$\times 10^{21}$ cm^{-3} at RT to 1.14$\times 10^{21}$ cm^{-3} at 2 K, the difference is 7×10^{18} cm^{-3}). Such small decrease of n_c indicates that the niobium impurity band has overlapped with conduction band and a degenerate semiconductor is formed. However there could be a small part of conduction carriers from thermal activation of other native defects levels[47] (i.

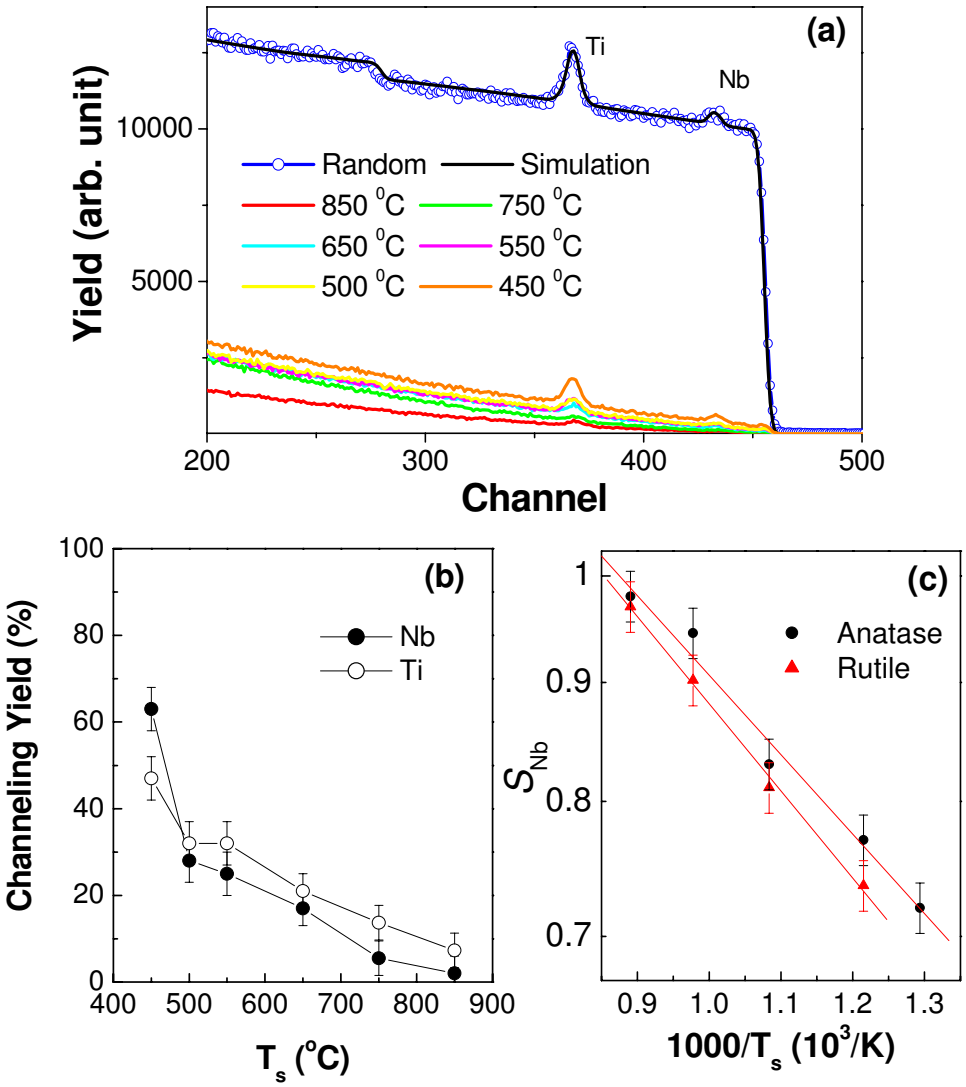

Figure 3.1: (a) The 3.05-Mev He+ Rutherford backscattering (RBS) random, simulation and channeling spectra of the $Ti_{0.95}Nb_{0.05}O_2$ films grown on LAO substrate at various temperatures (b) The χ_{min} of titanium and niobium as a function of T_S. (c) Nb substitutional fraction S_{Nb} vs $1/T_S$ for both anatase NTO/LAO films and rutile NTO/c-sapphire films (S_{Nb} is in $\log_{10}$ scale; black and red dots are experiment data, and solid lines are fitting data).

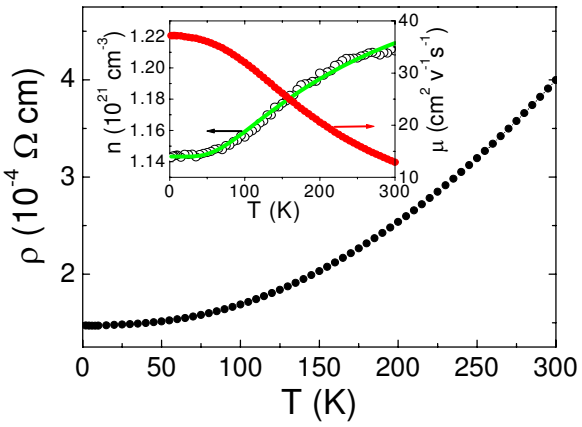

Figure 3.2: Resitivity as a function of temperature for the NTO/LAO film grown at 850 ^{0}C, 10^{-5}Torr. Inset shows carrier concentration n_c (black circles are experiment data, green curve is the theoretical data) and Hall mobility μ as a function of temperature.

e. Ti_i and V_O in the oxygen poor regime), which leads to the slight decrease of n_c with cooling. We fitted the carrier concentration data in the inset of Fig. 3.2 by the simplified formula of

$$n = n_0 + \frac{n_1}{2} e^{\frac{-E_d}{K_B T}} \tag{3.3}$$

where n_0 corresponds to the carrier from niobium, n_1 corresponds to the native defects, k_B is the Boltzmann constant and E_d is the activation energy of the native donors. We obtained the values as: n_0=1.14×10^{21} cm^{-3}, n_1=1.55×10^{20} cm^{-3} , and E_d= 0.02 eV.

In order to study the correlation between the electrical properties and crystalline quality as well as niobium substitutional factor. We show the substrate temperature dependence of niobium substitutional fraction (s_{Nb}) and carrier efficiency n/n_{Nb} (at 2 K and 300 K) in Fig. 3.3 (a), where n_{Nb}=1.45×10^{21} cm^{-3} is the niobium doping concentration. It is noted from the above discussion that the low

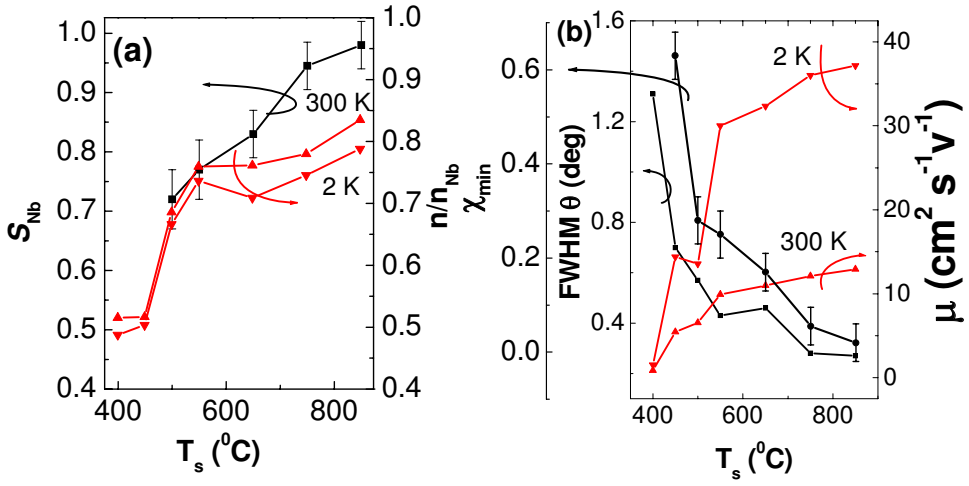

Figure 3.3: (a) The carrier concentration n_c (at 300 K and 2 K) and S_{Nb} of NTO/LAO films as a function of T_S. (b) Hall mobility μ (at 300 K and 2 K), full width at half maximum (FWHM) and minimum channeling yield of titanium in NTO/LAO films as a function of T_S.

temperature carrier concentration is more like only from niobium donors. Indeed with increasing the growth temperature, both the carrier density at 2 K and niobium substitutional fraction show a clear increase. Fig. 3.3 (b) shows the growth temperature dependence of mobility, thin film channeling, and full width at half maxium (FWHM) of the (004) peak. Apparently, the mobility shows a great enhancement with the increase of substrate temperature due to the improvement of crystallinal structural quality. And the low mobility of NTO film grown at 350 ^{0}C may indicate large grain boundary contribution.

3.4 Oxygen Effects

3.4.1 Valence States of Niobium and Titanium

The oxidation state of titanium in stoichiometrical TiO_2 is +4, therefore, niobium (normally in +4 or +5 state) provides one extra electron if it is in +5 state but no electron if it is in +4 state. On the other hand, if titanium is somehow in +3 state, then one hole can be induced. Therefore, to further confirm that the electrons in Nb: TiO_2 are introduced by niobium, it is essential to study the valence state of niobium and titanium by means of X-ray photoelectron spectroscopy (XPS). An introduction to XPS technique and experiment is given in Appendix 7 of this thesis. Figure 3. 4 (a) shows Nb 3d XPS spectra for $Ti_{0.95}Nb_{0.05}O_2$ films grown at 850 ^{0}C and under different oxygen partial pressures. The binding energies of Nb $3d^{3/2}$ and Nb $3d^{5/2}$ are 210.2 eV and 207.7 eV, respectively, and are oxygen pressure independent. According to the literatures[48], these binding energies correspond to +5 valence state rather than +4 state of niobium. Fig. 3. 4 (b) shows the Ti 2p spectra for the same samples and Ti 2 $p^{1/2}$ and 2 $p^{3/2}$ peaks are found to be at 465.1 eV and 459.5 eV, respectively. These binding energies correspond to the +4 state of titanium[49]. Therefore, niobium is indeed the main source of conduction electrons in this system.

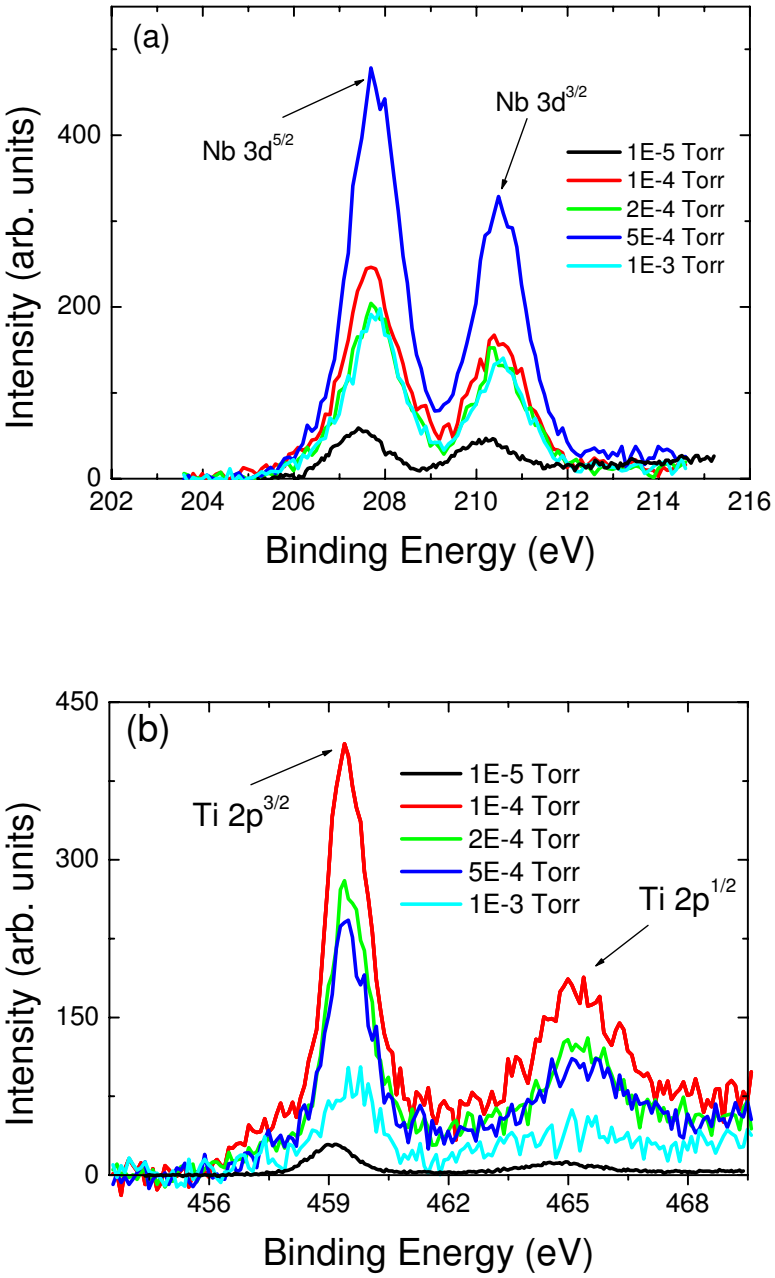

Figure 3.4: The X-ray photoelectron spectroscopy (XPS) spectrum in (a) Nb 3d regime & (b) Ti 2p regime.

3.4.2 Carrier Concentration, Hall Mobility and Niobium Substitutional Fraction

Fig. 3.5 (a) shows the oxygen pressure dependence of carrier concentration and niobium substitutional fraction of the films grown at 850 ^{0}C. With increase in the oxygen pressure (P_{O2} from 10^{-5} Torr to 5×10^{-3} Torr), the carrier concentration decreases by several orders though the niobium substitutional fraction only decreases from 98% to 84%. There have been some suggestions that the decrease of carrier concentration might be due to the decrease of oxygen vacancies while the film is being grown at high oxygen partial pressure. However, as discussed above, most of the carriers are from niobium donors instead of oxygen vacancies. Since the niobium substitutional fraction doesn't change considerably and the valence state of niobum is +5, the decrease of carrier concentration may indicate that large number of "electron killers", i. e. V_{Ti} and O_i, form due to their low formation energy[47] and hence compensate for the electrons provided by Nb.

Fig. 3.5 (b) shows the RT mobility and χ_{min} of titanium in NTO films as a function of oxygen partial pressure. As P_{O2} increases, the mobility decreases, which is believed to be due to the increase of disorder as evidenced by the increase of χ_{min}.

We have to point out that the good conductivity of NTO is mainly due to its large carrier concentration rather than high mobility. The large carrier concentration (almost equal to doping concentration) of NTO when grown at 10^{-5} Torr is because of the following: 1) in this host, under anion poor (= host cation rich) growth condition, the p-type native defects are not easy to form according to the doping

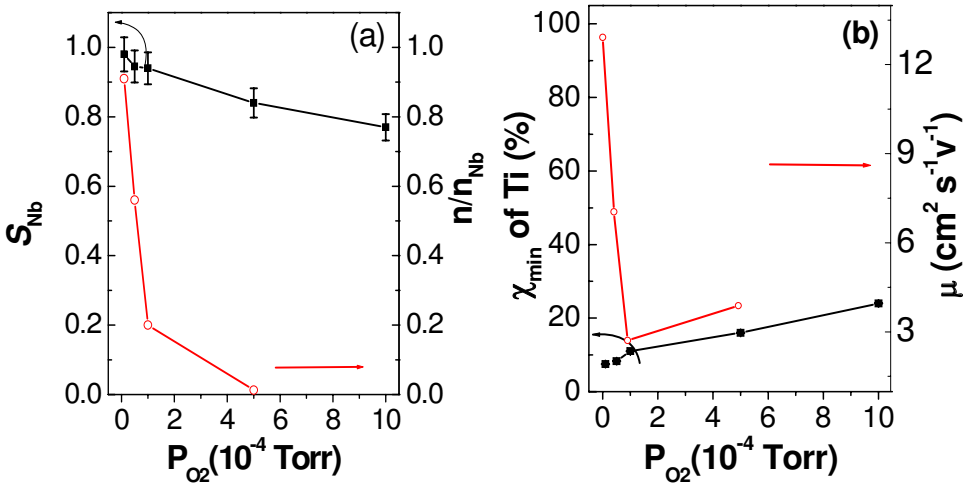

Figure 3.5: (a) The carrier concentration at 300 K and S_{Nb} of NTO/LAO films as a function of P_{O2}. (b) Hall mobility at 300 K and χ_{min} of titanium in NTO/LAO films as a function of P_{O2}. (Due to the high resistivity of the film grown at 5×10^{-4} Torr, a thicker film of $\sim$ 250 nm was used for electric measurement. The resistivity of the one grown at 10^{-3} Torr is too high to be measured.

rules. 2) Niobium, acting as shallow donor, is extremely soluble in TiO_2 even at this growth condition unfavorable for cation substitution.

3.5 Summary

In summary, the structural and electrical properties of niobium doped TiO_2 thin films grown at various conditions were studied via X-ray diffraction, Rutherford back scattering channeling and transport measurements. Niobium was found to easily incorporate substitutionally into titanium lattice site with low activation energy ($\sim$0.068 eV/atom for anatase and $\sim$0.074 eV/atom for rutile). By increasing T_S, the carrier concentration as well as the niobium substitution fraction increase, and the mobility also improves as the structural quality is enhanced. With increasing

P_{O2}, the carrier concentration decreases dramatically though the niobium substitution fraction doesn't change significantly. However, the oxidation states of niobium and titanium are in +5 and +4, respectively and are independent on P_{O2}. Therefore, the decrease of electron concentration may indicate that a large number (10^{20} cm^{-3}) of p-type native defects (such as V_{Ti}, O_i etc.) form and "kill" the electrons produced by Nb donor. The excellent conductivity of epitaxial NTO thin film grown at 10^{-5} Torr is because of the high solubility of niobium in TiO_2 even at the growth condition unfavourable for cation substitution.

Chapter 4

Introduction to Oxide based Diluted Magnetic Semiconductors (DMSs)

The following chapters of this thesis deal with another class of materials, called diluted magnetic semiconductors, fabricated with titanium oxides as host materials. In this chapter, I present a brief introduction to this type of material, which covers the basic physics of magnetism, motivation for studying these materials, previous experimental results as well as theoretical models.

4.1 Introduction to Ferromagnetism

4.1.1 Magnetic Moment & Exchange Interaction

An electron has both the charge degree of freedom and spin degree of freedom. The spins of the electrons are the basis of magnetism in a solid. Basically, the magnetic moment ($\vec{m}$) of an atom is determined by both the spin configuration and orbital configuration of the electrons in it[50, 51, 52]

$$\vec{m} = g\mu_B \vec{J} = g\mu_B \sqrt{J(J+1)}\vec{e}_J \tag{4.1}$$

Where, $g = 1 + \frac{J(J+1)+S(S+1)-L(L+1)}{2J(J+1)}$ is the Lande g factor, $\mu_B = \frac{e\hbar}{2m_0 c}$ is the Bohr magneton (m_0 is the electron mass), and S, L, J are the quantum numbers related with the spin, orbital, and total angular momentum of the electrons in the

atom ($\vec{J} = \vec{L} + \vec{S}$). In most of the solids, the orbital momentum is quenched (L=0) and hence the magnetic moment is determined by the spin momentum of the electrons (S). If the atomic spins ($\vec{S_i}$) in a solid do not interact with each other, this system is called paramagnetism. While if the spins interact with each other and tend to align in the same (or opposite) direction, this interaction is ferromagnetic (or antiferromagnetic). The interaction, called *exchange interaction*, between the spins originates from quantum-mechanical properties of spins. Simply, because electrons are Fermions, they must satisfy the Pauli exclusion principle, i. e. overall wave function of a system must be antisymmetric when any two electrons are exchanged. Taking a two-electron system for example, we assume they have individual orthogonal spatial wave functions $\psi_1(r_1)$ and $\psi_2(r_2)$. If the spatial wave function for the entire system is antisymmetric, i. e.,

$$\Psi_A(r_1, r_2) = \frac{\psi_1(r_1)\psi_2(r_2) - \psi_1(r_2)\psi_2(r_1)}{2} \tag{4.2}$$

then the spin wave function must be symmetric, i.e, spin for overall system is S=1 (two spins tend to align parallel to each other). While if the spatial wave function for the entire system is symmetric, i. e.,

$$\Psi_A(r_1, r_2) = \frac{\psi_1(r_1)\psi_2(r_2) + \psi_1(r_2)\psi_2(r_1)}{2} \tag{4.3}$$

then the spin wave function needs to be antisymmetric, i.e. spin for overall system is S=0 (two spins tend to align antiparallel to each other).

The energy difference between these two states is

$$J_{1,2} = 2 \int \int \psi_1^*(r_1)\psi_1^*(r_1)\frac{e^2}{r_{1,2}}\psi_1(r_2)\psi_2(r_1)dr_1dr_2 \tag{4.4}$$

where $\frac{e^2}{r_{1,2}}$ is the Coulomb interaction energy between two electrons, and $r_{1,2}$ the distance between them.

Or we can model this difference by adding a spin-spin interaction term

$$E_{ex} = -J_{12}\vec{S}_1 \cdot \vec{S}_2 \tag{4.5}$$

which is the so called *Heisenberg Hamiltonian.* J_{12} is called *exchange integral* which is positive for ferromagnetic interaction and negative for antiferromagnetic interaction.

4.1.2 Mean Field Approximation

The total energy of a magnetic system subjected to an external field of H is[50, 51]

$$E_{total} = -\sum_{i,j}{}' J_{ij}\vec{S}_i \cdot \vec{S}_j - \sum_i g\mu_B \vec{S}_i \cdot H \tag{4.6}$$

In the first sum, the case i=j is excluded.

Specifically, we consider the energy that the spin $\vec{S}_i$ is involved, i.e. E_i. By using the mean value of the other spins, $< \vec{S}_i >$, E_i can be written as[50, 51]

$$E_i = -2\sum_j J_{ij}\vec{S}_i \cdot < \vec{S}_j > -g\mu_B \vec{S}_i \cdot \vec{H} = -\vec{S}_i \cdot \vec{H}_i \tag{4.7}$$

where, $\vec{H}_i = 2\sum_j J_{ij} < \vec{S}_j > +g\mu_B \vec{H}$ is the effective field that spin $\vec{S}_i$ feels. This field is sometimes called molecular field, since it includes the exchange interaction the other spins $< \vec{S}_j >$ apply on spin $\vec{S}_i$.

After this treatment, the problem of ferromagnetism has been reduced to the problem of isolated spins (paramagnetism) interacting with an 'applied' field H_i.

In this case, the component of the S_i in the external field direction (z) is written as[50, 51]

$$< S_{z,i} >= S_i B_{S_i}(\frac{SH_i}{k_B T}) = S_i B_{S_i}(\frac{S(2\sum_j J_{ij} < S_{z,j} > +g\mu_B H)}{k_B T}) \tag{4.8}$$

where the *Brillouin function* $B_y(x) = \frac{2y+1}{2y} coth(\frac{2y+1}{2y}x) - \frac{1}{2y} coth(\frac{x}{2y})$. Since there is no difference between S_i and S_j on average, we can written the above equation without the index, i or j

$$< S_z >= SB_S(\frac{S}{k_B T}(2 < S_z > \sum_j J_{ij} + g\mu_B H)) \tag{4.9}$$

If we assume that J_{ij}=J for nearest neighbors and J_{ij}=0 for non-nearest neighbors, we can have

$$< S_z >= SB_S(\frac{S}{k_B T}(2 < S_z > \eta J + g\mu_B H)) \tag{4.10}$$

where η is the number of nearest neighbors.

In a zero external field, we have[50, 51]

$$< S_z >= SB_S(\frac{S}{k_B T}(2 < S_z > \eta J)) \tag{4.11}$$

or

$$M \sim B_S(\frac{S}{k_B T}(2M\eta J)) \tag{4.12}$$

where the magnetization M ($\sim S_z$) is the total z component of magnetic moment in a unit volume.

The temperature dependence of M is approximately drawn in Fig. 4.1. Here, T_c is the so called Curie temperature, above which the system turns to paramagnetism.

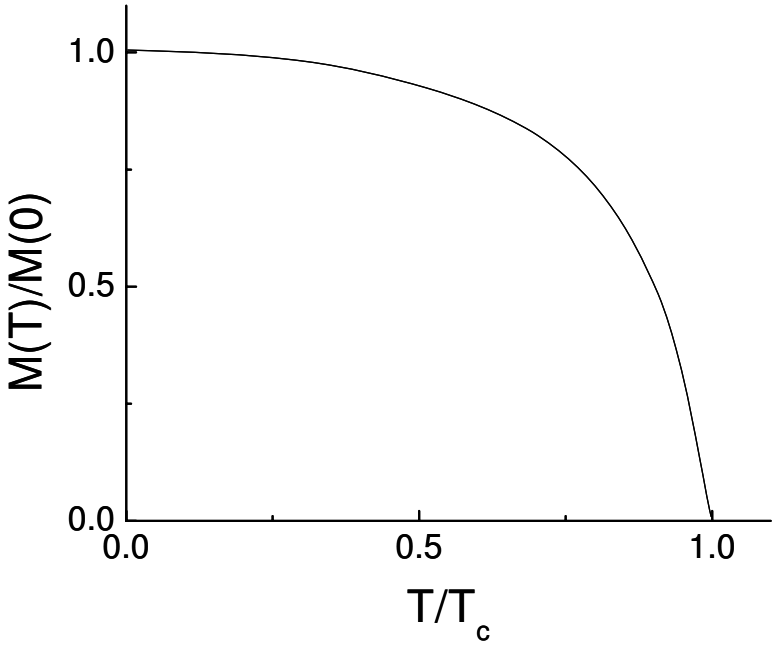

Figure 4.1: Schematic of a temperature dependence of magnetization of a ferromagnetic material in zero field

4.1.3 Magnetic Domains & Hysteresis Curve

In reality, however, without the application of external magnetic field, M is usually zero. The reason for this contradiction is that we have ignored an important fact that magnetic domains form in the system. Fig. 4. 2 shows a schematic picture for magnetic domains. Although the spins inside of individual domain align to the same direction, domains have different magnetic orientation with each other which gives rise to a zero average magnetic moment in any z-direction. Therefore, in normal magnetization measurement, an external magnetic field is applied to align the magnetic domains.

The existence of magnetic domains is a result of the competition between magnetic exchange interaction and magneto-static interaction (the classical dipole

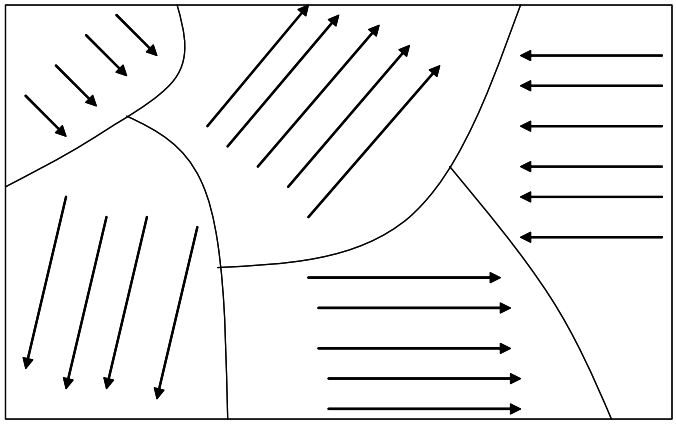

Figure 4.2: Schematic of magnetic domains in a ferromagnetic material

interaction). The details information about this could be found in ref.[50, 51].

The magnetic hysteresis loop (Fig. 4. 3) observed in a ferromagnetic material is an indication of the existence of magnetic domains. Starting from point 'O', the magnetization increases non-linearly with the increase of magnetic field due to the gradual alignment of magnetic domains. At point 'A', almost all of the magnetic domains are aligned and the material has reached the point of magnetic saturation (M_s). When H is reduced to zero ('B'), the magnetization does not drop to zero, but remain a finite value called magnetization remanence (M_r), because some of the magnetic domains remain aligned. As the magnetic field is reversed, the curve moves to point 'C', where the magnetization has been reduced to zero as the reversed magnetic field has flipped all the previously aligned domains so that the net magnetization within the material is zero. This field is called magnetic coercivity (H_c). As the magnetic field is increased in the negative direction, the material will again become magnetically saturated but in the opposite direction (point 'D').

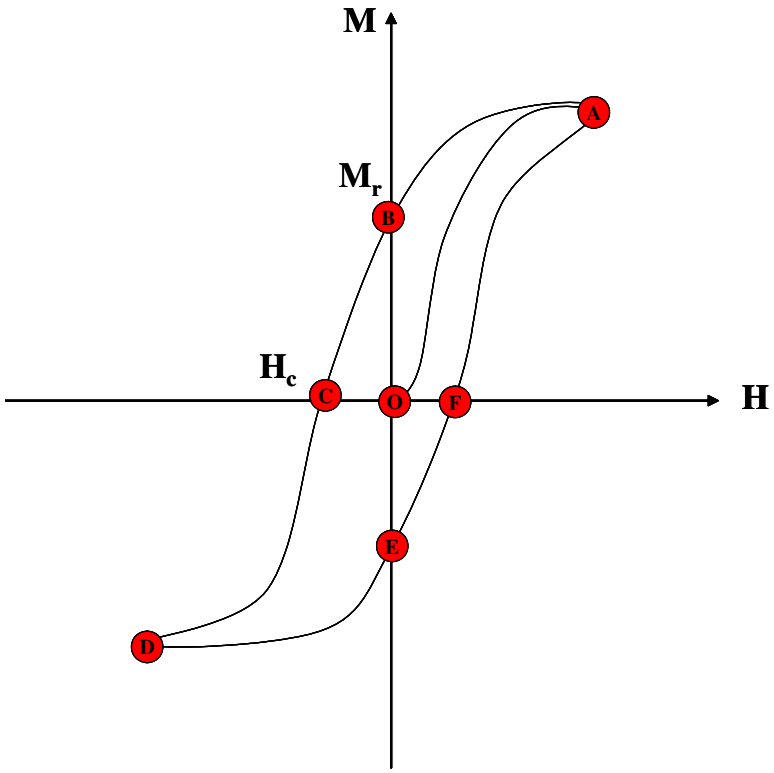

Figure 4.3: Schematic of a magnetic hysteresis loop for a ferromagnetic material

Reducing H to zero brings the curve to point 'E'. It will also have a remanence, which equals to that achieved in the positive direction. Increasing magnetic field back in the positive direction will return magnetization to zero ('F'). The curve moves from "F" back to the saturation point ('A') with the further increase of magnetic field.

4.2 Spintronics

In modern information technology, the charge of electrons is utilized to process information in semiconductors, while the spin degree of freedom is used to store information in magnetic materials. Recently, spin-based electronics (spintronics)[53,

54, 55], combining the charge and spin degrees of freedom have attracted great interest due to the possibility of realizing novel multi-functionality in these systems.

4.2.1 Spin-based Electronic Devices

The best-known spin-based electronic devices are the giant magnetoresistance (GMR) spin valves and magnetic tunnel junctions (MTJ), being commercially used in hard disk read heads and magnetic random access memory(MRAM), respectively. As shown in Fig. 4.4 (a), a spin valve device consists of two ferromagnetic (FM) layers separated by a metallic layer. The magnetic orientation of one FM layer is fixed (not sensitive to magnetic field) and the other one is free to the magnetic field, which can be realized by using materials with different magnetic coercivities. When a beam of electrons enter into the pinning layer, most of the electrons get polarized with their spin orientation parallel to that of the pinning layer. If the free layer, aligned by applied magnetic field, has the magnetic orientation parallel to that of the pinning layer, then these spin-polarized electrons are easy to flow through the free layer. However if the free layer is aligned anti-parallel, with respect to the pinning layer, then the spin-polarized electrons have great chance to be scattered back from the free layer. Therefore, this structure shows changeable resistance depending on the respective magnetic orientation of two FM layers and hence the applied magnetic field.

The magnetic tunnel junction (MTJ) has a very similar structure to the GMR spin valve. However, as shown in Fig. 4.4 (b), an insulating barrier other than

metallic layer is placed between two FM layers. The occurrence of magnetoresistance can be understood by Julliere's model proposed in 1967[56]. In Julliere's picture, the tunneling of up and down spin electrons are two independent processes. Therefore, when two FM layers have the same magnetic alignment, the minority spin electrons and majority spin electrons from the pinning layer tunnel to the minority states and the majority states in the free layer respectively. In contrast, when two FM layers are anti-parallel aligned, the minority spin electrons and majority spin electrons from the pinning layer tunnel to the majority states and the minority states in the free layer respectively. On the other hand, the conductance for a particular spin orientation is a product of the effective density of states of the two FM layer. Therefore, the conductance of the parallel configuration is higher than that of the anti-parallel configuration. The MTJ is used to store information in magnetic random access memory which has great advantage over the traditional random access memory, including the non-volatility.

The ferromagnetic layers in the above two devices are normally metallic. Recently, some novel spintronics devices based on ferromagnetic semiconductors have attracted considerable interest. One of these devices is called spin-based field effect transistor (spin-FET) proposed by Datta and Das in 1990[57]. A schematic picture of a spin-FET is given in Fig. 4.5 (a). The spin-FET consists of a ferromagnetic source and drain separated by a two dimensional electron gas channel. A gate electrode is used to applied an electric field to the channel. The electrons are spin-polarized as they pass through the FM source, and their spin orientation can be modulated by the electric field applied on the channel. If the spin of electrons

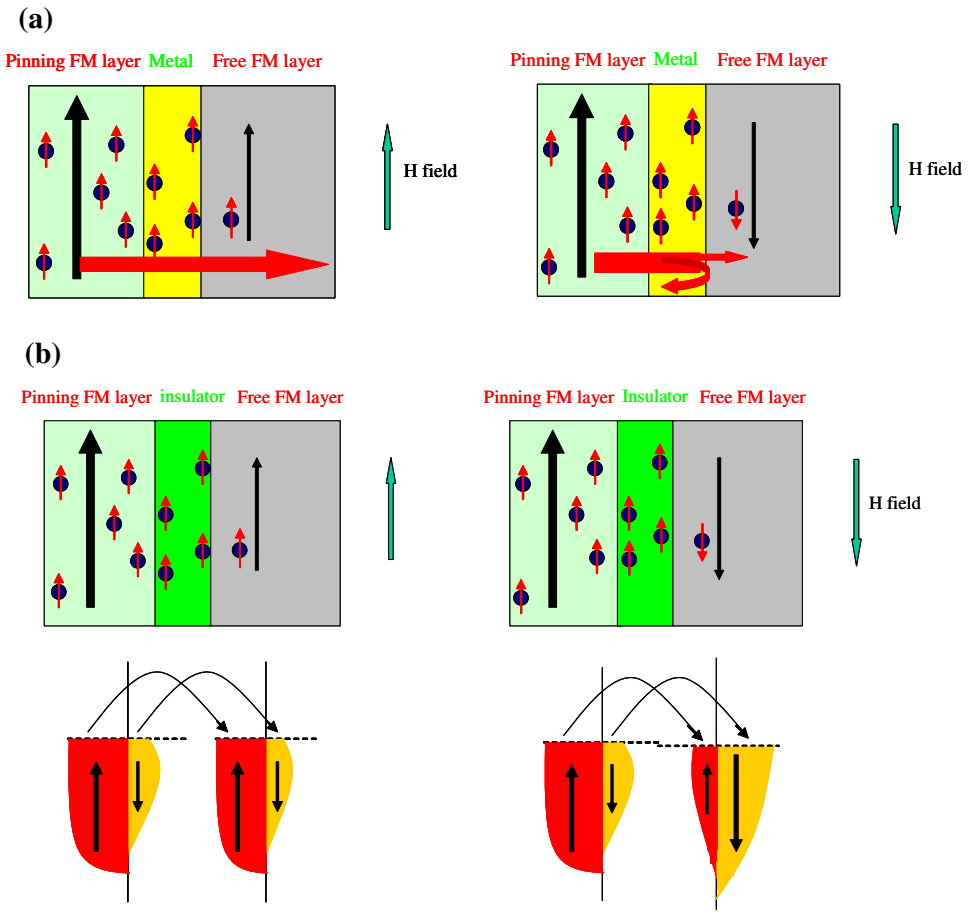

Figure 4.4: Schematic of a (a) GMR spin-valve with two magnetic layers have the same moment orientation (left panel) and the opposite moment orientation(right panel) (b) Magnetic tunnel junction with two magnetic layers have the same moment orientation (left panel) and the opposite moment orientation(right panel); Low panels show independent tunnel process of two spin states.

entering into the drain is parallel to the orientation of FM drain, they can easily pass to the drain. However if the spin of these electrons is anti-aligned with the FM drain, it is very difficult for them to pass through. Therefore, the applied electric field can modify the resistance state of the system. A spin FET has several advantages over a conventional FET in which the density other than the spin polarization is modulated by electric field. For instance, flipping an electron's spin takes much less energy and can be done much faster than pushing an electron away from the channel. It is also possible to change the orientation of FM source or drain by applied magnetic field; therefore another type of control can be realized.

Another type of novel spin-based device is called spin light emitting diode (spin LED)[58]. As we discussed in Chapter 2, when a p-n junction, fabricated by direct band gap semiconductors, is forward biased, the electrons in n-regime move towards the p-regime and the holes in p-regime move towards the n-regime. Once they meet with each, the system falls into a lower energy state and releases energy in the form of photons. While in a spin LED, as shown in Fig. 4. 5(b), the electrons from the ferromagnetic n-semiconductor are spin-polarized, and as they meet the un-polarized holes coming from non magnetic p-semiconductor, polarized photons are hence generated.

4.2.2 Diluted Magnetic Semiconductors

As mentioned above, both spin FET and spin diode requires ferromagnetic semiconductors for proper spin-injection or detection[53, 59]. And even for spin

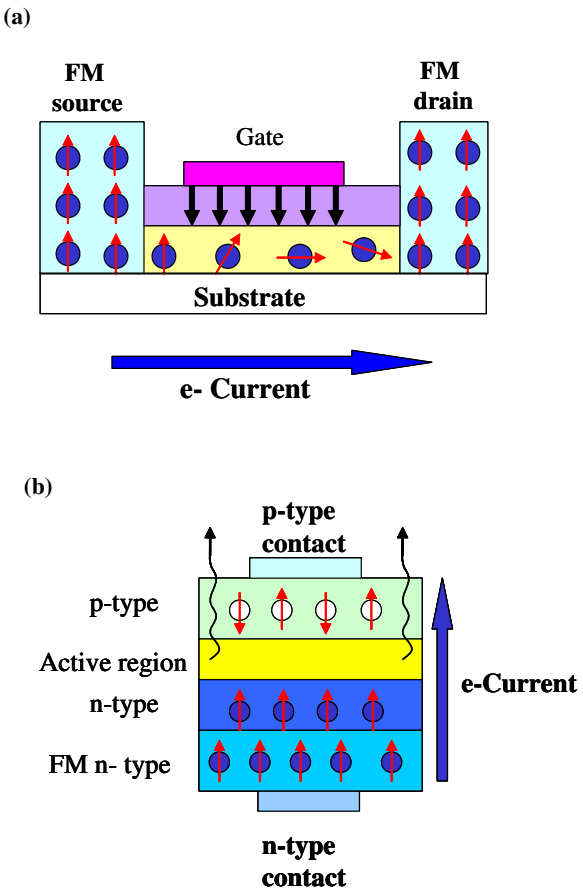

Figure 4.5: Schematic of a (a)spin field effect transistor and (b) spin light emitting diode.

valve and MTJ, FM semiconductors have been suggested to replace traditional ferromagnetic electrodes so as to successfully integrate these devices with silicon-based electronics[60]. Therefore, the search for above RT ferromagnetic semiconductors is an essential way to realize the multi-functional applications for novel spin-based electronic devices.

One main strategy for creating such a system with both magnetic and semiconducting properties is to dilutely introduce local magnetic moments into conventional semiconductors to achieve ferromagnetism without changing the application-worth semiconducting properties of the host[53, 59, 119](shown in Fig. 4. 6). This group of materials, called diluted magnetic semiconductors (DMSs) initiated in the 1970s, only attracted great interest since 1994 when ferromagnetism above 100 K was achieved in manganese doped InAs compound semiconductors[63]. In this type of DMSs, in addition to provide local moment, manganese was found to substitute for the trivalent cation, i.e. Ga, and therefore acts as an acceptor. The origin of the ferromagnetism (FM) is the Ruderman-Kittel-Kasuya-Yosida (RKKY) type of indirect FM coupling (discussed in next section) between Mn d-shell moments mediated by the itinerant holes provided by Mn acceptors[64]. Various functional spin-based electronic devices have been based on these materials[65, 66, 67, 68, 69, 70, 71, 71, 72]. However, the low Curie temperature of this class of materials makes them impossible for real application.

Predictions were made by Dietl et. al[73] for manganese doped semiconductors which could show ferromagnetism due to the magnetic coupling between manganese ions mediated by carriers. It was shown that above room temperature ferromag-

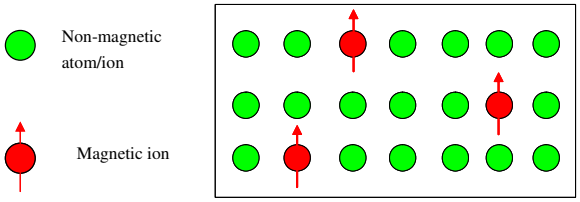

Figure 4.6: Schematic of a diluted magnetic semiconductor

netism can only be realized in GaN and ZnO. The follow up experimental work showed room temperature FM in cobalt doped ZnO, however the reproducibility of the results was less than 10%. Interestingly, another important oxide system, anatase TiO_2[44], dilutely doped with cobalt was reported as a transparent ferromagnetic semiconductor with T_c above room temperature. This observation stimulated a fast growth of research interest in the search for high temperature FM in oxide systems[45, 46, 74, 75, 76, 77, 78, 79, 80, 81, 82, 83, 84, 85, 86]. Some studies on Co: TiO_2 have shown that the achievement of FM strongly depends on the growth conditions[74, 78, 83, 84], i. e. oxygen partial pressure etc., while further work with detailed structural characterization have shown the evidence of cobalt segregation[77, 45, 76] and raised the question whether the FM observed in this system is an intrinsic effect or from extrinsic cobalt metal clusters. Another group claimed that FM in oxide system was due to the formation of defects[85, 86] because FM was only observed in the pulsed laser deposited thin films with fast repetition rate but not in the defect-free molecular beam epitaxy films. Moreover, ferromagnetism was even observed in some un-doped oxide systems grown at highly reduced condition and oxygen deficiency was considered as the origin of FM[87].

These controversies in oxide-DMS are not yet resolved.

4.2.3 Theoretical Models on the Origin of Ferromagnetism

Due to the low concentration of magnetic dopants in diluted magnetic semiconductors, the direct exchange interaction between magnetic moments, requiring overlap of electron wave functions, as in conventional magnetic metals is not applicable. Therefore, two indirect exchange interaction models, namely RKKY model[64] and bound magnetic polaron model[85, 88, 89], were proposed to explain this unconventional FM in DMS. The RKKY interaction deals with conducting systems having considerable delocalized carriers, while the bound magnetic polaron model deals with the highly insulating systems. In the rest of this chapter, I present some qualitative and brief introduction to these two models.

4.2.3.1 RKKY Interaction

The Ruderman-Kittel-Kasuya-Yosida interaction[90, 91, 92] refers to a coupling mechanism of localized d shell electron spins in a conductor in terms of an interaction through the conduction electrons: when the conduction carriers are temporarily around a localized magnetic moment, the spins of the carriers are polarized by this magnetic moment. As the spin polarized carrier moves through the lattice, it interacts with another magnetic moment. As a result, these two magnetic moments interplay with each other through the conduction electrons[93].

This interaction was initially proposed by Ruderman and Kittel [90] in 1954.

They proposed that the indirect exchange coupling between two nuclear spins by the conduction electrons have the following relation

$$H = -JI_iI_j = -\frac{2\pi}{9}n^2\frac{A^2}{\varepsilon_F}(I_iI_j)F(2k_Fr_{ij}) \tag{4.13}$$

$$F(x) = \frac{-x\cos x + \sin x}{x^4} \tag{4.14}$$

where H represents the Hamiltonian, n is the number of conduction electrons per atom, A represents the strength of the hyperfine interaction between two nuclear spins, ε_F is the Fermi energy, I_i, I_j are the nuclear spins, k_F is the Fermi wave vector, r_{ij} is the distance between two nuclear spins.

Later, Kasuya proposed that the localized inner d-electron spins can interplay with each other via conduction electrons through a relation similar to eq. 4.13[91].

$$H = -JS_iS_j = -\frac{2\pi}{9}n^2\frac{J_{sd}^2}{\varepsilon_F}(S_iS_j)F(2k_Fr_{ij}) \tag{4.15}$$

where, S_i, S_j are the localized magnetic moments, J_{sd} is the s-d exchange constant.

Furthermore, Yosida pointed out that the interaction given by eq. 4.15 can induce spin polarization of the conduction electrons around the localized magnetic spins and showed that the spatial distribution of the spin polarization of the conduction electrons can be described by eq. 4.15[92].

As shown in Fig. 4.7, the RKKY exchange coefficient J, oscillates from positive to negative as the separation of the ions changes and has the damped oscillatory

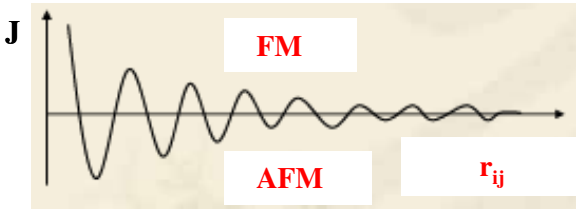

Figure 4.7: The indirect exchange coupling constant J as a function of the distance r_{ij} between two localized magnetic moments i and j

nature. Therefore, depending upon the separation between a pair of ions their magnetic coupling can be ferromagnetic or antiferromagnetic.

In semiconductors, considerable conduction carriers can be introduced by means of extrinsic doping, and work as an medium for the exchange interaction between magnetic moments.

4.2.3.2 Bound Magnetic Polarons

As discussed in Chapter 2, in an insulating semiconductor, the electrons or holes, induced by extrinsic dopants, are loosely bound within a range of $\sim r^*_H$ distance from the dopant sites. If a local magnetic moment falls to the area about which the carrier is localized, an exchange interaction between the carrier and the magnetic moment leads to the polarization of carrier (the spin of carrier is aligned)[88, 89]. This picture is sometimes called F-center model[85] as the carriers are induced by the deficiency of anions, i. e. oxygen vacancy etc. As the concentration of the magnetic moments increases, two or more magnetic atoms/ions fall into the carrier localized area, and indirectly interact with each other through the polarized carrier.

Meanwhile, with a increase of magnetic polaron density, a short range ferromagnetic (or anti-ferromagnetic) state can form due to the overlap of polarons. And further increase of this density leads to the establishment of percolative path and formation of a long range magnetic ordering.

This bound magnetic polaron model is being widely used to explain the high temperature ferromagnetism observed in oxide DMS showing highly insulating behavior. In those oxide systems, the dielectric constant ϵ is very high ($10 \sim 100$), which gives rise to a large hydrogen-like radius $r^*_H = m/m^*\epsilon a_0$ (m^* is the effective mass of carriers, m is electron mass and a_0 is the Bohr radius). Moveover, the localized carriers arise from the oxygen vacancies created by magnetic dopants, hence the localized carrier produced by oxygen vacancy is close to the magnetic atoms/ions (for example, when cobalt substitutes into titanium in TiO_2, one cobalt creates two oxygen vacancies nearby in order to satisfy the local charge neutrality)[46]). Therefore, even the magnetic dopants dilutely disperse in the matrix of the host, there are some chances for the magnetic polarons to overlap with each other and generate ferromagnetic ordering.

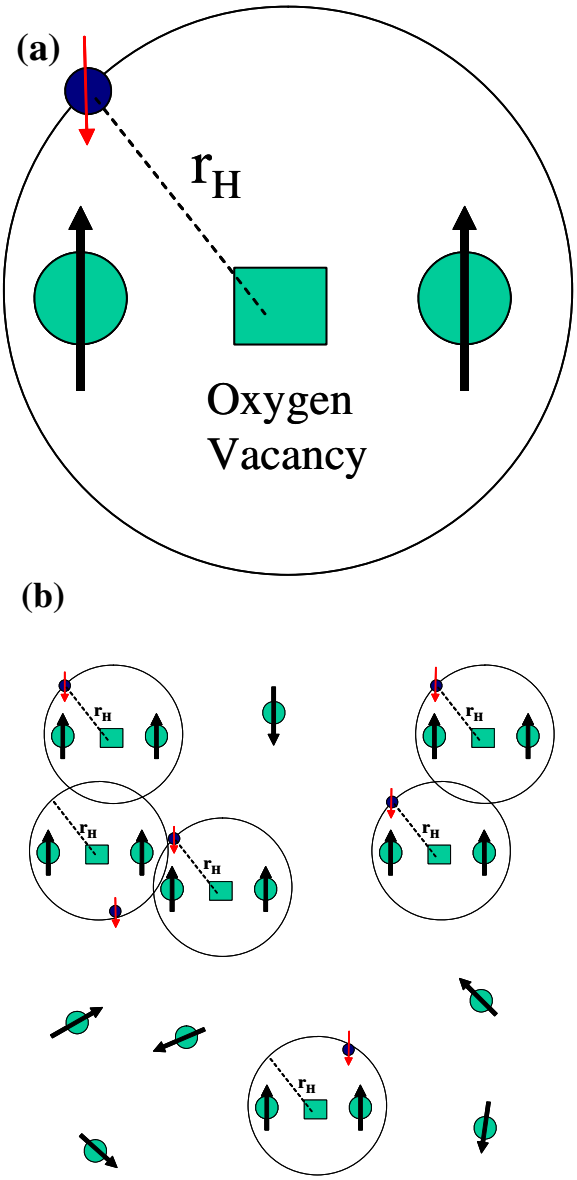

Figure 4.8: Schematic of the bound magnetic polaron model. (a) a single magnetic polaron. the light green square denotes a F-center, the light green circle with black arrow represent a localized magnetic moment, the small blue circle with red arrow indicates the localized carrier, and the large circle shows the area by which a carrier is localized. (b) the overlap of magnetic polarons.

Chapter 5

Niobium and Cobalt Dual Doped TiO_2: an RKKY Motivation

5.1 Motivation

As briefly discussed in the previous chapter, the microstructure of Co:TiO_2 films and the growth sensitivity of the corresponding FM state observed in different works possibly relates to the controllability of oxygen in the films[74, 78, 83, 84]. This has also led to an improved recognition of the relevance and possible significance of different defect types such as a neutral oxygen vacancy, an F-center etc. and the related new mechanisms, i. e. bound magnetic polarons model or F-Center model[85, 89]. Since oxygen pressure influences the defect states as well as the carrier density in anatase TiO_2, it has been difficult to isolate and thereby control the corresponding effects in films. In order to investigate the carrier concentration effects on the ferromagnetism in this system (an RKKY approach), it is important to control the carrier concentration via an independent way. Indeed, the modulation of FM in Co: TiO_2 through an electric gate has been realized[94]. However, it is of interest to examine another channel, such as chemical doping, to control the carrier density independently. As shown in Chapters 2 and 3, niobium doping can dramatically improve the conductivity of TiO_2 by introducing a large number of electrons into the its conduction band. Therefore, interesting modulation of electronic transport and magnetism of TiO_2 through dual doping of niobium and

cobalt can be expected.

5.2 Experimental Results

5.2.1 Sample Preparation

Thin films of anatase $Ti_{1-x-y}Co_xNb_yO_{2-\delta}$ (x=0.03, and y=0.0, 0.01) studied in this work were grown on $LaAlO_3$ (LAO) by pulsed excimer laser deposition (KrF, λ =248 nm) at 875 ^{0}C at different oxygen partial pressures (10^{-5} and 10^{-4} Torr). The laser energy density was $\sim$ 2 J/cm^2 and the repetition rate was 10 Hz.

5.2.2 Structure and Chemical Distribution

Fig. 5. 1(a) shows a typical XRD pattern observed for the $Ti_{1-x-y}Co_xNb_yO_{2-\delta}$ (x=0.03, and y=0.01)films. Only (00l) family of anatase film peaks are seen, in addition to the (LAO) substrate peaks. No major secondary contributions can be noted even on the log scale, suggesting phase purity. The rocking curve on the main film peak (as shown in the inset of Fig 5.1 (a)) has full width at half maximum (FWHM) of 0.22^0 which shows the high degree of orientation order of the film. Similar general characteristics were seen for all the films grown under the stated conditions, indicating their optimal nature.

Fig. 5. 1 (b) shows the RBS (Random and channeled) spectra for the $Ti_{0.96}Co_{0.03}Nb_{0.01}O_{2-\delta}$ film. The elemental positions are indicated on the spectra. The Ti minimum channeling yield (χ_{min}%) of about 8% seen in this spectrum for a Nb doped film is possibly the smallest reported thus far in the Co: TiO_2 system,

suggesting very high dopant substitutionality and very small distortion disorder. Interestingly, the random and channeled RBS spectra for $Ti_{0.97}Co_{0.03}O_{2-\delta}$ film without niobium doping (not shown) indicate a higher distortion disorder with the Ti minimum channeling yield ($\chi_{min}\%$) of almost 38%. These data indicate the interesting role of Nb dopant in rendering a higher quality film growth and enhancing the degree of dopant substitutionality.

Fig. 5. 2 (a) shows a typical transmission electron micrograph for the $Ti_{0.96}Co_{0.03}Nb_{0.01}O_{2-\delta}$ sample. The micrograph (which is deliberately shown on a coarser length scale to bring out the presence or absence of any distributed clusters) is clearly very smooth and featureless, and no clusters of any kind are seen. The high resolution micrograph of the interface (Fig. 5. 2 (b)) ensured the epitaxy and high interfacial quality of the film growth consistent with the RBS channeling data. In Fig. 5. 2 (c) we show the high resolution micrograph of the surface region of the film (which is of interest for reasons discussed below) and it shows a highly crystalline character. The distribution of Co in the film was studied by probing the film via tens of electron energy loss spectroscopy (EELS) line scans across the sample starting with recording one signal on the $LaAlO_3$ substrate and subsequently probing the film in 5 nm steps in direction of the film surface. The range of energy for the line scan experiments was from 150 eV to 870 eV in order to include the signals of niobium, titanium, oxygen, cobalt and lanthanum. A typical series of line scans covering oxygen, cobalt and Lanthanum contributions is presented in Fig. 5. 2 (d). The single scans are shifted in the y-direction for clarity. Proceeding from lower to higher counts in the graph (as indicated by the arrow in Fig. 5. 2 (a)), the first

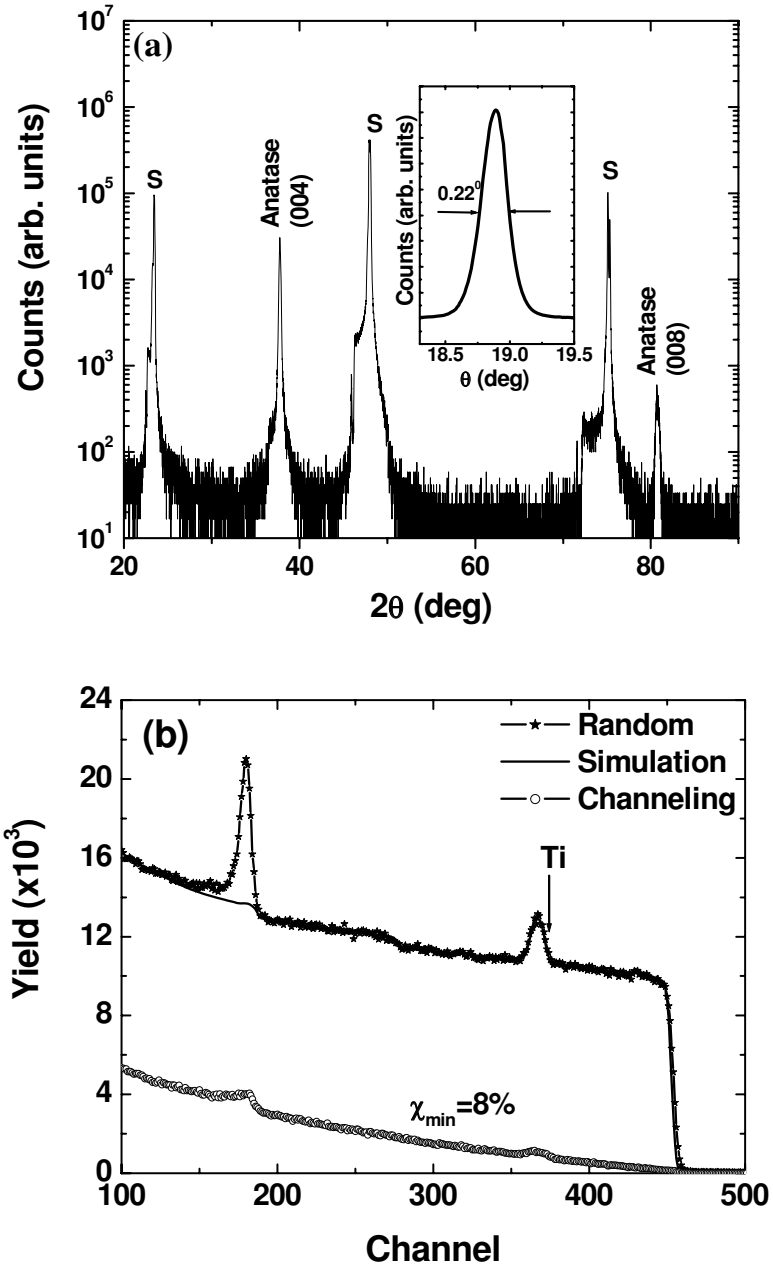

Figure 5.1: (a) The θ-2θ XRD spectrum for a $Ti_{0.96}Co_{0.03}Nb_{0.01}O_{2-\delta}$ film on $LaAlO_3$ (001). Peaks labeled "S" correspond to the substrate. The inset shows the XRD rocking curve for the film. (b) The 1.5-Mev He+ Rutherford backscattering (RBS) random, simulation and channeling spectra for the $Ti_{0.96}Co_{0.03}Nb_{0.01}O_{2-\delta}$ film.

signal has been recorded on the $LaAlO_3$ substrate and includes the O K-edge at 532 eV and the La M_5-edge at 832 eV etc. The oxygen signal for the following spectra changes owing to the change in material by crossing the interface and being recorded on the cobalt doped TiO_2 film. In addition, the La M_4, M_5-edge disappears while the Nb and Co signals are present consistently in the film. Remarkably, the cobalt signal was found only in the top $\sim$ 15 nm surface layer of the sample. Also, the white lines for the Co $L_{2,3}$-edge have been observed at 795 eV and 780 eV respectively implying an oxidized state of Co and the creation of oxygen vacancies in the film. Notably the oxygen signal in these surface layers is also different than the signal in the deeper layers of the film with its strength also reduced, implying enhanced oxygen vacancy concentration. Substitution of Co^{2+} for Ti^{4+} is indeed expected to add oxygen vacancies for local charge neutrality[46]. This suggests the presence of a uniform surface layer phase wherein cobalt is highly enriched as compared to the mean intended concentration. In Fig. 5. 2 (e) we show the EELS line scans (again appropriately shifted for clarity) for the Nb and Ti contributions. It can be seen that the niobium signal is fairly uniform across the films thickness, except for the surface layer wherein the signal diminishes. It seems that niobium doping affects the charge balance of the local complex comprising of the substituted cobalt and the nearby oxygen vacancy, thereby driving cobalt out towards the surface. Notably this concurrently leads to a drop of Niobium concentration in the surface region. In this sense cobalt and niobium may not be entirely compatible ions for uniform dual doping in anatase TiO_2.

The thin film of $Ti_{0.97}Co_{0.03}O_{2-\delta}$ has also been studied using the STEM tech-

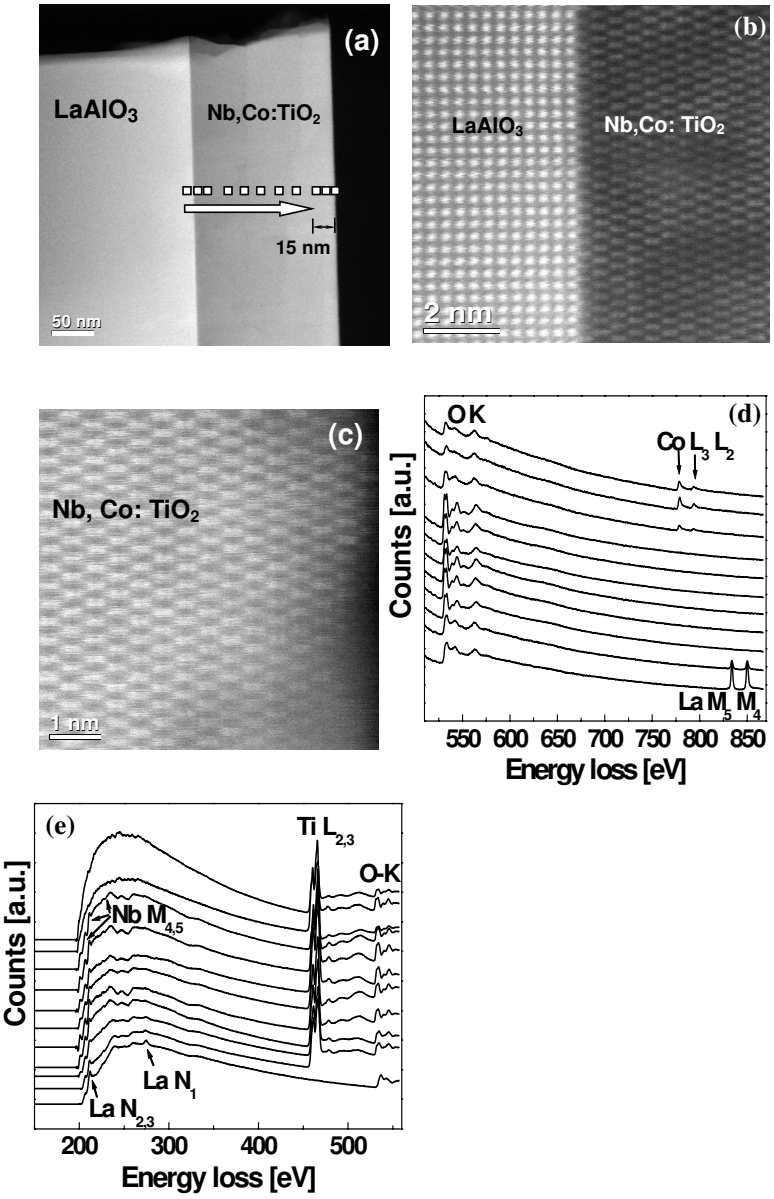

Figure 5.2: (a) Cross sectional TEM images at large length scales of the $Ti_{0.96}Co_{0.03}Nb_{0.01}O_{2-\delta}$ film grown on $LaAlO_3$ (001) substrate. (b) High resolution TEM image for the interface between the film and substrate. (c) High resolution TEM image for the Cobalt-rich surface layer of the film. (c) & (d) EELS line scans across the cross section of this sample.

niques. Figure 5. 3(a) shows a typical STEM Z-contrast micrograph for this sample on a coarser length scale. In the micrograph, some nanoparticles with the size of 10 $\sim$ 40 nm can be seen in the thin film, mostly at the interface. The distribution of cobalt in the film and the composition of clusters were also studied by EELS scans. A typical such series of EELS scans is presented in Fig. 5. 3(b). EELS analysis on each particle confirms the existence of Co elements in these nanoparticles, as shown in the spectra labeled 5 $\sim$ 7. The intensity of Co signals increases with the increasing size of clusters. There are also Ti and O signals in these clusters which possibly come from an overlaying of the Co-rich nanoparticles on the anatase TiO_2 matrix. The valence state of cobalt in these particles is found to be +2.6, indicating cobalt is in oxide form. However, EELS spectrum (inset of Fig. 5. 3 (b))taken on the particles with size of 50-100 nm occasionally observed on the film surface only show a strong Co signal without any O and Ti signals, indicating that cobalt forms in metallic state.

5.2.3 Magnetism and Conductivity

Fig. 5. 4 (a) compares the room temperature magnetic hysteresis for $Ti_{1-x-y}Co_xNb_yO_{2-\delta}$ (x=0.03 and y=0.0) and $Ti_{1-x-y}Co_xNb_yO_{2-\delta}$(x=0.03 and y=0.01) films, i.e. for 3% cobalt doped anatase TiO_2 films without and with 1 % Nb doping grown at an oxygen pressure of $\sim 10^{-5}$ Torr (Note that substrate signal has been subtracted). Although both samples exhibit ferromagnetism, Nb doping is observed to suppress the magnetization considerably. Indeed the saturation moment (M_S)

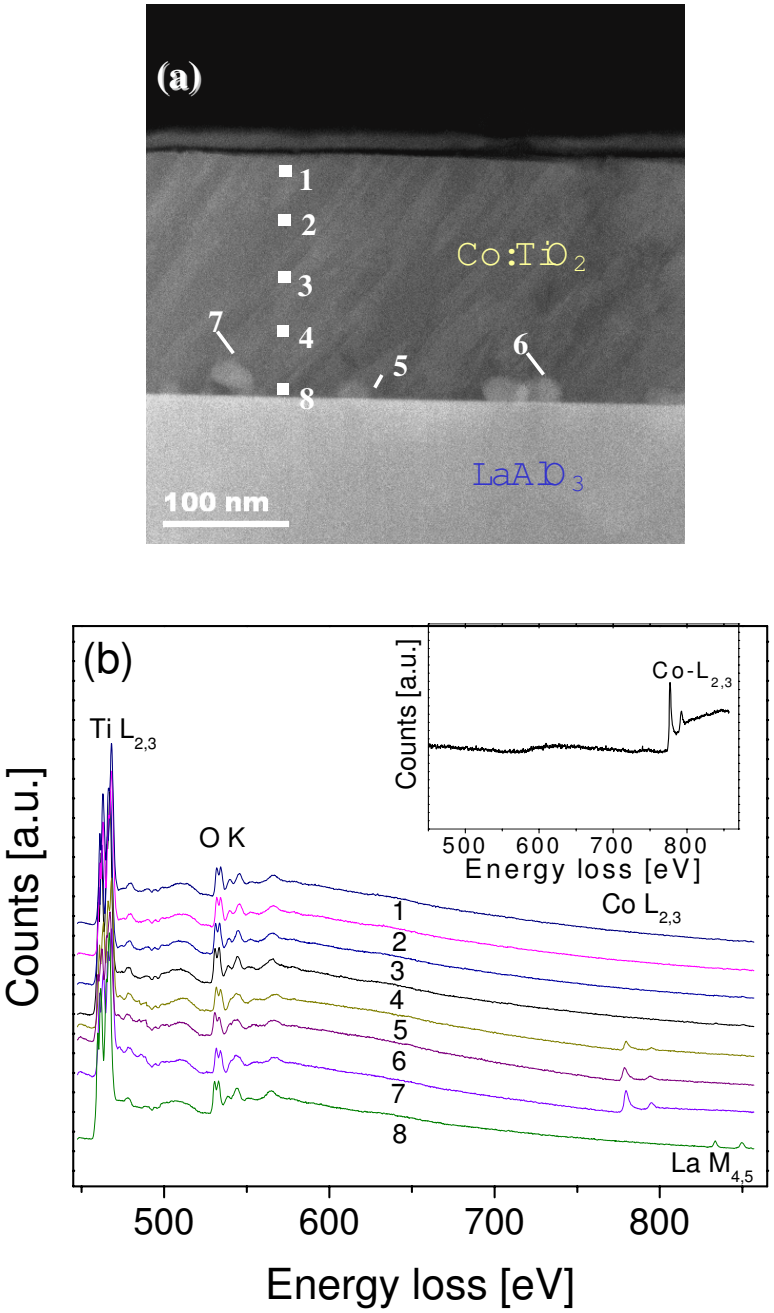

Figure 5.3: (a) A cross-sectional STEM Z-contrast image of the $Ti_{0.97}Co_{0.03}O_{2-\delta}$ thin film at a large length scale showing the existence of nanoparticles. (b) The EELS scans acquired across the thin film and on the nanoparticles showing that Co is rich in these particles. The inset shows a typical EELS spectrum of the particles occasionally observed on the film surface

and coercive field (H_C) values drop from $\sim$ 0.38 μ_B/Co and $\sim$ 300 Oe to about $\sim$ 0.15 μ_B/Co and $\sim$80 Oe, respectively. In order to bring out the possible role of the carriers (electrons) known to be contributed by Nb to anatase TiO_2, we compared the resistivity for the 3% Co:TiO_2 films without and with 1% Nb doping. The corresponding data are shown in Fig. 5. 4 (b). As expected, it is seen that the resistivity of the film with Nb doping is orders of magnitude lower than the film without Nb, and the Nb doped film is also metallic as against the semi-insulating nature of the film without Nb. This result emphasizes the shallow donor nature of the Nb level in anatase TiO_2 as discussed in Chapter 2.

In order to explore the connection between oxygen stoichiometry, resistivity and magnetization, further we compared these physical properties for the $Ti_{1-x-y}Co_xNb_yO_{2-\delta}$ (x=0.03 and y=0.0) and $Ti_{1-x-y}Co_xNb_yO_{2-\delta}$ (x=0.03 and y=0.01) films grown at a higher oxygen pressure of 10^{-4} Torr. The magnetization data (Fig. 5. 5(a)) exhibit a very interesting reversal of signal strength as compared to the case of films grown at 10^{-5} Torr. The Co: TiO_2 film without Nb doping loses all the FM, The negative magnetization shown in the inset of Fig. 5.5 (a) is only due to the diamagnetic contribution of LAO substrate, while the FM does occur for the Co:TiO_2 film with Nb doping, albeit with a reduced moment. The M_S value for Nb doped Co:TiO_2 film grown at 10^{-4} Torr is $\sim$ 0.07 μ_B/Co, smaller by a factor of two as compared to that for the film grown at 10^{-5} Torr, namely $\sim$ 0.15 μ_B/Co. The value of H_C on the other hand is not seen to change significantly. The resistivity data for the films grown at 10^{-4} Torr are shown in Fig. 5. 5 (b). Growth at this higher pressure imparts a highly insulating character to the Co:TiO_2 film without

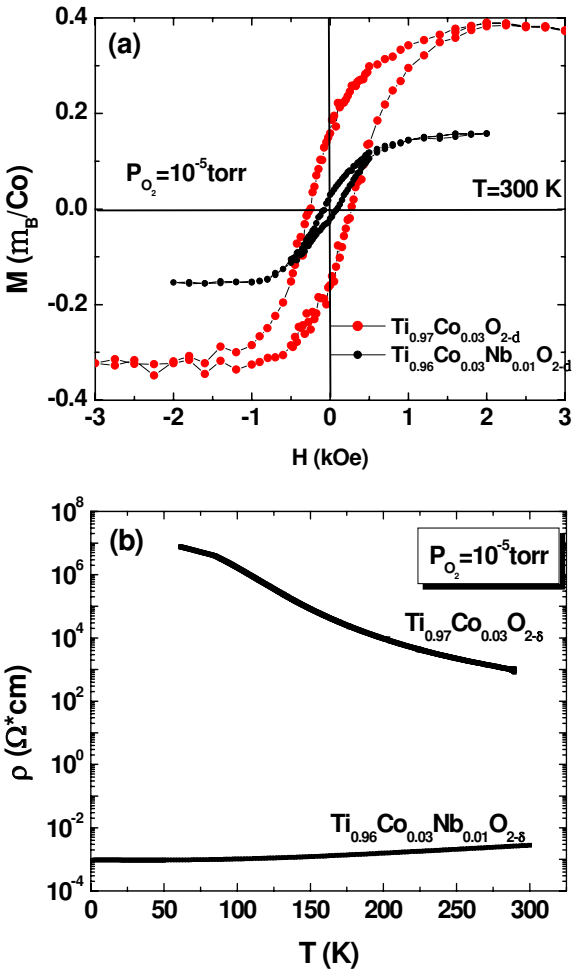

Figure 5.4: (a) Magnetic hysteresis loops for the $Ti_{0.97}Co_{0.03}O_{2-\delta}$ (red circles) and $Ti_{0.96}Co_{0.03}Nb_{0.01}O_{2-\delta}$ (black circles) films grown at oxygen pressures of 10^{-5} Torr; (b) Resistivity vs temperature of the two samples in (a);

Nb doping, making it impossible to perform a proper four probe resistivity measurement (therefore data are not shown). The room temperature resistivity for the Co:TiO_2 film with Nb doping is also seen to increase from 0.0028 Ω cm for growth at 10^{-5} Torr to 0.014 Ω cm for growth at 10^{-4} Torr; yet the metallic behavior is seen to have been preserved.

5.3 Summary

Niobium doping has been found to greatly improve the conductivity of Co:TiO_2 as well as modulate the corresponding magnetization. The electrons thus contributed by Nb doping appear responsible for the changes to the magnetization. The chemical role of Nb in causing surface enrichment of cobalt should then be compounded with its role of electron source in controlling the degree of these effects. This observation of the influence of chemically induced carrier manipulation on ferromagnetism is interesting and can be compared with that of the electric field induced manipulation of ferromagnetism reported recently using a field effect configuration. However, the chemical manipulation is easier from the processing standpoint as compared to the FET device fabrication if it enables realization of the desired property goal. Also, as seen in the present case, introduction of an extra dopant can potentially modify the local charge and chemical balance and lead to dopant redistribution effects.

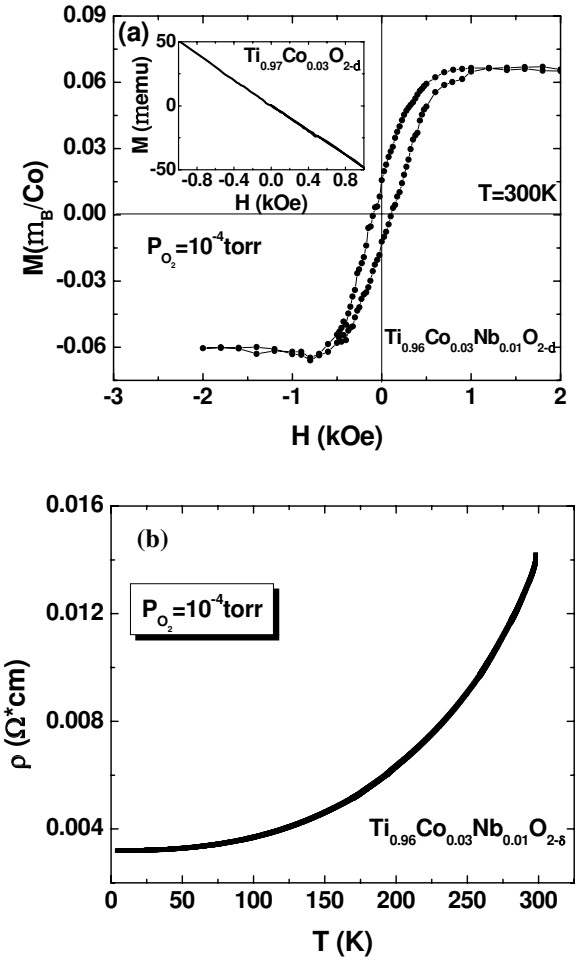

Figure 5.5: (a) Magnetic hysteresis loop for the $Ti_{0.96}Co_{0.03}Nb_{0.01}O2-\delta$ film grown at oxygen pressures of 10^{-4} Torr. The inset shows the non-magnetic behavior (diamagnetism of substrate) of the $Ti_{0.97}Co_{0.03}O_{2-\delta}$ sample grown at 10^{-4} Torr; (b) Resistivity vs temperature of the $Ti_{0.96}Co_{0.03}Nb_{0.01}O2-\delta$ film grown at oxygen pressures of 10^{-4} Torr.

Chapter 6

$SrTiO_3$ (STO)-based DMS

6.1 Overview

Another titanium-based oxide in which we have tried to explore ferromagnetism by magnetic doping approach is strontium titanium oxide ($SrTiO_3$). $SrTiO_3$ has a well known perovskite structure[95] as shown in Fig. 6.1. Each Sr atom is in the corner of a cubic with the lattice parameter a = 3.905 $\mathring{A}$, and the Ti atom, at center of the cubic, is octahedrally coordinated with six oxygen atoms. The simple perovskite structure of $SrTiO_3$ makes it an important substrate for the growth of various type of oxide thin films.

Stoichiometric $SrTiO_3$ (STO) is a band insulator[96, 98], while with oxygen deficiency[97, 99], lanthanum [100]or niobium doping[40, 101], it becomes a good conductor and even a superconductor[99, 40]. The idea of doping $SrTiO_3$ films with transition metals for the goal of ferromagnetism was introduced by Zhao et al.[82]. They doped both lanthanum and cobalt into STO, with the idea of introducing carriers by lanthanum and local spins by cobalt. A ferromagnetic behavior with a Curie temperature of $\sim$ 450 K was found in some of their Co-(La, Sr)TiO_3 (Co-LSTO) thin films. The results were reproduced by Ranchal et al.[102]. Furthermore, Herranz et al.[103] reported a spin polarization of about 80% in Co-LSTO, which supports the intrinsic nature of DMS-FM in this system. Since the insulating $LaTiO_3$

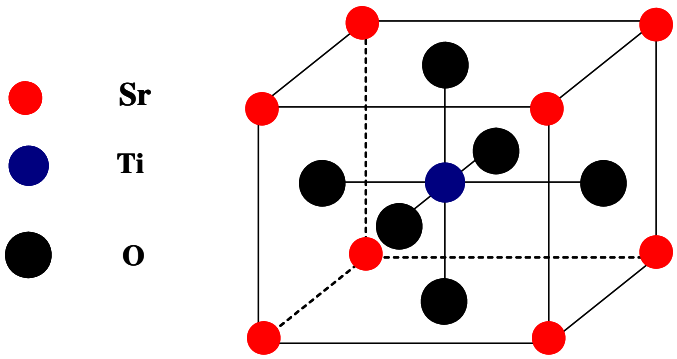

Figure 6.1: Schematic for the lattice structures for $SrTiO_3$ at room temperature

and $SrTiO_3$ do not show any FM when doped by magnetic elements[104], the FM in conductive Co-LSTO is attributed to carrier effects. Indeed, Inaba et al.[105] have suggested FM exchange interaction between Cr spins via carriers (RKKY origin) in the Cr doped (LaSr)TiO_3 system, which is further evidenced by their high-resolution photoemission spectroscopy results[106]. It should be noted that the observation of FM in doped (La,Sr)TiO_3 has a strong dependence on the growth condition, especially oxygen partial pressure[82, 102, 103].

6.2 Search for FM in Nb: $SrTiO_3$ with Transition Metal Dopants

6.2.1 Motivation

The initial achievement of ferromagnetism in Co-LSTO have attracted considerable interest, because the simple perovskite structure of STO is an advantage for film growth and lends itself to epitaxial integration with many functional oxides such as manganites or multiferroics. An interesting question is also raised: can ferromag-

netism be induced in magnetically doped $SrTiO_3$ by other means of carrier doping? As discussed in section 6. 1, niobium, as a donor impurity, can also introduce large number of carriers into STO conduction band. Although this is similar to La doping, it should be noted that La substitutes Sr (rare earth site) while Nb substitutes Ti. Therefore it is of great interest to examine the possibility of FM interaction in magnetic transition element (MTE: Cr, Co, Fe, Mn) doped conducting Nb:STO in order to further understand the mechanism of FM in STO based DMS.

6.2.2 Sample Preparation and Microstructure Characterization

The 2% MTE (Cr, Co, Fe, Mn) and (0.5%, 1%) niobium dual doped $SrTiO_3$ thin films were grown on $LaAlO_3$ (001) (LAO) by pulsed excimer laser deposition (KrF, λ =248 nm, ε =2 J/cm^2, and f =10 Hz). The oxygen partial pressure of $\sim 10^{-6}$ Torr is used because ferromagnetism is observed in Co-LSTO grown at the same pressure. The temperature is set at 870 ^{0}C in order to obtain high quality thin films.

A typical x-ray diffraction (XRD) pattern for a dual doped film on LAO is shown in Fig. 6.2 (a). No impurity phase is present and the film orientation is (001) with a perovskite structure. The rocking curves has a full width at half maximum (FWHM) below 0.20^0 for all the films indicating a high degree of crystallinity. Moreover, with increasing niobium concentration the (002) film peak is seen to shift to lower 2θ (not shown) implying increase of lattice parameter c and substitutional incorporation of niobium into the STO lattice.

Rutherford backscattering data confirm the excellent quality of our thin films. Fig. 6.2 (b) and (c) show the RBS (random and channeled) spectra for 2%Cr, 0.5%Nb and 2%Co, 0.5% Nb doped $SrTiO_3$ films, respectively. The elemental positions are indicated on the spectra. The strontium minimum yield for Co doped one is 8 %, and for Cr doped one is even lower (4.5%), indicating high dopant substitutionality and small lattice distortion disorder. The pure niobium doped STO films prepared at the same condition recently by our group showed a similar minimum yield[107], which means that the quality of the thin films is not affected by magnetic transition element doping.

Fig. 6.3 (a) shows the scanning transmission electron microscopy (STEM) Z-contrast imaging for the 2%Cr, 0.5% Nb doped STO thin film, which is featureless and without any clusters. The difference of lattice parameters between film and substrate leads to strain effect as seen in this micrograph, similar to the case of our Nb: $SrTiO_3$ samples[107]. The high resolution micrograph shown in Fig. 6.2.2 (b) also brings out the epitaxy and good interfacial quality of the film consistent with the RBS channeling data.

The uniformity of elemental distribution in the film was studied by probing the film cross section via tens of EELS line scans (with a spatial resolution of $\sim$ 0.4 nm) starting from the LAO substrate and scanning in the direction of the film surface. A typical series of line scans covering oxygen and chromium (shifted in the y-direction for clarity) is presented in Fig. 6.3 (c). The first two signals (bottom two lines) were recorded on LAO and the interface, respectively, while the rest in the film region. Fig. 6.3 (d) shows the EELS analysis covering lanthanum, strontium,

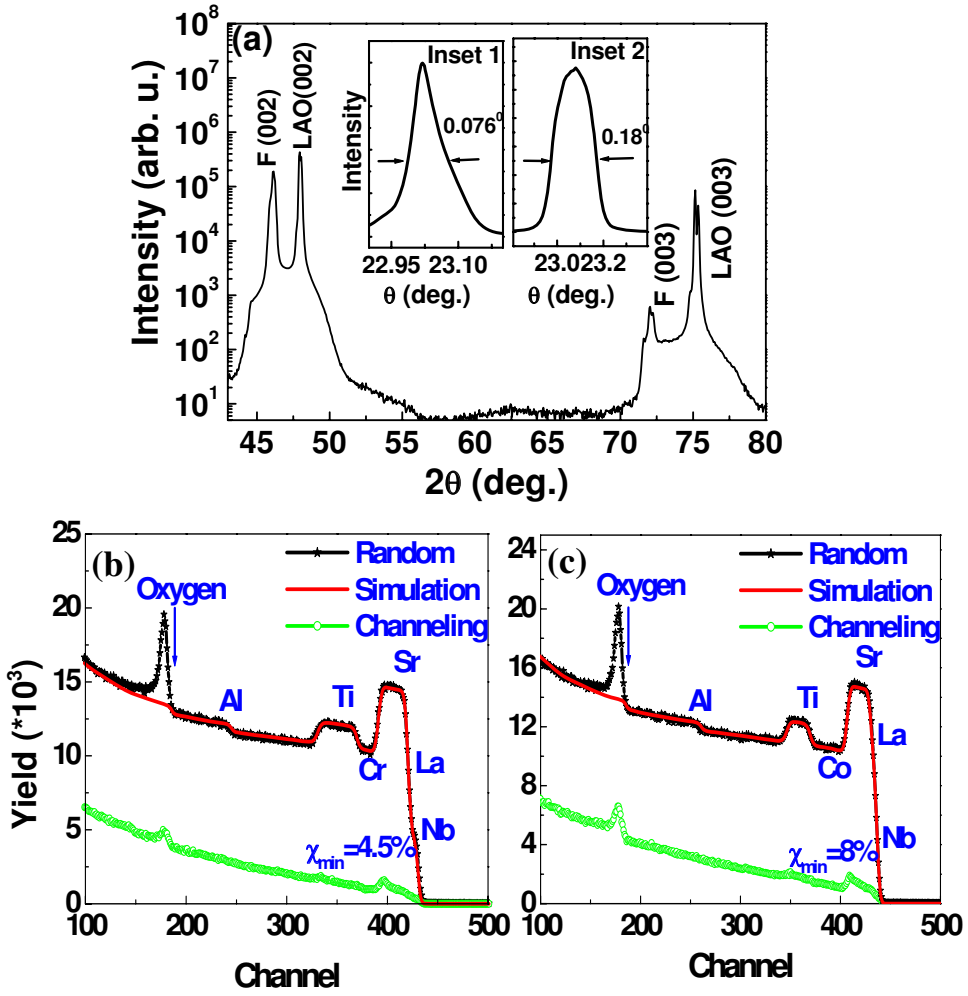

Figure 6.2: (a) A typical θ-2θ XRD pattern for 2%MTE, Nb: STO thin films on $LaAlO_3$ (001). Peaks labeled "F" correspond to the film. Inset 1 shows the XRD rocking curve for a thin film with chromium doping. Inset 2 shows rocking curve for a cobalt doped one. (b) and (c) 3.05-Mev He^+ Rutherford backscattering (RBS) random, simulation and channeling spectra for the 2%Cr, 0.5%Nb doped STO and 2%Co, 0.5%Nb doped STO thin films respectively.

titanium, oxygen and niobium contributions. As the probe crosses the interface, the La $N_{2,3}$, N_1-edge disappears while the Ti $L_{2,3}$, Sr $M_{2,3}$, and Nb $M_{4,5}$ -edges are present consistently in the film. The intensity of each signal does not change inside of the thin film, indicating a uniform distribution of all the elements. Similar STEM and EELS results also obtained in other samples suggest that these thin films indeed have very good quality with all elements uniformly distributed in the lattice and they are free of any type of clusters.

6.2.3 Magnetism and Conductivity

The temperature dependence of resistivity for 2% MTE, 0.5%Nb: $SrTiO_3$ and 2%MTE, 1%Nb: $SrTiO_3$ are given in Fig. 6.4 (a) and (b), respectively. Clearly, Nb doping induces conductivity in STO. For 0.5% Nb doping, only the cobalt doped film shows semiconductor behavior over the entire temperature range, while the other three samples show metal to semiconductor transition at around 120 K during cooling. For 1%Nb doping (Fig. 6.4 (b)), all four samples show metal to semiconductor transition during cooling. Although no obvious shift of transition temperature is seen, the resistivity of each film is much lower than that for the corresponding 0.5% Nb doping case.

Though the samples show excellent quality and good conductivity, it is found that none of them exhibit any ferromagnetism from 365 K down to 5 K. Fig 6.2.3 (a) shows the typical field dependence of magnetization obtained at 300 K, 100 K. Obviously, no FM is observed, the linear negative signal being the diamagnetic substrate

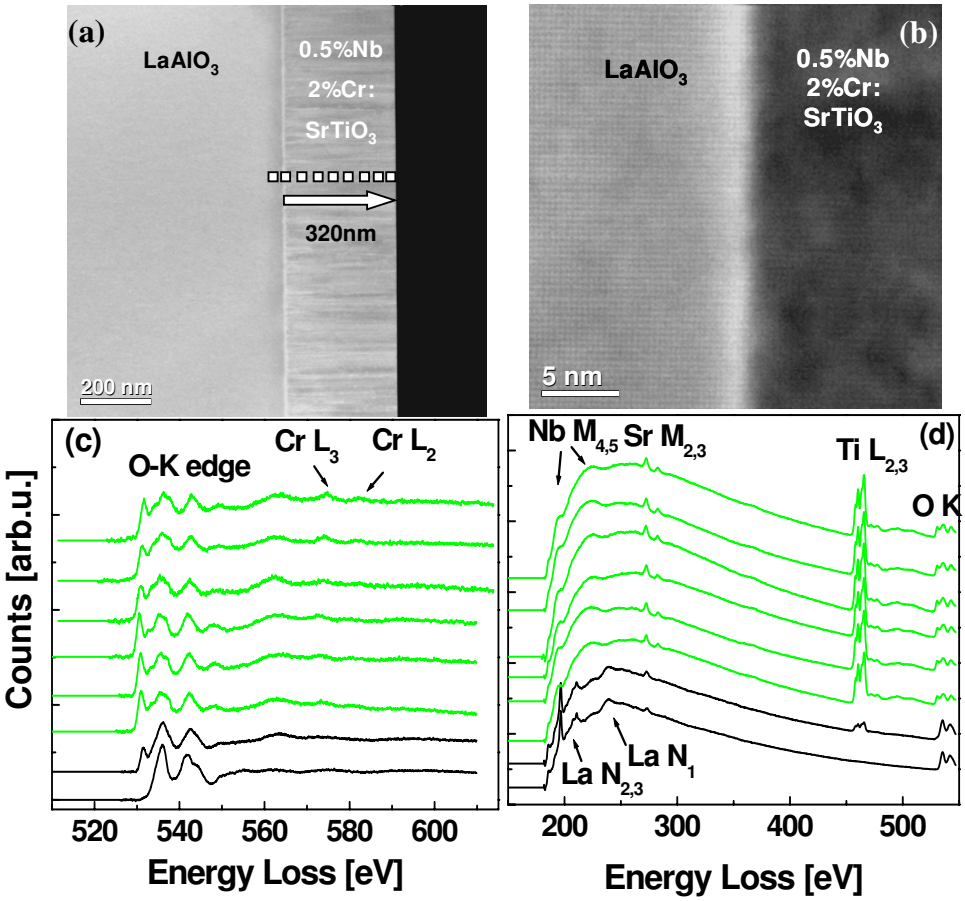

Figure 6.3: (a) Cross sectional TEM image at large length scale of the 2%Cr, 0.5%Nb doped STO film grown on $LaAlO_3$ (001) substrate. (b) High resolution TEM image for the interface between the film and substrate. (c) and (d) EELS line scans across the cross section of the sample.

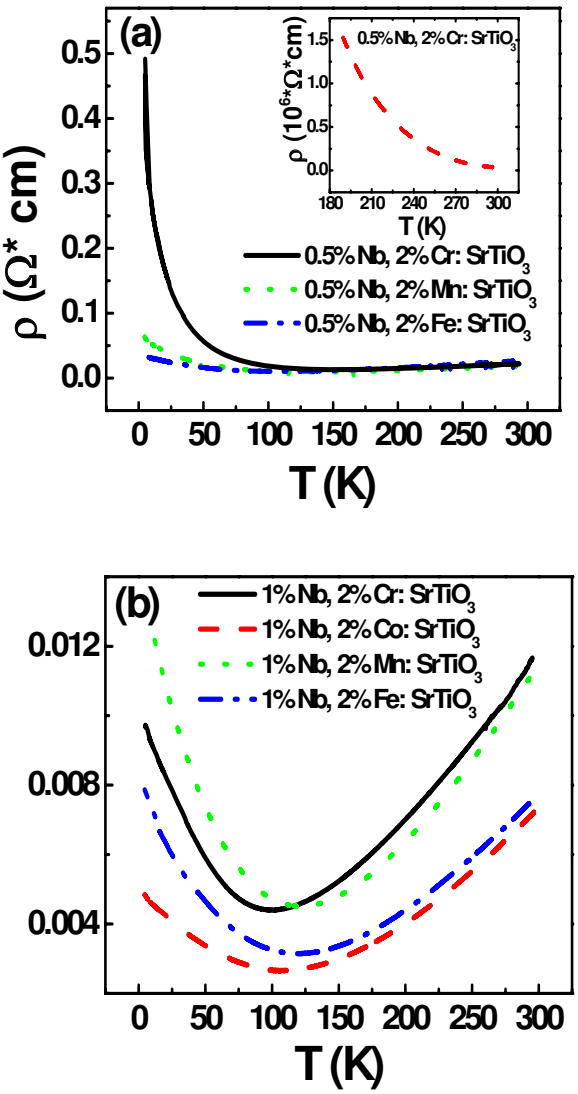

Figure 6.4: Temperature dependence of resistivity for these thin films: (a) 2%MTE, 0.5%Nb doped STO; (b)2%MTE, 1%Nb doped STO.

contribution. Fig. 6.5 (b) shows the M-H loop taken at 15 K. we have calculated the magnetic moment per cm^2 of our sample (thin film together with substrate) and compared it with the signal of a heated substrate(similarly processed, but for film deposition). Both the sample and substrate show hysteresis loops, and these loops overlap with each other. This means that the FM observed at this temperature is totally from the substrate, an extrinsic contribution. Furthermore, we measured the temperature dependence of magnetic moment over the entire temperature range of 365 K to 5 K. As shown in Fig. 6.5 (c) our sample (per cm^2) has the same magnetic moment as the substrate (per cm^2). Therefore, it is believed that no FM occurs in the magnetic transition element and niobium dual doped $SrTiO_3$ thin films.

6.2.4 Discussions

It is surprising that ferromagnetism is not observed in conductive and high quality MTE doped Nb:$SrTiO_3$ thin films, given the fact that FM is observed in a similar system (Co-(LaSr)TiO_3)[82, 102, 103, 105]. Tracking back to the origin of magnetic interaction, i.e. RKKY type of carrier mediated one, proposed in Co-LSTO system, the numbers of spins and carriers are the most important parameters for the coupling between spin and charge degrees of freedom. As introduced in chapter 4, the RKKY interaction can be written by the following formula[90, 91, 92]:

$$J = \frac{2\pi}{9} n^2 \frac{J_{sd}^2}{\varepsilon F} F(2k_F r_{ij}) \tag{6.1}$$

Where distance between spins: r_{ij} is $\sim n_s^{-1/3}$ (n_s is the density of local mo-

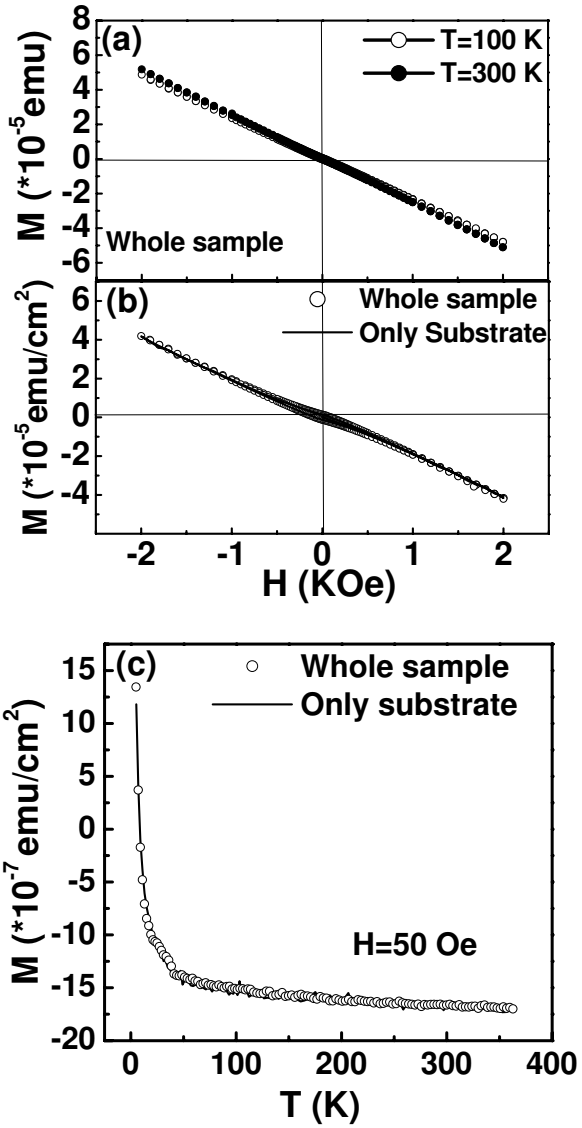

Figure 6.5: (a)Typical M vs H for one thin film(including substrate) at 300 K, 100 K; (b) Comparison of M- H for one sample with a heated pure substrate at 15 K. (substrate area unity: emu/cm^2); (c) Comparison of M-T for one sample with a heated pure substrate at an applied field of 50 Oe.

ments determined by the magnetic dopant concentration (x)). And the Fermi wave number: k_F is $\sim n_c^{-1/3}$ (n_c is the carrier density determined by donor impurity level (y)). Since the elements are fairly uniformly distributed in our samples, the Weiss mean-field treatment will lead to the ferromagnetic RKKY interaction if n_c is less than n_s, and the FM exchange strengthens with the increase of n_c up to n_s value. Since one Nb donor provides less than one electron[40], the carriers induced by Nb should be less than y×N_T, where y=0.5% or 1% in our samples and N_T is the titanium concentration in undoped STO. We also consider the carriers contributed by possible oxygen vacancies. As pointed out by Leitner et al.[40], the carriers induced by oxygen vacancies in the thin film grown at $\sim 1\times10^{-8}$ Torr and 870 ^{0}C have less than 10% contribution. So spin density given by 2%×N_T should be much higher than the carrier density. Experimentally, it is found that around 1% Nb doping even together with high oxygen reduction into STO produces less than 10^{20} cm^{-3} carriers. Given the STO lattice parameters: a=b=c=3.905 $\mathring{A}$, the titanium concentration in undoped STO is $\sim 1.6\times10^{22}$ cm^{-3} and hence the spin density of 2%×N_T= 3.2×10^{20} cm^{-3} which is several times higher than the carrier density. Thus the RKKY interaction in our samples should be ferromagnetic. It should be noted that the antiferromagnetic super-exchange (SE) interaction as a short range type, is unlikely to happen in our dilutely doped system with only 2% MTE. On the other hand, for the reported FM Co-LSTO system, the carrier density n_c is around 10^{22} cm^{-3}[82, 103], which is much higher than the spin density n_s $\sim3.2\times10^{20}$ cm^{-3}. In this case, the frustration effects in RKKY oscillation become important and should lead to the collapse of FM interaction. Therefore, the finding

of FM in Co-LSTO (assuming FM is indeed an intrinsic nature for now) and its absence of FM in our magnetic transition element doped Nb: STO may indicate that the RKKY type carrier mediated interaction is not adequate to explain the origin or absence of magnetism in these oxide based conductive systems. It is noticed that even in III-V semiconductors, RKKY is not the only mechanism for the origin of magnetic interaction[108]. Therefore, new mechanisms such as F-center model[87] or polaronic percolation theory[88, 89] etc. may need to be considered.

6.2.5 Summary

To summarize, magnetic transition element (Cr, Co, Fe, Mn) and niobium dual doped $SrTiO_3$ epitaxial films were grown by pulsed laser deposition. X-ray diffraction, Rutherford back scattering, scanning transmission electron microscopy Z-contrast imaging and electron energy loss spectroscopy together establish excellent film quality with highly orientated epitaxial growth, absence of clusters or secondary phases, and uniformity of dopant distribution. However, no evidence for occurrence of ferromagnetism is observed at the temperature range from 365 K down to 5 K though the conductivity of these films is greatly improved as a result of niobium doping effect. The absence of FM in our samples together with the observation of FM in highly conductive Co-(LaSr)TiO_3 thin films may indicate that RKKY type of carrier mediated interaction is not adequate to explain the origin of magnetism in the $SrTiO_3$ system.

Chapter 7

Magnetism and Anomalous Hall Effect (AHE) in Co-(La,Sr)TiO_3

7.1 Magnetism in Co-(La,Sr)TiO_3

The absence of FM in TM-Nb:$SrTiO_3$ thin films and the existence of FM in Co-(La,Sr)TiO_3 thin films questions the RKKY origin of ferromagnetism in $SrTiO_3$ based DMS systems, because theoretically the former system falls into an RKKY FM favorable regime while the latter falls in a frustration state. These results kindled our interest in revisiting Co-(La,Sr)TiO_3 system with a goal of understanding the origin of magnetism in this important system.

7.1.1 Sample Preparation and Structural Characterization

5%Co doped $La_{0.3}Sr_{0.7}Ti_{0.95}O_3$ thin films were grown on $LaAlO_3$(001) substrates by pulsed laser deposition at the oxygen partial pressure of 10^{-6} Torr. Such a low pressure is believed to be crucial in stabilizing the $LaSrTiO_3$ phase[109] and realizing ferromagnetism in Co-LSTO thin films[103]. The growth temperature was varied from 600 ^{0}C to 850 ^{0}C.

Fig. 7.1 (a) shows the x-ray diffraction (XRD) pattern of a typical Co-LSTO sample. Besides the substrate peaks, only the film (002) and (003) peaks were found, indicating that the film is in epitaxial LSTO (00L) phase without any impurities. The inset of Fig. 7.1 (a) shows the full width at half maximum ($\Delta\omega$) of the LSTO

(002) peak. The typical $\Delta\omega$ as low as of $\sim 0.02^0$ obtained indicates the excellent epitaxy of these samples. However, the standard XRD study is not able to bring out the micro-structure quality and exclude the existence of structurally incoherent nano-particles embeded in the system[45, 46, 85]. Therefore, a cross-section transmission electron microscopy measurement was performed on a typical sample. As seen in Fig. 7.1 (b), the orientation and density of the lattice in the enclosed area of yellow circles are different from the other regimes in the image. This indicates that the yellow circle regimes are nano-particles, which have the diameters of about $3 \sim 5$ nm and are randomly dispersed in the (La,Sr)TiO_3 matrix. The electron diffraction pattern taken in these regimes indicates that these particles are cobalt metal clusters (see Appendix 5).

7.1.2 Magnetism

7.1.2.1 Introduction to Superparamagnetism

Superparamagnetism (SPM) occurs in a system with some non-interacting ferromagnetic nano-particles dilutely dispersed in a non-magnetic matrix. When the ferromagnetic particles are small enough, they form single-domains in order to minimize the energy. Usually, the magnetization of the small single-domain FM particle is constrained to lie in one particular direction, due to various types of anisotropy, such as magneto-crystalline anisotropy, demagnetization etc. Assuming the magnetic moment M of the particle is at an angle θ to the easy axis (the direction in which the spins prefer) while the magnetic field H is applied along the easy axis,

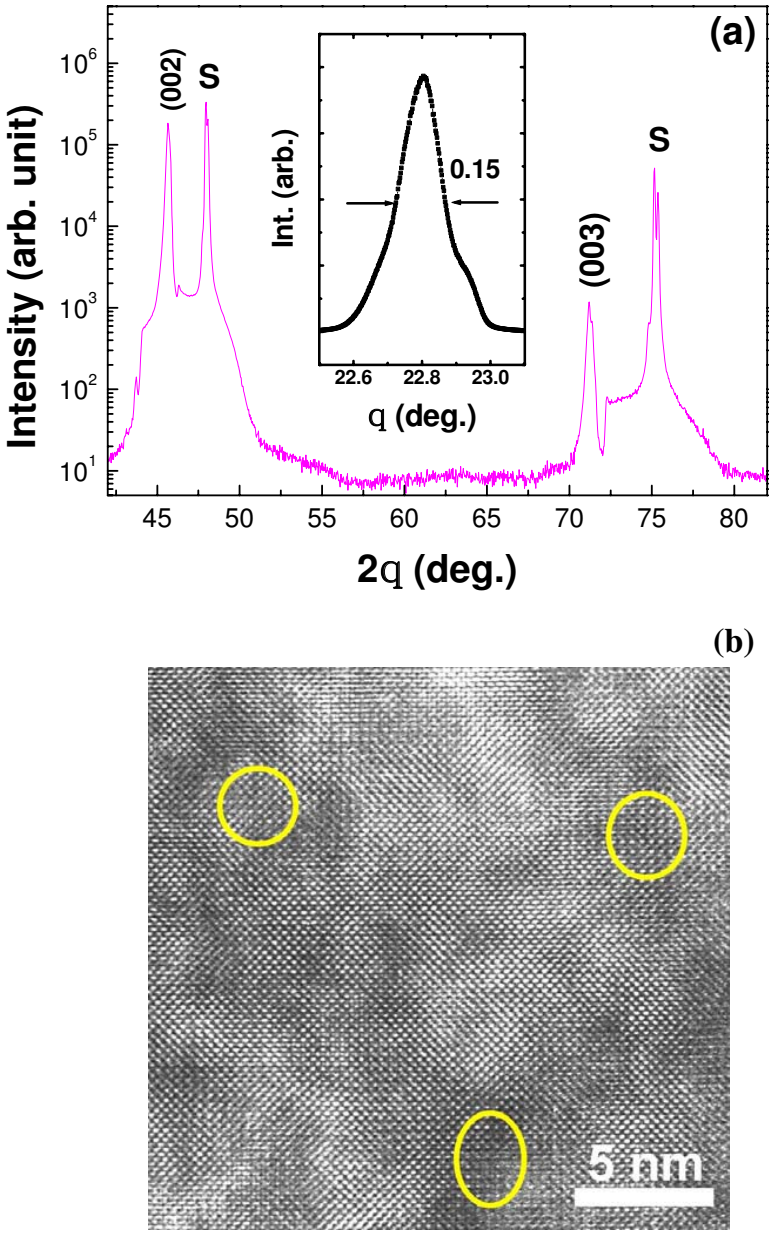

Figure 7.1: (a) X-ray diffraction pattern of a typical Co-LSTO sample. The inset shows the rocking curve for the film (002) peak; (b) A high resolution transmission electron microscopy image of the Co-LSTO sample grown at 850 ^{0}C. The yellow circles highlight the nano-clusters.

then the total energy can be written as[50]:

$$E = KV\sin^2\theta - MVH\cos\theta \tag{7.1}$$

Where K is the anisotropy constant and V is the particle volume. According to this equation, there are two minimum energies: E_{min1}=-MVH and E_{min2}=+MVH, separated by an energy barrier of E_{max}=KV[1+(HM/(2K))^2]. The probability for the particle jumping from energy minimum 1 to minimum 2 is[50]:

$$v_{12} \sim exp[-(KV/k_BT)(1 + H/H_K)^2] \tag{7.2}$$

where k_B is the Boltzmann constant, and H_K=2K/M is the anisotropic field.

The probability of the particle jumping from energy minimum 2 to minimum 1 is:

$$v_{12} \sim exp[-(KV/k_BT)(1 - H/H_K)^2] \tag{7.3}$$

Therefore,the relaxation time τ, defined as the average time it takes for one system to jump from one minimum to the other at zero field (H=0), can be written as[50]:

$$\tau^{-1} = f_0 exp(KV/k_BT) \tag{7.4}$$

where the constant f_0 is usually in the range of 10^9 $\sim$$10^{10}$s^{-1}. When k_BT is much greater than KV, the relaxation time is small, which means that the thermal energy enables the magnetic moment of the particle to fluctuate rapidly and the system behaves like a paramagnet. However, when the system is cooled down, the relaxation time increases, which means that the fluctuation slows down. Below a certain temperature, the moment of the particle fluctuates so slowly that it appears to be

blocked. This temperature is called the blocking temperature (T_B) which is usually defined as when the relaxation time $\tau \sim t_e$, where t_e is the experiment time. Then one finds[51],

$$T_B = 25KV/k_B \tag{7.5}$$

The blocking temperature can be determined experimentally by some magnetization measurements, including the temperature dependent magnetization. After an SPM system is cooled down to below T_B under a zero field, the magnetic clusters are blocked in random directions and a small external magnetic field is not able to rotate them. Upon warming under this external field, the enhanced thermal energy allows the clusters to overcome the energy barriers and start to rotate towards the field direction. Therefore the magnetization increases as the temperature increases. However, once the temperature is high enough to make the thermal energy dominate over the anisotropy energy, the clusters fluctuate so rapidly that they are not easily aligned along the field direction. As a result, the magnetization decreases as the temperature further increases, giving rise to a maximum magnetization at a certain temperature normally considered to be the blocking temperature. On the other hand, when the system is cooled down to below T_B under a non-zero magnetic field, the magnetic clusters are blocked in the direction nearly parallel to the field. The increase of temperature enhances the thermal fluctuation which leads to the decrease of magnetization along the field direction. As a consequence, the ZFC and FC M vs T curve exhibits a λ like behavior, with the FCM decreasing monotonically

upon warming while the ZFCM increases up to the blocking temperature and then decreases.

Another key feature of an SPM system is that its field dependent magnetization curve shows no hysteresis above the blocking temperature. In a SPM state, the net magnetization aligned with magnetic field can be written as[50]:

$$M_H \sim L(\mu H/K_B T) = \coth(\mu H/K_B T) - K_B T/\mu H \tag{7.6}$$

where $\mu = MV$ is the magnetization of a single cluster. According to eq. 7.6, the curves of magnetization as a function of H/T at all the temperatures above T_B should superimpose onto one curve with no hysteresis. While below the blocking temperature, the relaxation time $\tau \gg t_e$, which means that the magnetization is stable during the time of measurement, thus the system behaves like a ferromagnet. A hysteresis loop usually shows up if one measure the magnetic field dependence of magnetization below T_B.

The above discussion is based on the fact that the ferromagnetic particles do not interact with each other. The situation could be different if these particles couple with each other through types of interaction such as magnetic dipole interaction. This class of systems is called super-spin glass(SSG)[110], which is similar to the classic spin glass in a way that single atom spins are now magnetic clusters. One way to distinguish between SPM and SSG is by the measurement of memory effect proposed by Sasaki et al.[110] In this measurement, the system is cooled down to a temperature (T_w) below T_B, and after a wait at T_w, it is further cooled down

to a lower temperature. Finally, an external field is applied and the temperature dependent magnetization data are recorded upon warming. If the M vs T data obtained under this protocol (called aging protocol) is the same as the one obtained under the normal ZFC protocol, the system is recognized as superparamagnetic. However, if the MT data obtained under two protocols have different values at around T_w, normally lower magnetization values for the aging case, the system is considered as a super-spin glass. One interpretation to this result is that in an SSG, the system goes into deeper and deeper states with higher and higher energy barriers as time progresses[111, 110]. Since it is more difficult for the system blocked in a state with a higher energy barrier to respond to the field, the increase of the typical energy barrier of the state caused by an intermittent stop at T_w on cooling causes the decrease of magnetization at about this temperature. Another way to distinguish SSG from SPM is by looking at the trend of field cooled magnetization with cooling process. Normally the SPM magnetization keeps increasing by lowering the temperature, while the SSG magnetization gets saturated at low temperatures due to the correlation among clusters[110].

7.1.2.2 General Magnetic Properties

Magnetic measurements were performed on the Co-(La,Sr)TiO_3 thin films. Fig. 7. 2(a) shows the temperature dependence of zero field cooled (ZFC) and field cooled (FC) magnetization of the films grown at various temperatures(H=50 Oe, and H is perpendicular to film plane). Apparently, all of the films show a super-

paramagnetic or superspin-glass-type of behavior as we discussed in the previous section. In order to further investigate the underlying physics of the magnetic properties of this system, we performed a systematic study on a typical sample which is grown at 850 ^{0}C. As seen in Fig. 7. 2(b), the FCM and ZFCM (under a magnetic field of 150 Oe) increase with the decrease of temperature at high temperatures and depart from each other below $\sim$ 40 K, where a maximum appears for ZFCM while the FCM continues to increase with decreasing temperature. In our system, with only 5% cobalt in (La,Sr)TiO_3 host, it is reasonable to believe that the nano-clusters do not interact with each other, rendering a superparamagnetic system instead of superspin glass system, as evidenced by the non-flat FCM below the blocking temperature. To confirm this argument, we performed the studies of ZFC memory effect on our system. In this protocol, the system is zero field cooled with and without an intermittent stop at 20 K for 10000 sec and then further cooled down to 5 K, after which the magnetization data were taken upon warming at a field of 150 Oe. The temperature dependence of the difference between ZFCM with and without an intermittent stop at 20 K does not show any cusp at 20 K (inset of Fig. 7.2 (b)), indicating the absence of a memory effect, which establishes that the system is a SPM other than a SSG[110].

As introduced in section 7. 1. 2. 1, in a superparamagnetic state, the Langevin function leads the non-hysteresis M vs H/T curves to superimpose into one curve (M-H curves above 40 K in our case, Fig. 7. 3 (a)), while below $\sim$ 40 K, M vs H data show hysteresis loops and the coercivity increases with decrease in temperature (Fig. 7. 3 (b)). Here 40 K is the so-called blocking temperature (T_B), below which

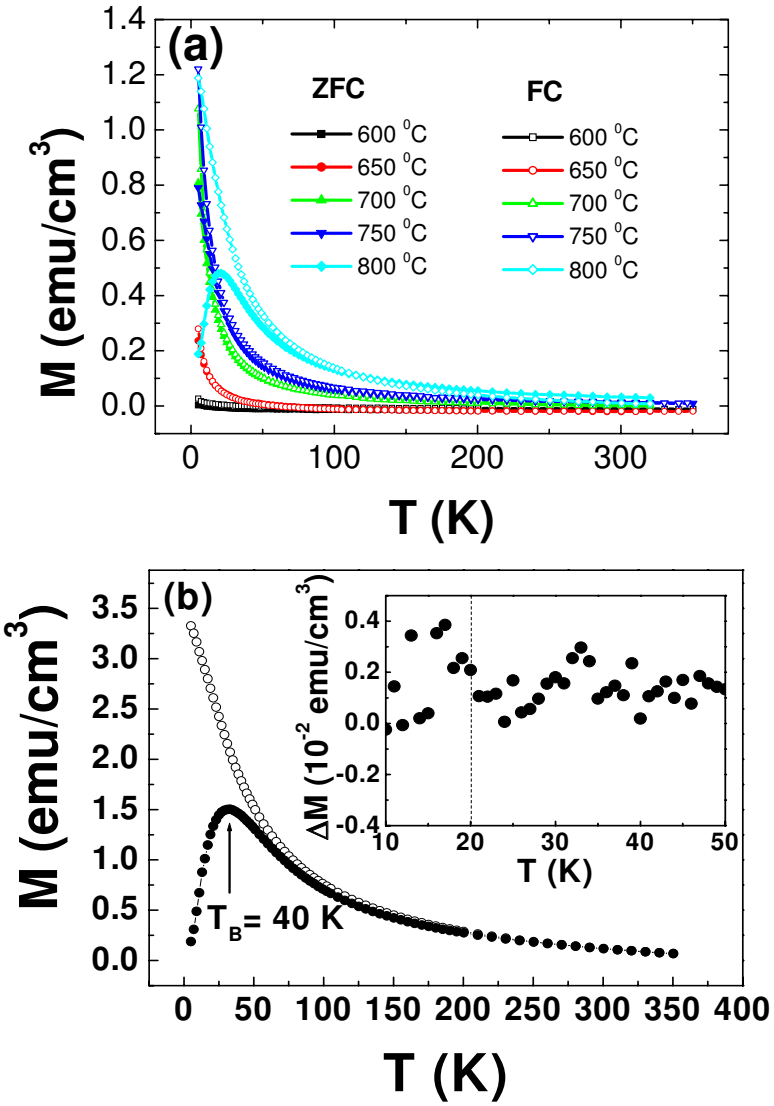

Figure 7.2: (a) zero field cooled and field cooled magnetization of Co-LSTO films (grown at 600 ^{0}C $\sim$ 800 ^{0}C) in a magnetic field of 50 Oe as a function of temperature. (b) ZFCM (solid dots) and FCM (hollow dots) of Co-LSTO film grown at 850 ^{0}C as a function of temperature. The inset shows the difference of the magnetization between normal ZFC and aging ZFC.

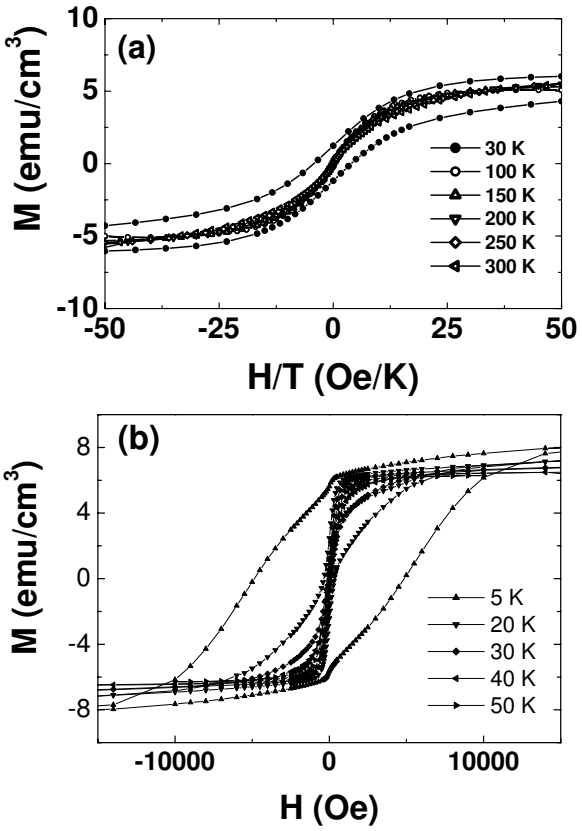

Figure 7.3: (a) M vs H/T data of the Co-LSTO film grown at 850 ^{0}C (T$\geq$ 50 K) (b) M vs H data of the Co-LSTO film grown at 850 ^{0}C (T$\leq$50 K). (c) The cross-section TEM image of the Co-LSTO film. Yellow circles indicate the nano-size clusters.

the moments of the single-domain FM particles start to be blocked due to the magnetic anisotropy. Using K=4.5106 ergs/cm^3 for cobalt, we can get the average particle volume V$\sim$ 31nm^3 (diameter D $\sim$ 3.85 nm) from eq. 7.5. As seen in the TEM image(Fig. 7.1 (a), the cobalt clusters with about 3 $\sim$ 5 nm size are indeed observed.

7.1.2.3 Discussion

After a systematic study of the magnetic properties as well as the microstructrual characterization, we found that Co-(La,Sr)TiO_3 system appears to have embedded cluster character under most experimental growth conditions examined in our work. This questions whether the system can in fact be stabilized into an intrinsic DMS state with only dilutely dispersed dopants without any degree of clustering. In the first paper reported by our group[82], based on a limited set of characterization protocols (which only evolved in later years with maturing of DMS research), this system was suggested to have an intrinsic DMS character. However, our detailed studies presented here seem to suggest an embedded cluster character for this system. The clusters are extremely fine, which are therefore likely to evade detection unless specifically probed for. We would also like to emphasize that, theoretically, the reported FM in Co-$LaSrTiO_3$ system[82, 103] falls into the regime where the carrier concentration is larger than the moment concentration, and as discussed in section 6.2.4, this will lead to the collapse of ferromagnetism if the RKKY interaction is applied[64].

7.2 Anomalous Hall Effect in Co-(La,Sr)TiO_3

7.2.1 Introduction to Anomalous Hall Effect

If an electric current (I_{xx}) flows through a conductor subjected to a magnetic field (B) perpendicular to the current, the magnetic field exerts a transverse

(Lorentz) force on the conduction electrons and holes, which tends to separate them to each side of the sample. The accumulation of charges at the sides of the conductor produces a transverse voltage (V_{xy}) which is able to balance the magnetic influence on moving charges. The presence of this measurable transverse voltage is the well-known Hall effect discovered by E. H. Hall in 1879[113]. In a non-magnetic material, the voltage has the following relation to the current and magnetic field based on the simple Drude Model:

$$V_{xy} = I_{xx} R_H B/t; or \rho_{xy} = V_{xy} t/I_{xx} = R_H B \tag{7.7}$$

where t is the thickness of the sample, ρ_{xy}= V_{xy}t/I_{xx} is called Hall resistivity and R_H is called Hall constant which equals to $\frac{1}{ne}$ in a simple one band system.

It was also found that transverse Hall voltage can be produced when an electric current flows through a ferromagnetic material in the absence of a magnetic filed. This is the so-called anomalous Hall effect or extraordinary Hall effect[114]. Generally, the Hall resistivity can be written as:

$$\rho_{xy} = R_H B + \mu_0 R_s M \tag{7.8}$$

Where, μ_0 is the permeability of free space, M is the magnetization of the material, and R_s is called the anomalous Hall constant.

The origin of the anomalous Hall effect (AHE) remains the subject of vigorous debate for many decades[115]. About 50 years ago, Karplus and Luttinger (KL) [116] investigated the band structure of ferromagnetic material by taking into account the relativistic spin-orbit interaction perturbatively. They showed that the interband matrix element of applied electric potential energy combined with the

spin-orbit perturbation gives rise to a current perpendicular to both the field and the magnetization. This theory goes beyond the semiclassical Boltzmann transport theory. For example the group velocity of an electron wave-packet is now:

$$v(k) \sim \nabla\varepsilon - eE \times \Omega \tag{7.9}$$

where, ε is the electron energy, E is the electric field, Ω is now known as the Berry curvature[117, 118, 119]. This extra term -eE×Ω is called the Luttinger anomalous velocity term, which is crucial for the AHE. As this Hall effect originates from intrinsic band structure of the material, it is commonly referred to the intrinsic anomalous Hall effect. The intrinsic anomalous Hall resistivity scales with the longitudinal resistivity as $\rho_{xy}^{AHE} \sim \rho_{xx}^{2}$[114, 115, 116]. However, this theory was criticized by Smit[120], who claimed that the impurity scattering is essential for the steady state and hence also for AHE. He pointed out that the spin-orbit scattering in a solid would give rise to asymmetric scattering of spin-up electrons (preferentially in one direction) and spin-down electrons (preferentially in the opposite direction). This spin dependent impurity scattering is called skew scattering. Due to the imbalance of spin-up and spin-down electrons in ferromagnetic materials, the skew scattering tends to induce a net Hall current which is proportional to the spin density s = n↑ -n↓, where n↑, n↓ are the spin up and spin down electron densities, respectively[121, 122]. In addition, an accompanying mechanism called side-jump scattering was proposed by Berger[123], in which the electrons in the process of being scattered also undergo a lateral displacement due to the presence of an anomalous velocity induced by the spin-orbit coupling. This induced transverse Hall current

is proportional to the spin density as well. The AHE due to skew scattering and side-jump mechanisms is collectively known as the extrinsic anomalous Hall effect as it originates from extrinsic impurities. The scaling relationship for the extrinsic AHE is $\rho_{xy}^{AHE} \sim a\rho_{xx} + b\rho_{xx}^2$[114, 120, 123].

7.2.2 The Motivation for Hall Effect Study in Co-(La,Sr)TiO_3

In diluted magnetic semiconductors, the anomalous Hall effect has played an essential role in establishing or negating the occurrence of intrinsic FM for a very long time. However, only few cases of AHE for oxide-DMS systems[76, 124, 125, 126] have been observed, mostly with reduced $TiO_{2-\delta}$ as the parent compound. Very recently, Shinde et al.[76] reported the observation of the AHE in a highly reduced cobalt doped rutile $TiO_{2-\delta}$ wherein cobalt was found to form nano-clusters. This questioned the AHE as a tool to test the intrinsic nature of DMS. Nevertheless, a systematic study of the AHE in relation to this extrinsic-DMS has been lacking because of the insulating nature of TiO_2. Moreover, it is still not clear whether the co-occurrence of AHE and superparamagnetism is unique in reduced Co-TiO_2 or not, and the AHE is continuously being considered as an evidence of intrinsic FM of DMS systems. Therefore, it is of great interest and importance to perform a systematic study of the correlation between Hall effect and magnetic properties in some other extrinsic oxide-DMS system. In this work, we chose Co-(La,Sr)TiO_3, the magnetic properties of which have already been studied in section 7.1, as the extrinsic oxide-DMS. This material was chosen not only because there has been

an increasing interest in it[82, 102, 103, 105] but also because (La, Sr)TiO_3 is a conductor[100], hence it is possible to do Hall measurements from room temperature (RT) down to very low temperatures.

7.2.3 Electronic Transport and Hall Effect in Co-(La,Sr)TiO_3 Thin Films

Figure 7. 4 (a) shows the temperature dependence of longitudinal resistivity ρ_{xx} for the 5%Co-LSTO sample grown at 850 ^{0}C. This result is identical to the un-doped (La,Sr)TiO_3 case, with a strong electron-electron scattering dominated metallic behavior[100], supporting the fact that cobalt does not incorporate into LSTO matrix. The transverse resistivity, ρ_{xy}, against magnetic field μ_0H at various temperatures is plotted in Fig.7. 4 (b) and (c). Although this system is not an intrinsic diluted magnetic system, as evidenced in section 7.1, the AHE is clearly observed over the temperature range of 5 - 300 K. The low temperature ρ_{xy} vs μ_0H curves show hysteresis, while the high temperature ones do not. According to section 7. 2. 1, the Hall resistivity is written as ρ_{xy}=R_0B +$\mu_0 R_s$M, with the first term being the ordinary Hall resistivity and the second one being the anomalous Hall resistivity. Because M gets saturated at high field and the ordinary Hall contribution dominates, the negative slope of our high field Hall data indicates the n-type carriers, which is expected for the LSTO system. we subtracted the ordinary Hall resistivity (R_0=1/ne is obtained from n $\sim$ 4$\times$ 10^{21} cm^{-3}) and plotted the anomalous Hall resistivity vs magnetic field (ρ_{xy}^{AHE} vs μ_0H) in the insets of Fig. 7. 4 (b) and (c).

For comparison, M vs μ_0H together with ρ_{xy}^{AHE} vs μ_0H for various temperatures are plotted in Figs. 7. 5(a) - (e). It can be seen that the ρ_{xy}^{AHE} vs μ_0H and M vs μ_0H curves almost coincide with each other, confirming that the AHE relates to the non-interacting magnetic clusters. The insets show the ρ_{xy}^{AHE} vs M which is almost linear. From R_S=ρ_{xy}^{AHE}/μ_0M, we can obtain the anomalous Hall coefficient $R_S \sim$ 0.03 cm^3/C (as shown in Fig. 7. 5 (f)), which has the same order as that of the normal ferromagnetic systems[127, 128].

7.2.4 The Origin of AHE in Superparamagnetic DMS

As discussed in Section 7. 2. 1, the most powerfull way to determine the origin of AHE is to study the scaling relation between ρ_{xy} and ρ_{xx}[114]. Unfortunately, in our sample, both ρ_{xx} and ρ_{xy} do not vary much with temperature, which makes it difficult to study the scaling relation. However, it would be fair to believe that the AHE observed in our sample is not the intrinsic AHE arising from band structure, since the embedded magnetic clusters do not change the band structure of the epitaxial (La,Sr)TiO_3 host which itself does not show any AHE. Spin-orbit scattering due to impurities is therefore more likely to be the underlying mechanism for our observed AHE. The magnetic clusters polarize the nearby conduction electrons as shown in Fig. 7. 6(a). Before the clusters are magnetized by the external magnetic field, the net magnetization M is zero, and therefore the spin polarization is zero. Once the cluster magnetizations get oriented by the magnetic field as shown in Fig. 7. 6 (b), a net electron spin polarization is induced (s $\sim$ M) which gives

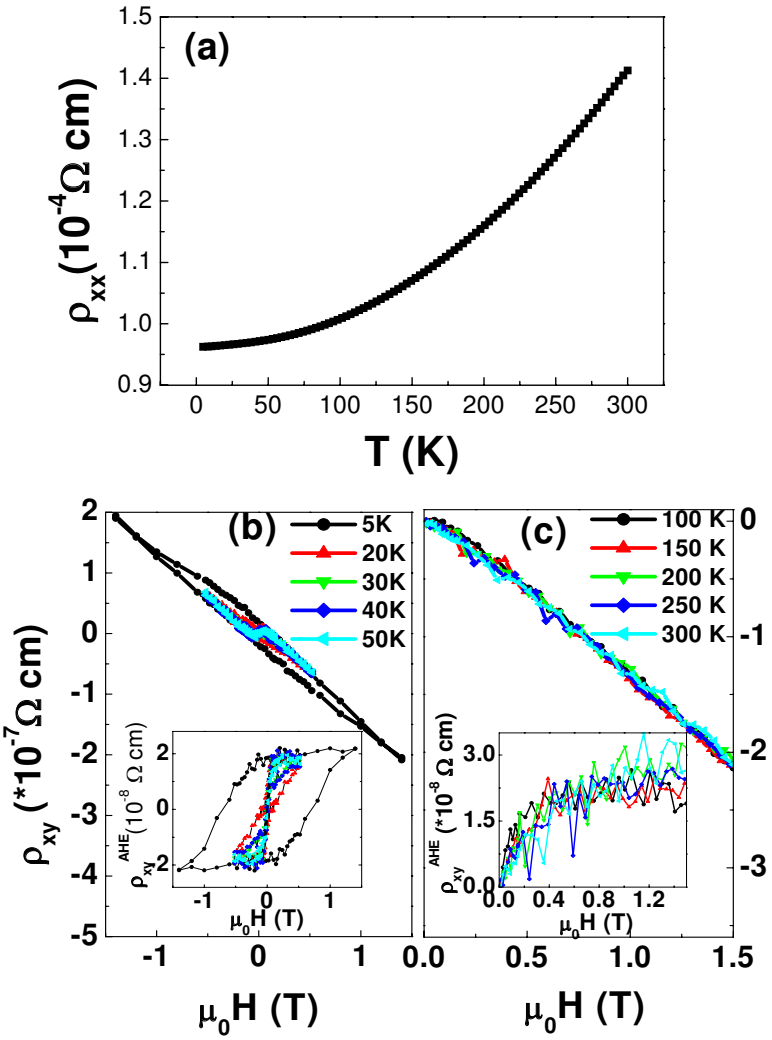

Figure 7.4: (a) The longitudinal resistivity ρ_{xx} as a function of temperature. (b)The Hall resistivity ρ_{xy} vs μ_0H at low temperatures (around and below the blocking temperature); Inset shows ρ_{xy}^{AHE} vs μ_0H (c) The Hall resistivity vs μ_0H at high temperatures (above the blocking temperature); Inset shows ρ_{xy}^{AHE} vs μ_0H. The film was grown at 850 ^{0}C

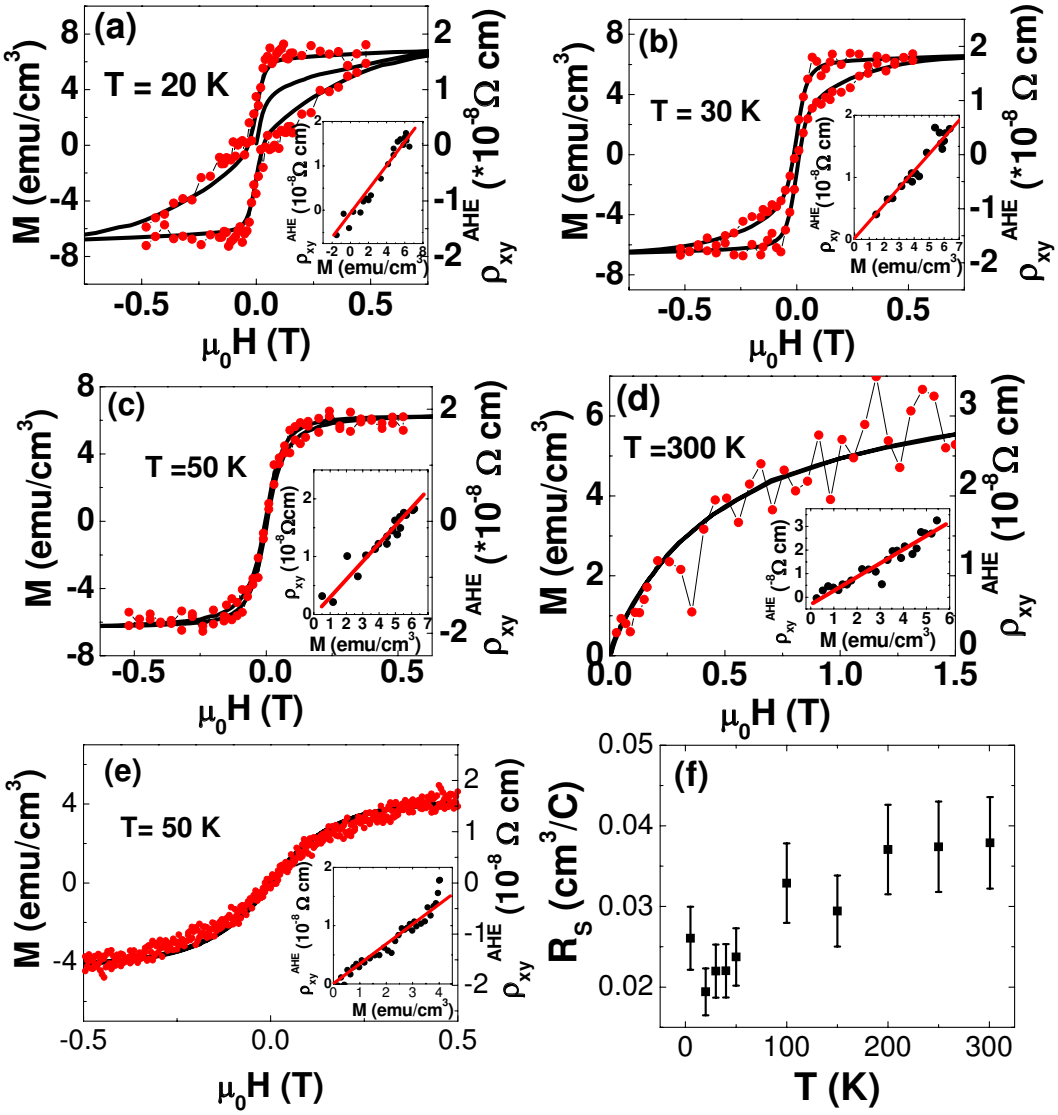

Figure 7.5: (The comparison of the magnetic field dependence of anomalous Hall resistivity ρ_{xy}^{AHE} (red(dark gray) dots with right axis) and magnetization M (solid black line with left axis) at (a) 20 K, (b) 30 K, (c) 50 K, (d) 300K, for the film grown at 850 ^{0}C. e) 50K for the film grown at 750 ^{0}C (just to show the same behavior is observed in films grown at other temperatures). Insets show ρ_{xy}^{AHE} vs M for the respective temperatures(black dots are experimental data, solid red(dark gray)lines are fitting data); (f) R_s as a function of temperature for the sample grown at 850 ^{0}C.

rise to a non-zero transverse Hall current due to the extrinsic spin-orbit scattering. This picture is substantiated by the fact that the observed ρ_{xy}^{AHE} vs μ_0H curve is almost identical to the M vs μ_0H curve and therefore ρ_{xy}^{AHE} is proportional to the magnetization M (as seen in insets of Figs. 7. 5 (a)-(e)), which is the case for the extrinsic AHE. We note that for the case of intrinsic AHE, except for the known particular case of ferromagnetic Mn_5Ge_3 thin film[129], the ρ_{xy}^{AHE} vs M profile is in general rather nonlinear[119, 130].

7.2.5 A New Parameter to Test Intrinsic DMS by AHE

We note that the magnitude of the AHE (here defined by $\rho_{xy}^{AHE}/\rho_{xx}$) found in the extrinsic DMS is usually very small compared to that found in intrinsic DMS. For example, with similar doping level, $\rho_{xy}^{AHE}/\rho_{xx}$ in our Co-LSTO here and highly reduced Co-$TiO_{2-\delta}$ has values of the order of 10^{-4}[76, 126], while in the intrinsic DMS with long range FM order, i.e. (Ga, Mn)As, $\rho_{xy}^{AHE}/\rho_{xx}$ is $\sim 10^{-2}$[70, 131, 132, 133]. This is not surprising if one notes that $\rho_{xy}^{AHE}/\rho_{xx}$ is proportional to the spin polarization (s/n)[134]. In our extrinsic DMS, the magnetic clusters do not couple to each other (superparamagnetism), but only polarize the carriers in the nearby region depending on the interaction strength. However, in intrinsic DMS, especially for the carrier mediated type, the carriers strongly couple to the local magnetic ions which are more homogenously distributed. Therefore, the population of carriers contributing to AHE in the intrinsic DMS is much larger than in the extrinsic case, which hence gives rise to a higher magnitude of AHE. Moreover, it

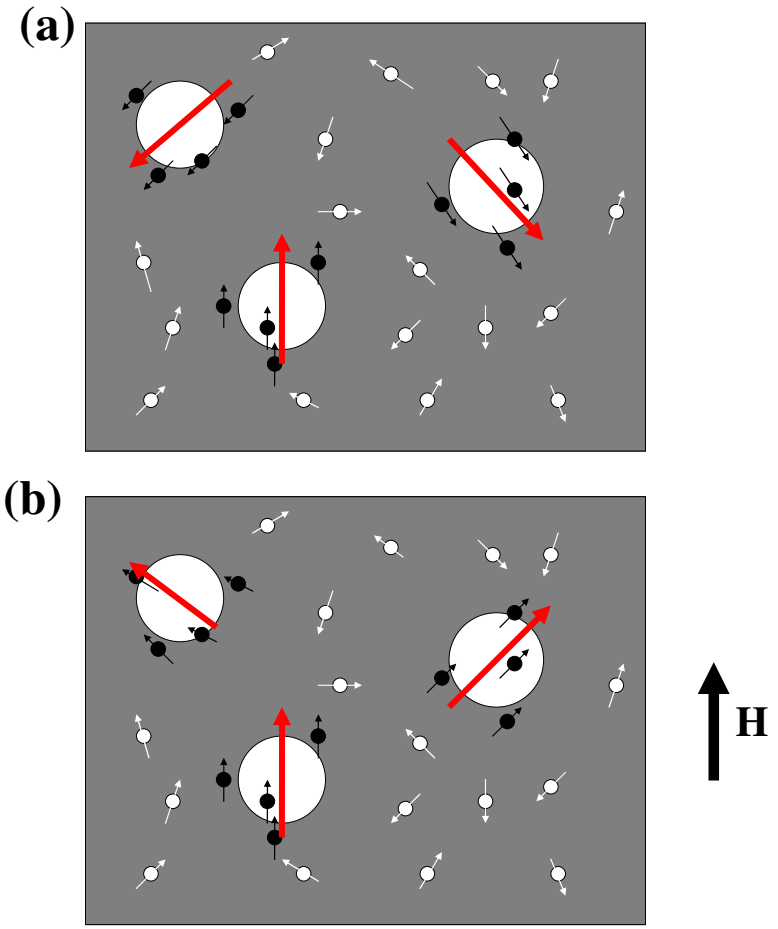

Figure 7.6: Schematic pictures of magnetic clusters and electrons inside a SPM sample as in our experiment (a) before and (b) during the cluster spins are oriented by the magnetic field H: the big white circles are clusters; the small black circles are electrons polarized by the clusters; The small white circles are electrons not polarized by the clusters. Arrow crossing each circle indicates the spin orientation of each object.

has been found that the Berry-phase contribution of the AHE in the intrinsic DMS is more significant than the scattering contribution[119, 129, 130]. Therefore, we claim that the magnitude of AHE ($\rho_{xy}^{AHE}/\rho_{xx}$) can be used as a criterion for intrinsic or extrinsic diluted magnetic semiconductors.

7.3 Summary

In summary, a systematic study of the magnetic properties and the Hall effect was performed on pulsed laser deposited 5 % cobalt doped (La, Sr)TiO_3 thin films, especially grown at high substrate temperature. The system is found to be super-paramagnetic in nature as evidenced by several protocols of magnetic measurements. Nevertheless, the anomalous Hall effect (AHE) is observed in the system, the profile of the measured Hall resistivity vs magnetic field being found to be identical to the magnetic hysterisis loops. This highlights the limitations of AHE as a tool to test the intrinsic nature of ferromagnetism in a diluted magnetic system, supporting the previous report for the Co: $TiO_{2-\delta}$ case[76]. It is believed that the magnetic clusters polarize nearby electrons and the non-zero polarization leads to a net transverse current because of the spin dependent scattering, which gives rise to the observed AHE. We point out that the AHE signal observed in the current extrinsic DMS is much weaker than that observed in the intrinsic long range ferromagnetic ordered DMS due to the reduced population of spin-polarized carriers, which raises the possibility for using this magnitude, rather than the occurrence of AHE, as a criterion for intrinsic or extrinsic DMS.

Chapter 8

Magnetic Effect in Anatase Nb: TiO_2 Thin Films

In chapter 2 and 3, we have shown that epitaxial anatase Nb: TiO_2, grown at a low oxygen partial pressure (10^{-5}) by pulsed laser deposition, is an intrinsic transparent conducting oxide (TCO). I will show, in this chapter, that the low temperature conductivity of Nb:TiO_2 grown at a higher pressure is dominated by spin scattering, which indicates the existence of magnetism in this transparent material.

8.1 Introduction

To understand the underlying physics of the low temperature conductivity of Nb:TiO_2, I would like to introduce two different mechanisms, namely the Kondo effect and the weak localization effect, Both of which are usually important at low temperatures and give rise to similar temperature dependent resistivity behaviour. The approach to distinguish between these two will also be discussed.

8.1.1 Orbit Scattering - Weak Localization Effects

In semi-classical limit ($k_F l \gg 1$, where l is the mean free path of carriers, and k_F is the Fermi wave vector), the Boltzmann approach successfully describe the transport properties of normal metals. This theory studies the evolution of the distribution of particles subjected to various fields and gradients, rather than

describing each particle individually. The generalized Boltzmann equation is[3, 135]:

$$\dot{f}_{scattering,\vec{k},\vec{r}} = \vec{v}_{\vec{k}} \cdot \frac{\partial}{\partial \vec{r}} f_{\vec{k},\vec{r}} + \frac{e}{\hbar}(\vec{E} + \vec{v}_{\vec{k}} \times \vec{B}) \cdot \frac{\partial}{\partial \vec{k}} f_{\vec{k},\vec{r}} \tag{8.1}$$

Where, f is the distribution function, $\vec{k}$ is the wave vector, $\vec{r}$ is particle position, $\vec{E}$ and $\vec{B}$ are electric field and magnetic field respectively. One can calculate the electrical conductivity of the system by solving the above equation. The conductivity of a metal can be written as[3, 135]:

$$\sigma_{ij} \equiv \frac{J_i}{E_j} = -e^2 \int \frac{\upsilon_i \upsilon_j \tau d\vec{k}}{4\pi^3} \frac{\partial f}{\partial \varepsilon} \tag{8.2}$$

Where υ is the group velocity of an electron wave packet, ε is the energy and τ is the relaxation time.

The temperature dependence of resistivity ($\rho \equiv \frac{1}{\sigma}$) due to fundamental scattering processes are summarized as following[3, 135]:

1)Elastic impurity scattering: ρ_i=ρ_0, where ρ_0, independent of temperature, is called residual resistivity;

2)Electron-phonon scattering:

$$\rho_{e-p} = \frac{A}{\Theta_D}(\frac{T}{\Theta_D})^5 \int_0^{\frac{\Theta_D}{T}} \frac{x^5 dx}{(e^x - 1)(1 - e^{-x})} \tag{8.3}$$

or

$$\rho_{e-p} \sim \frac{T}{\Theta_D}, (T \gg \Theta_D) \tag{8.4}$$

$$\rho_{e-p} \sim (\frac{T}{\Theta_D})^5, (T \leq \frac{\Theta_D}{50}) \tag{8.5}$$

where A is a temperature (T) independent constant, Θ_D is the Debye temperature.

3) Electron-electron scattering:

$$\rho_{e-e} \sim T^2 \tag{8.6}$$

According to the Matthiessen's rule that the total scattering rate is a sum of the rates from all the different processes, or

$$\frac{1}{\tau} = \Sigma \frac{1}{\tau_i} \tag{8.7}$$

Therefore, the temperature dependence of total resistivity caused by impurity scattering, electron-phone scattering and electron-electron scattering is:

$$\rho = \rho_0 + \alpha T^2 + \beta T^5 \tag{8.8}$$

here T $\ll \Theta_D$ is assumed, which is true in the temperature regime of our measurements.

The enhancement of disorders in "dirty" metals decreases the mean free path of electrons. If $k_F l \ll 1$, a quantum-mechanical treatment must be applied as the above semi-classical approach is not valid anymore. A quantum effect known as weak localization effect (WLE)[136, 137], originated from the constructive interference of the electron wavefunctions, occurs in the case of weak disorder limit. A temperature dependent quantum correction term to the Boltzmann conductivity is applicable in this limit.

The physical mechanism of weak localization caused by disorder is the phase coherence induced back-scattering. Fig. 8. 1 shows an array of scatterers which scatter electrons isotropically. An electron wave function is scattered off the first

scatterer it encounters, and the scattered wave gets scattered again by the second scatterer, leading to the second order scattered wave and so on. The total wave function of these processes is the sum of all of the multi-scattered waves. If two random waves labled 1 and 2 are chosen as seen in Fig. 8. 1 (a), then the total wave function is just the incoherent sum of these two individual waves (the total amplitude $\mid A_0 \mid = \sqrt{\mid A_1 \mid^2 + \mid A_2 \mid^2}$). Now we choose two special waves as shown in Fig. 8. 1 (b). They travel around the same closed loop in opposite directions: wave 1 (denoted by black line) traverses the loop in clockwise direction, while wave 2 (denoted by red line) traverses the loop in anticlockwise direction. The beginning of the path of wave 1 corresponds to the end of the path of wave 2 and vice-versa. We call these two partial electron waves "complementary" because they have the same amplitude A and phase ϕ when they return to their initial points. And at the initial point, these two complementary waves interfere, leading to their combined return probability of $|2A|^2=4|A|^2$. As discussed previously, for two uncorrelated electron waves, the probability has only the value of $2|A|^2$ if the individual wave has the same amplitude of $|A|$. Therefore we have an additional "coherent back scattering" probability of $2|A|^2$. This increased probability will apprarently decrease the transmission of electron waves and hence the conductivity of a sample.

It should be noted that the inelastic scattering, which can change the energy of electrons, must be avoided in order to maintain the wave coherence. In other words, the inelastic mean free path should be large enough to observe significant WLE. This is why this effect is always observed at low temperatures where the electron-phonon, electron-electron interactions are negligible.

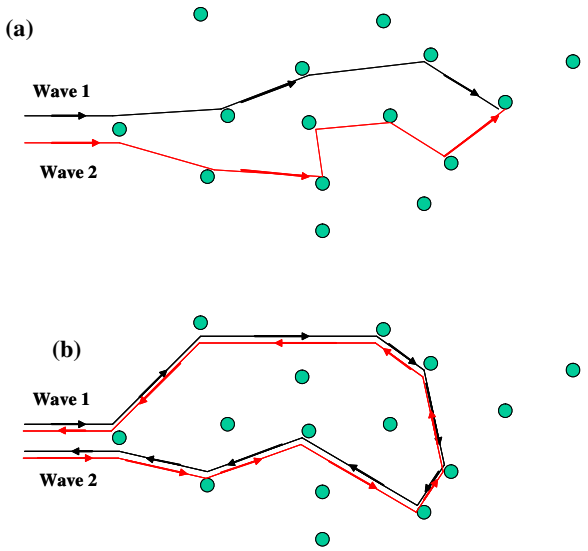

Figure 8.1: A schematic picture shows that the electron waves are scattered by the impurity scatterers (a) two random electron waves; (b) two complementary electron waves

Theoritical work have shown that any amount of disorder, no matter how small, causes localization in a 1-D or 2-D sample at zero temperature. While in a 3-D sample, only a large amount of disorder can cause localization effect, but a small amount can not. Theoritical calculation also shows that the quantum correction to conductivity due to WLE for 2-D and 3-D sample has different temperature dependence[136]:

1)

$$\Delta\sigma(T) = \frac{p}{2}\frac{e^2}{\hbar\pi^2}\ln(\frac{T}{T_0}) \tag{8.9}$$

for 2-D;

2)

$$\Delta\sigma(T) = \frac{e^2}{\hbar\pi^3}\frac{1}{l_{in}} = \frac{e^2}{\hbar\pi^3}\frac{1}{a}T^{p/2} \tag{8.10}$$

for 3-D.

where $l_{in} = aT^{-p/2}$ is the inelastic mean free path and p is a constant depending on scattering mechanism.

The presence of magnetic field can destroy the coherence of carrier wave functions and hence depress the weak localization effect. Theoritical calculation predicts the following magnetic field dependence of magnetoresistance for 2-D and 3-D systems[136]:

1)

$$\Delta\sigma(H,T) \equiv \sigma(H,T) - \sigma(0,T) = \frac{e^2}{2\hbar\pi^2}\{\Psi(\frac{1}{2} + \frac{1}{l_{in}^2 4eH/\hbar c}) + ln(l_{in}^2 4eH/\hbar c)\} \quad (8.11)$$

for 2-D. At high fields, the digamma function $\Psi(\frac{1}{2} + \frac{1}{l_{in}^2 4eH/\hbar c})$ is a constant, so $\Delta\sigma(H,T) \sim \ln(H)$

2)

$$\Delta\sigma(H,T) \equiv \sigma(H,T) - \sigma(0,T) = (\frac{eH}{\hbar})^{\frac{1}{2}} f(\frac{\hbar c}{4eHl_{in}^2}), \quad (8.12)$$

for 3-D. At high fields, $f(\frac{\hbar c}{4eHl_{in}^2})$ is a constant, therefore $\Delta\sigma(H,T) \sim H^{\frac{1}{2}}$.

In general, the magnetoresistance (MR) of a 3-D system is isotropic, while the same of a 2-D system is anisotropic(MR is only observed when magnetic field has perpendicular component). In the next section, I introduce a spin scattering effect which can also modify the low temperature conductivity of a metal through impurities.

8.1.2 Spin Scattering - Kondo Effect

It was discovered in 1930s, that when adding a small amount of magnetic impurities (i.e. Mn, Fe etc.) into pure metals (i.e. Cu, Ag etc.), a resistivity minimum appears at low temperatures and below this minimum the reistivity shows a logarithmic increase as the temperature is lowered further[138]. The increment of the resistivity below the resistivity minimum temperature is almost proportional to the concentration of magnetic impurities, which suggests that this effect is an isolated impurity phenomenon[139].

It was proposed by Kondo in 1964[138], that there exists an interaction, called s-d exchange interaction, between the magnetic impurities and the nearby conduction electrons(this interaction has been mentioned in section 4. 2. 3. 1). The s-d exchange Hamiltonian is written as:

$$H_{sd} = -2J_{sd}(\vec{s}\vec{S}) \tag{8.13}$$

Where $\vec{s}$ is the spin of conduction electron and $\vec{S}$ is the spin of magnetic impurity. J_{sd} is the exchange interaction between $\vec{s}$ and $\vec{S}$. Kondo[138] treated the s-d interaction as a perturbation and calculated the scattering probability of the conduction electron up to the third-order. He found that the resistivity caused by the s-d interaction was given by[138]:

$$\rho_k = c(n_{\varepsilon_F})^2 J_{sd}^2 S(S+1)[1 + 4J_{sd}n_{\varepsilon_F} \log \frac{k_B T}{D}] \tag{8.14}$$

Where c is a constant propotional to the impurity concentration, and n_{ε_F} is the density of states at ε_F in a flat band of width 2D[93, 139].

Kondo's theory correctly describes the observed upturn of the resistivity at low temperatures. However, it also gives the wrong prediction that the resistance diverges at zero temperature. It turns out that the perturbation theory is not applicable below a certain temperature called Kondo temperature (T_k), which is defined as[93, 139]:

$$T_K = \frac{D}{k_B} \exp(-\frac{1}{Jn_{\varepsilon_F}}) \tag{8.15}$$

In 1974, Kenneth Wilson[140, 141, 142] at Cornell University developed a method known as 'numerical renormalization' and proved that at temperatures well below T_k, the localized magnetic moment is screened by the spins of the conduction electrons and the system gradually reaches the singlet state at 0 K. Therefore the resistivity starts to saturate below T_k

When a magnetic field is applied to a Kondo system, the Kondo scattering is being depressed due to the alignment of spins and thereby it gives rise to a negative magnetoresistance. since the Kondo scattering is a spin scattering process, the magnetoresistance should be independent on the direction of applied magnetic field[139].

In summary, the upturn of resistivity at low temperatures is due to the antiferromagnetic s-d exchange interaction between the conduction electron and the localized moment(as shown in Fig. 8. 2). Below T_k, the localized moment gets screened by conduction electrons and a singlet state is formed gradually.

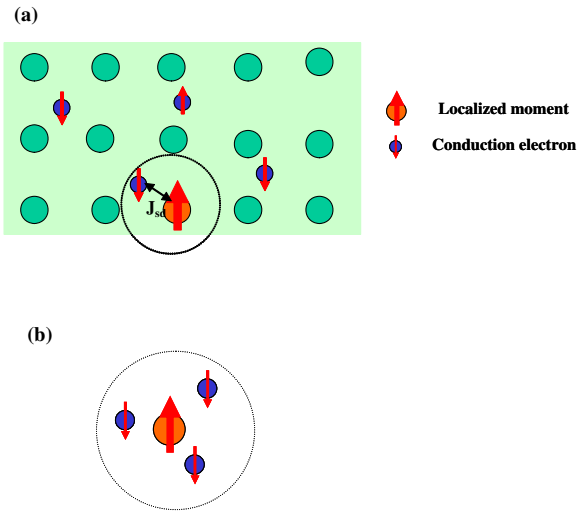

Figure 8.2: (a) The s-d exchange interaction in a Kondo system (b) the screen of localized moment by conduction electrons.

8.2 Experimental Results and Discussions

The transparent metallic anatase $Ti_{1-x}Nb_xO_{2-\delta}$ films studied in chapter 2 is grown at 10^{-5} Torr. In this chapter, we will discuss the magnetic effects observed in the films grown at a higher oxygen partial pressure of 10^{-4} Torr. The deposition temperature is 850 ^{0}C. The concentrations of niobium are x= 0.00, 0.01, 0.03, 0.05, and 0.07.

8.2.1 Conductivities and Hall Coefficients

The undoped TiO_2 thin film grown at 10^{-4} is highly insulating and the resistance is out of the range of measurement. Fig. 8. 3 (a) shows the temperature (T) dependence of resistivity of $Ti_{1-x}Nb_xO_2$ thin films with different dopant concentrations (x=0.01, 0.03, 0.05, and 0.07). All the doped samples studied in this work

show metallic behavior at high temperatures, however the resistivity of all these samples show an upturn below a certain temperature with a lnT behavior. Fig. 8. 3 (b) shows the Hall constant (R_H) as a function of temperature. The R_H is negative indicating that the carriers are mainly electrons, and the absolute value of R_H decreases as the dopant concentration increases which suggests increase in the conduction electron concentration. Moreover, R_H is almost independent of temperature, implying that the change of resistivity with temperature should arise from the temperature dependent scattering. Therefore, the low temperature lnT dependent resistivity is an indication of the Kondo effect, due to enhanced spin scattering[139] with lowering of temperature, or 2-D weak localization[137], due to self-interference of wave packets when they are backscattered coherently by impurities.

As disccussed in section 8.1.1, the 2-D weak localization effect gives rise to anisotropic negative magnetoresistance while the Kondo effect leads to isotropic negative MR. Therefore, we performed magneto-resistance measurements in order to resolve the underlying mechanism of the lnT dependent resistivity of these thin films. Fig. 8. 4 (a) shows the MR of $Ti_{0.95}Nb_{0.05}O_2$ film as a function of the magnetic field, where MR is defined as $\frac{\rho(H)-\rho(0)}{\rho(0)}$. The magnetic field is either perpendicular to the film plane (hence perpendicular to the current I) or parallel to the current. Negative MR was observed at temperatures below the resistivity minimum and becomes prominent with decreasing temperature. The negative MR saturates more easily with field at lower temperature than it does at higher temperature. The 2 K negative MR saturates at about 3 T and a positive MR contribution is observed at higher fields. The origin of this positive MR is still not clear. Comparing the

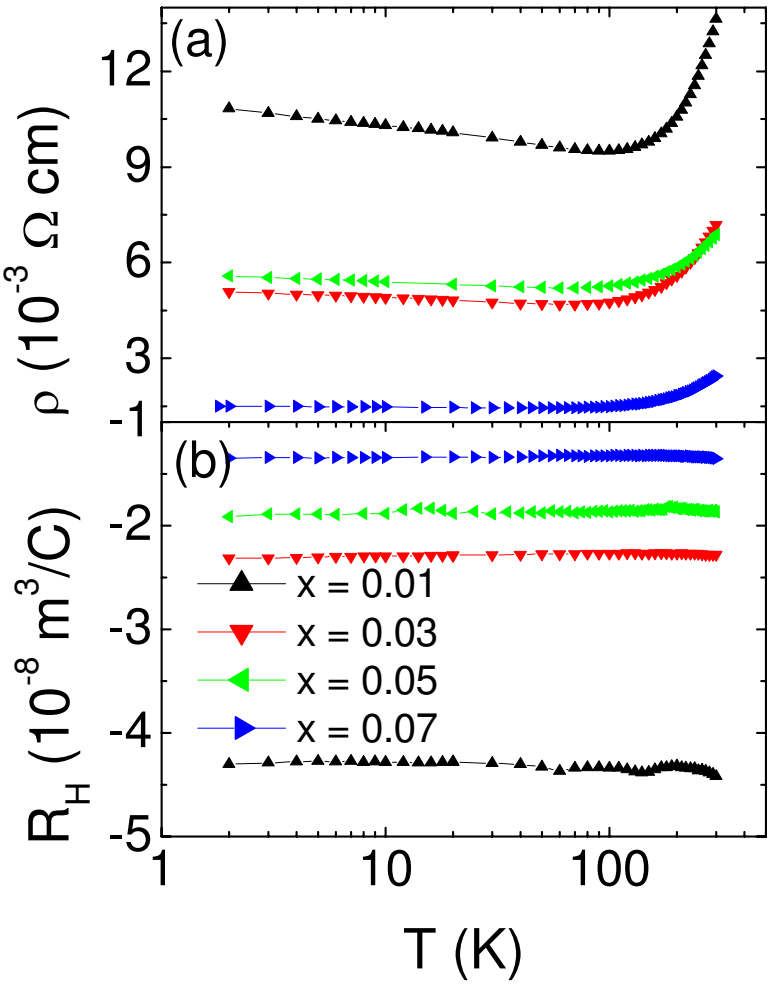

Figure 8.3: Temperature dependence of (a) resistivity and (b) Hall constant of $Ti_{1-x}Nb_xO_2$ thin films (x = 0.01, 0.03, 0.05, 0.07)

MR at two different field directions, it is clear that the MR is almost isotropic, suggesting that the lnT dependence of resistivity and negative magnetoresistance are mainly due to spin effect[138, 139] (Kondo effect) other than orbit effect[137] (2-D weak localization). To further confirm this, we did the angular (θ) dependence of MR measurements under various fields at 2 K, where θ=0 corresponds to the field perpendicular to the film plane. As shown in Fig. 8. 4 (b), the angular dependence of MR is very small. Assuming the magnetoresistance is due to both the spin scattering and orbital related effect, the MR data can be fitted by a simple expression MR=MR_1+MR_1| cos(θ) |, where MR_1 and MR_2 are due to the spin effect and orbital effect, respectively. As seen in Fig. 8. 4 (b), the data can be fitted well by this formula. And as shown in the inset of Fig. 8. 4 (c), the ratio of MR_1/MR_2 is about 0.15, suggesting that the dominant effect is spin-related.

Now I would like to focus on the typical $Ti_{0.95}Nb_{0.05}O_2$ sample with more qualitative analysis on the resistivity data. We measured the resistivity of this sample down to 0.4 K using a He-3 system. Any heating effect has been ruled out. As seen in the inset of Fig. 8. 5 (a), the resistivity tends to deviate from the lnT dependence at below 1.5 K, which is expected for the spin scattering picture but not for the 2-D weak localization. As briefly disccussed in section 8. 1. 2, in the spin scattering case, lowering of temperature below the Kondo temperature, the localized magnetic moment is gradually cancelled out by the nearby anti-parallel spins of the conduction electrons, by the formation of singlet states. Therefore, the scattering of the conduction electrons by the local magnetic moments is weakened, and the resistivity starts to saaturates. The total resistivity including the contributions

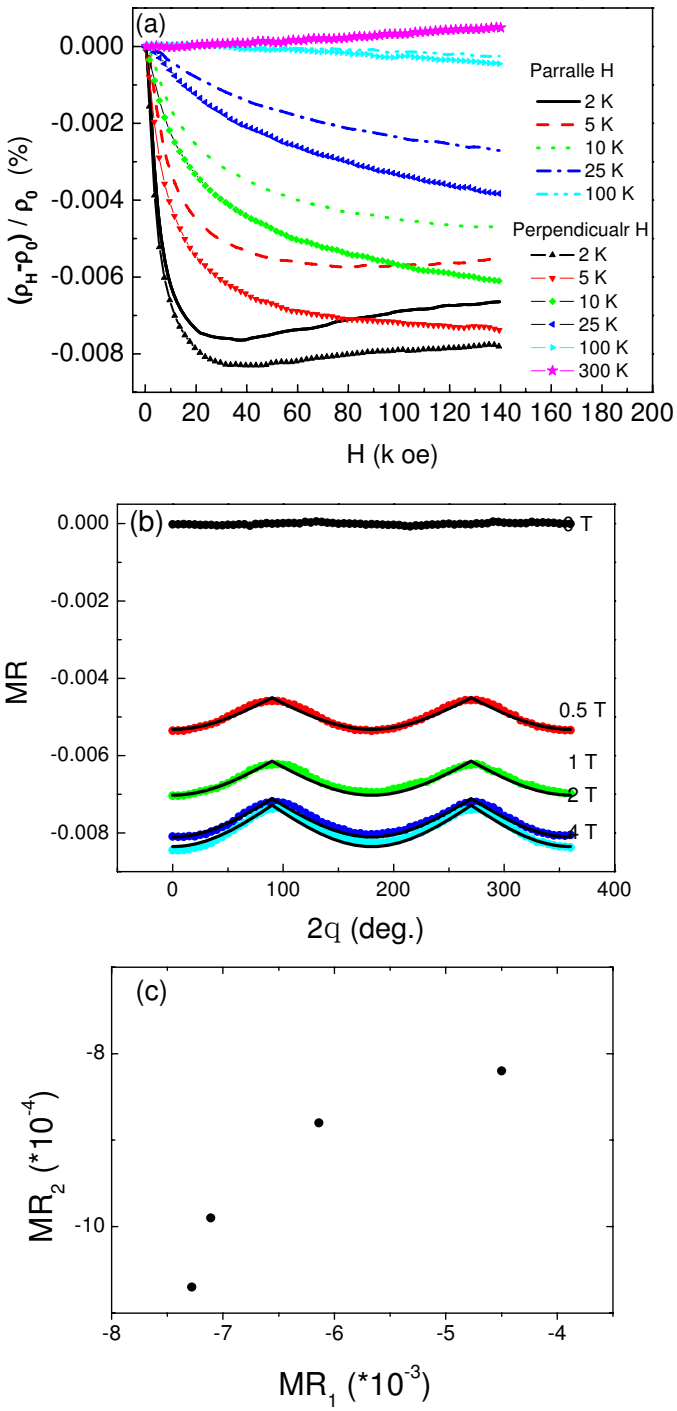

Figure 8.4: (a) Magnetoresistance of $Ti_{0.95}Nb_{0.05}O_2$ thin film at various temperatures with magnetic field perpendicular to film plane or parallel to electric current; (b) Angular dependence of magnetoresistance of $Ti_{0.95}Nb_{0.05}O_2$ thin film; (c) MR_2 versus MR_1

from elastic impurity scattering, electron-phonon (e-p) scattering, electron-electron (e-e) scattering and Kondo scattering is written as:

$$\rho_{total} = \rho_0 + \rho_{e-p} + \rho_{e-e} + \rho_k \tag{8.16}$$

Where ρ_0 is the residual resistivity due to impurity scattering, $\rho_{e-p} = \alpha T^2$ is from e-p scattering, $\rho_{e-e} = \beta T^5$ is from e-e scattering, ρ_k is the Kondo resistivity. Since the Kondo resistivity is negligible at high temperatures, we fitted the resistivity data at temperatures above T_{min} by only considering the contributions of impurity scattering, e-p scattering and e-e scattering. As seen in Fig. 8. 5 (a), the fit is very good. The parameters obtained from the fit are: ρ_0=0.00505 Ωcm, α=2.0314$\times 10^{-8}$ $\Omega cm T^{-2}$, and β=5.2605$\times 10^{-19}$ $\Omega cm T^{-5}$.

Fig. 8. 5 (b) shows the low temperature Kondo resistivity, which is obtained by subtracting the other contributions from the total resistivity. In a typical Kondo system, the following empirical formula is usually employed to fit the low temperature ρ_k at zero field[143]:

$$\rho_k(T,0) = \frac{\rho_u}{2}[1 - \frac{\ln[(T^2+\theta^2)/T_k^2]}{\pi[S(S+1)]^2}] \tag{8.17}$$

where ρ_u is the unitarity-limit resistivity, S represents the spin of local moment correlating with conduction electrons, and $\ln(\theta/T_k)$ = -$\pi[S(S+1)]^{1/2}$. As seen in Fig. 8. 5 (b), the Kondo resistivity data can be fitted by the above formula well at low temperatures with the parameters of: S=1/2, $\rho_u \sim 0.0007 \Omega cm$ and $T_k \sim$8.85 K. Although the fitting looks quite good, the difference ($\Delta\rho$) between the subtracted Kondo resistivity and the fitting data shows a period dependence of temperature (Fig. 8.5 (c)). One possible reason for this is that we used very simple equations in

the electron-electron scattering (T^2) and electron-phonon scattering (T^5) process. However, the T^2 relation in electron-electron scattering and the T^5 in electron-phonon scattering are only valid in a limited temperature range. The deviation of these simple equations may give rise to the period background of $\Delta\rho$.

8.2.2 Possible Origin of magnetic moments

In this section, I would like to discuss the possible origin of local magnetic moments required for the Kondo effect in niobium doped TiO_2 samples. As shown by the RBS data in Chapter 3, almost all of niobium atoms substitute in titanium site, though disorder is created in TiO_2 matrix. As shown in Fig. 3. 4 (a), the binding energies of Nb $3d^{3/2}$ and Nb $3d^{5/2}$ are 210.2 eV and 207.7 eV, respectively, which indicates that niobium is in +5 state other than +4 state[48]. The binding energies of Ti $2p^{1/2}$ and 2 $p^{3/2}$ are 465.1 eV and 459.5 eV(Fig. 3. 4(b)), respectively, suggesting that titanium is in +4 state[49]. Therefore, it is unlikely that the local moments responsible for Kondo scattering emerge from the cations. Another possibility is that specific native defect types could lead to magnetic moments. Indeed, Coey et al.[85] have proposed that oxygen vacancy induced in conventional non-magnetic oxide semiconductors could, under certain circumstances, be the origin of magnetism. Zunger and co-workers[144] have theoretically predicted that a cation vacancy can also induce a magnetic moment though long range ferromagnetic interaction amongst such moments (magnetic percolation) can not be realized without a very high concentration of these vacancies. We note however that to observe Kondo

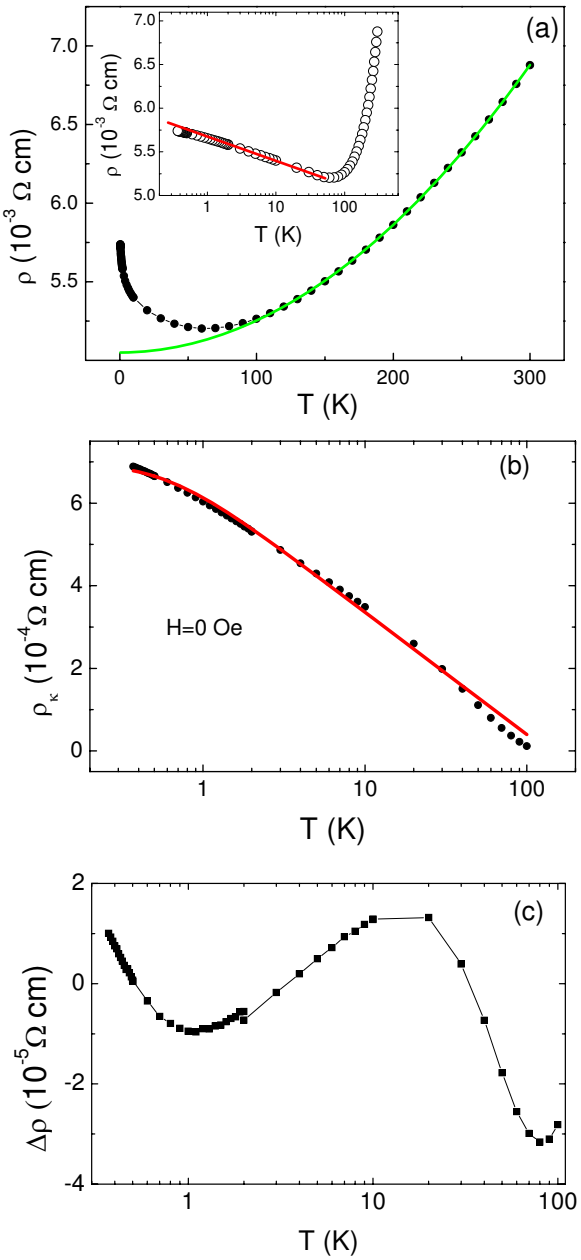

Figure 8.5: (a) Resistivity as a function of temperature down to 0.37 K of $Ti_{0.95}Nb_{0.05}O_2$ thin film (black dotted line) and the fitted resistivity due to contributions of impurity scattering, e-p scattering and e-e scattering (green solid line); (b) The Kondo resistivity as fitted by eq. 8.17 (The black dotted line is the subtracted Kondo resistivity and red solid line is the simulated data) (c) The difference between the subtracted Kondo resistivity and the fitting data

effect one does not need high magnetic impurity concentration or percolation. Also, according to the practical doping rule[43, 47], cation vacancy is easier to form in an anion rich condition, which means that the titanium vacancy is easier to form when the film is grown at 10^{-4} than grown at 10^{-5} Torr. Therefore, the cation vacancy origin of magnetic moment explains why Kondo effect is observed in the film grown at 10^{-4} rather than grown at 10^{-5} Torr. Moreover, the n-type dopant (niobium in our case) pushes the Fermi level upward, thereby reducing the formation energy of p-type defects (i.e. titanium vacancy), i.e. increasing the probability of forming magnetic moment V_{Ti} and hence giveing rise to Kondo effect in our TiO_2 system.

8.3 Summary

In summary, we have observed spin related electrical transport behavior in a transparent non-magnetic oxide doped with a non-magnetic dopant: $Ti_{1-x}Nb_xO_2$. Temperature dependent measurements of resistivity, Hall effect and magnetoresistance are used to substantiate the conclusion that magnetic moments responsible for Kondo scattering are present in the system. Since there is not any unpaired electron in titanium and niobium as evidenced by XPS results, the possible origin of such moments is attributed to cation vacancies. This observation of spin effect in a conventional non-magnetic oxide system doped with a non-magnetic ion under specific growth ambient conditions may open new avenues for manipulating defect ferromagnetism of interest to spintronics.

Chapter 9

Summary and Future Work

9.1 Summary

9.1.1 Transparent Conducting Oxides

Structural, electrical and optical characterizations were performed on a novel transparent conducting oxide (TCO) anatase Nb: TiO_2 thin films. By the study of films grown on various substrates and hence with different structural polymorphous, we demonstrate that epitaxial anatase Nb: TiO_2 grown at certain condition (P_{O2} $\sim 10^{-5}$ Torr by PLD) is an intrinsic n-type TCO with both its conductivity and optical transmittance comparable to that of the conventional transparent electrodes In-Sn-O which is currently widely used in optoelectronic devices. The high conductivity of anatase Nb: TiO_2 should be attributed to the high solution of niobium, acting as a very shallow donor, in TiO_2 matrix, and the small electron effective mass ($m^* \sim m_0$). Our growth parameter-phase diagram study shows that the deposition temperature can improve the carrier mobility considerably by enhancing the structural crystallinity, while the oxygen partial pressure can 'kill' number of electrons dramatically via inducing p-type native defects.

9.1.2 Diluted Magnetic Semiconductors

We investigated the structural, magnetic and electrical properties of several titanium oxide based diluted magnetic semiconductors. We found that the co-doping of niobium had positive effects on the micro-structure as well as the conductivity of Co:TiO_2, which give rise to the modulation of magnetism in this system. We demonstrated that $SrTiO_3$ doped by transition metal elements is at least not an RKKY induced ferromagnetic system, though our experiments have not excluded out the existence of intrinsic ferromagnetism in this system reported by other groups. We show that cobalt doped (La,Sr)TiO_3 is superparamagnetic at most of the growth conditions. And our Hall study on this system suggests that the magnitude of AHE rather than its occurrence is a criterion for intrinsic or extrinsic DMS. Niobium doped TiO_2 grown at P_{O2} of 10^{-4} Torr shows an unusual transport property at low temperatures, which is explained in terms of Kondo scattering. The local moment contributing to the Kondo effect is believed to arise from the defects generated during thin film growth by pulsed laser deposition.

9.2 Future Work

Niobium doped anatase TiO_2 is a novel oxide system which shows abundant interesting properties, such as transparency, excellent conductance, and magnetic effect. It is noticed that anatase TiO_2 has a very similar crystalline structure as $SrTiO_3$ (double perovskite structure for the former(Fig. 1.3(B) and single perovskite structure for the latter (Fig. 6.1)), and niobium doped $SrTiO_3$ grown at

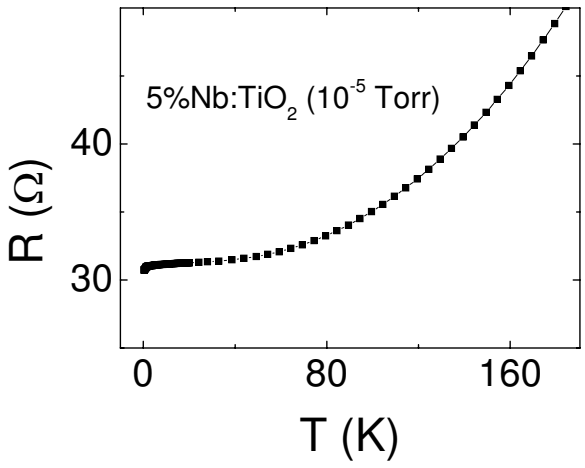

Figure 9.1: Resistance vs temperature for a 5% Nb: TiO_2 sample grown at an oxygen partial pressure of 10^{-5} Torr

certain condition shows superconductivity below around 0.3 K[40]; therefore, one may expect the possibility of superconductivity in anatase Nb:TiO_2. Indeed, our resistivity measurement, on a Nb:TiO_2 sample grown at certain condition, from 300 K down to 0.35 K (using He-3 system) shows the monoclinic decrease of resistivity without any saturation or upturn(Fig. 9.1). We have tried various growth conditions for high crystalline quality film in order to obtain superconductivity, however up to now, we haven't observed any zero resistivity above 0.35 K. Therefore, it would be helpful if one can measure resistivity down to further low temperatures using dilution refrigerator to see the possibility of superconductivity in this system.

Another work on anatase TiO_2 of great interest is to dope this material into p-type semiconductor in order to realize TiO_2 based p-n diodes. Most of the efforts on transition metal (vanadium, chromium, manganese, iron, cobalt, nickel, copper, and zinc) doped TiO_2 have been dedicated to search for ferromagnetism and very

little attention has been on the electronic properties. Therefore the search for p-type TiO_2 is still at its beginning stage. Since Ti in stoichiometric TiO_2 is in +4 state, one may be able to introduce holes by doping some low valence elements, such as Cu^{2+} and Zn^{2+}. To minimize the concentration of hole killers, such as oxygen vacancy (V_O) and titanium interstitial (Ti_i), it is helpful to grown thin films at high oxygen partial pressures.

Appendix A 1

Pulsed Laser Deposition Technique

Pulsed laser deposition (PLD) is considered to be one of the most important thin film deposition techniques for fabricating thin films of multi-elemental compounds.

A schematic of the pulsed laser deposition system is shown in Fig. A. 1.1. The system consists of three parts: an excimer laser, an optical set up, and a vacuum chamber. The excimer laser used in this work is a Lambda Physik excimer KrF UV laser which generate laser pulse with wavelength λ of 248 nm, pulse duration of 30 ns, maximal output energy of 1 J, and maximal pulsed rate of 30 Hz. Optical lens are applied to focus the laser beam into a millimeter size spot in order to achieve high energy density (typically $\sim$ 2 J/ cm^2) at the target site. The dielectric mirrors are used to deflect the beam towards the chamber and a fused silica window is employed to allow the laser beam to enter the vacuum chamber. The vacuum chamber is mainly equipped with pressure control set up, target carousel, and substrate holder with temperature controller. An oil-free turbo pump backed by a rotary pump enables the chamber to reach a vacuum of 10^{-7} Torr. Various high-purity gases are supplied to the chamber through a system of gas lines, valves, and flow controllers. An electrical motor controlled by a computer program is equipped to rotate the targets during deposition. The substrate holder integrated with a resistive heater is

able to control the deposition temperature through a transformerless power supply.

When the laser beam strikes a target (polycrystalline pellet), the laser energy is absorbed by the target material within a few nanometers of the surface layer, which heats up the material to an extremely high temperature (many times greater than the melting point of material). The surface layer of the target is thus evaporated and produces a forward-directed plasma plume containing high speed neutrals, ionized atoms and electrons of the target species. These ablated materials condense onto an appropriately heated substrate placed $5 \sim 10$ cm away from the target, as a result of which, the thin film nucleates and grows. Because of the non-equilibrium heating, during which there is little surface diffusion on the target and hence (little segregation) and the large density of the evaporated plume in which collisional processes average out the kinematics of the various species, the PLD process tends to closely reproduce the composition of the target in the film. This is one of the key advantages of this technique.

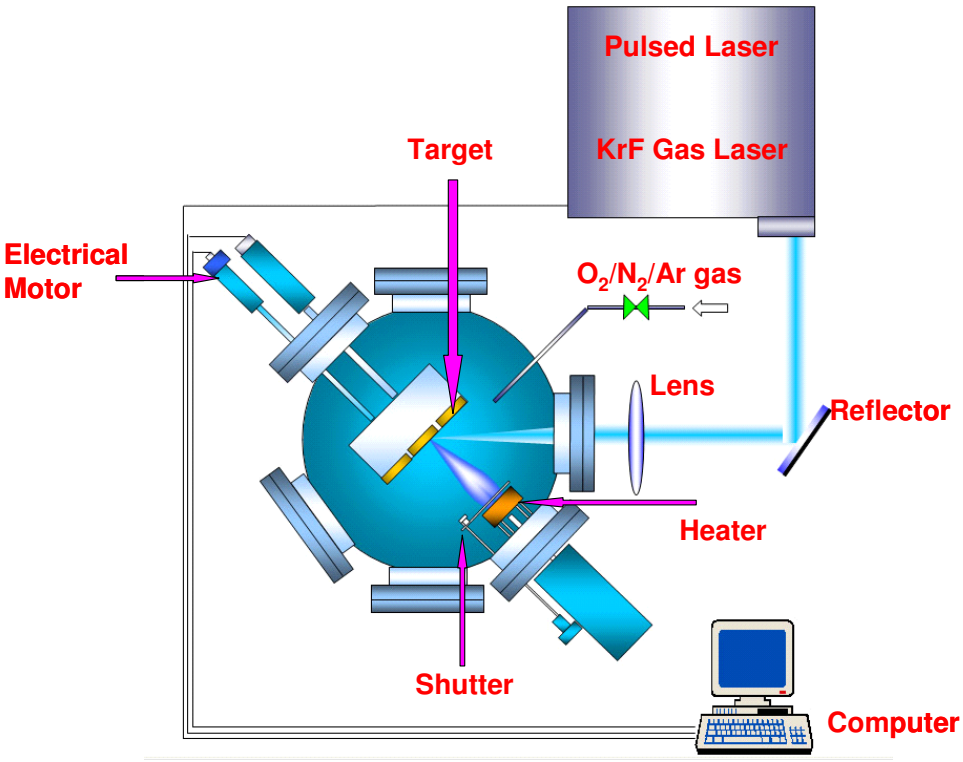

Figure A 1.1: Schematic of a pulsed laser deposition system

Appendix A 2

Four-Circle X-ray Diffraction

X-ray diffraction is a simple, yet powerful technique for structural characterization. It investigates the lattice spacings, phase composition, and epitaxy of a material.

A schematic of Siemens D5000 x-ray diffractmeter for our characterization studies is shown in Fig. A. 2.1. The x-ray, from Cu Kα source operated at 40kV, 30mA, is diffracted at the sample and received by a detector. For an ω - 2θ coupled scan (studying the lattice spacing etc.), the x-ray source is fixed, while the sample rotates with a steady angular velocity, and the detector rotates with an angular velocity satisfying $2\theta = 2\omega$. The X-rays are diffracted by atomic planes in the crystal and constructively interfere when the Bragg condition is satisfied:

$$2d\sin\theta = n\lambda \qquad \text{(A 2.1)}$$

where d is the spacing between atomic planes, θ=ω is the angle between atomic plane and the incident x-ray beam, λ is the x-ray wavelength, and n is the diffraction order. At this Bragg condition, a peak shows up at the intensity versus 2θ pattern. Therefore, the d value of those atomic planes, which are perpendicular to the beam plane, can be extracted by eq. A 2.1.

For a rocking curve (studying the degree of crystallinity of a film), both the source and detector (2θ) are fixed at the Bragg condition for a known lattice d value,

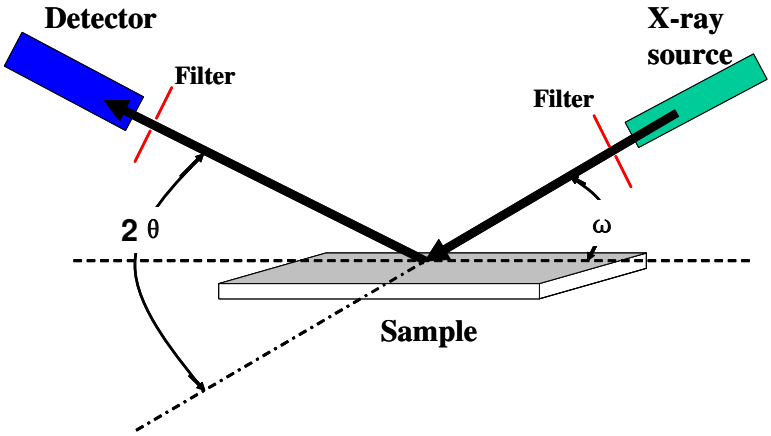

Figure A 2.1: Schematic of a X-ray diffraction technique

while the sample rotates (ω is changed around θ). The width of the resulting scan peak is an indicator to the degree of misorientation of the grains in the film. A narrower peak usually suggests a less misorientation of the grains hence a better crystalline quality.

Appendix A 3

Rutherford Backscattering Spectrometry and Channeling

Rutherford backscattering spectrometry (RBS) is a powerful technique for structural and compositional characterization of thin films or single crystals (Fig. A. 3. 1 (a). A beam of monoenergetic α particles ($^4He^{2+}$) is generated by an electrostatic accelerator, and directed towards the sample via the magnetic steering mechanism. When the α particles reach the sample surface, some of them are elastically scattered off the surface atoms, while the others enter the sample with energy loses along the way and are further scattered by the atoms inside of the sample (Fig. A. 3. 1 (b)). The number and energy of backscattered α particles are detected and the resulting spectrum is the intensity of backscattered particles as an function of energy.

Since the collision between α particle and atom is elastic, the energy (E) of the backscattered α particle is proportional to the atomic mass (M). The intensity of spectrum at a particular energy is proportional to the number of corresponding atoms inside of the sample. Thereby, the elemental composition of the sample can be readily determined by spectrum. The second application of RBS is to measure the thickness of the film because the width of the peak in the spectrum is proportional to the thickness (t) of the sample (Fig. A. 3. 1(b)).

The degree of crystalline order in a film can be determined via RBS by op-

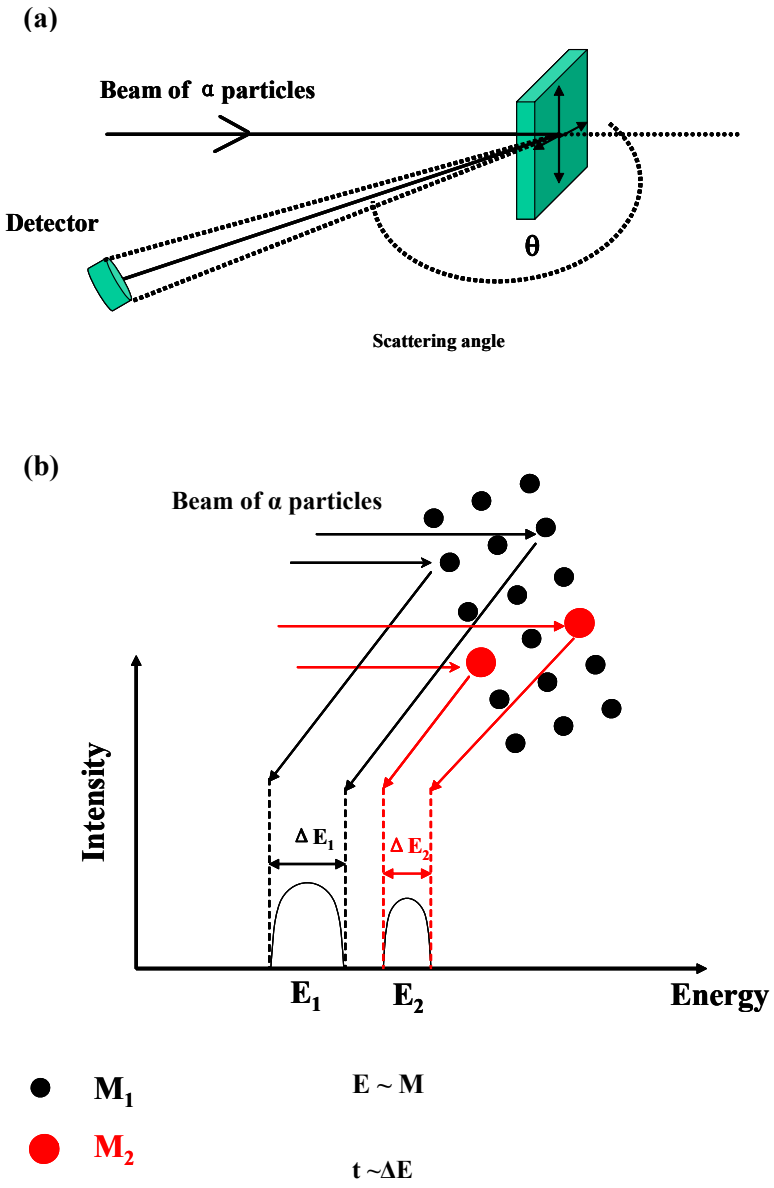

Figure A 3.1: (a) Schematic of a Rutherford backscattering system; (b) RBS spectrum in random (unaligned) mode.

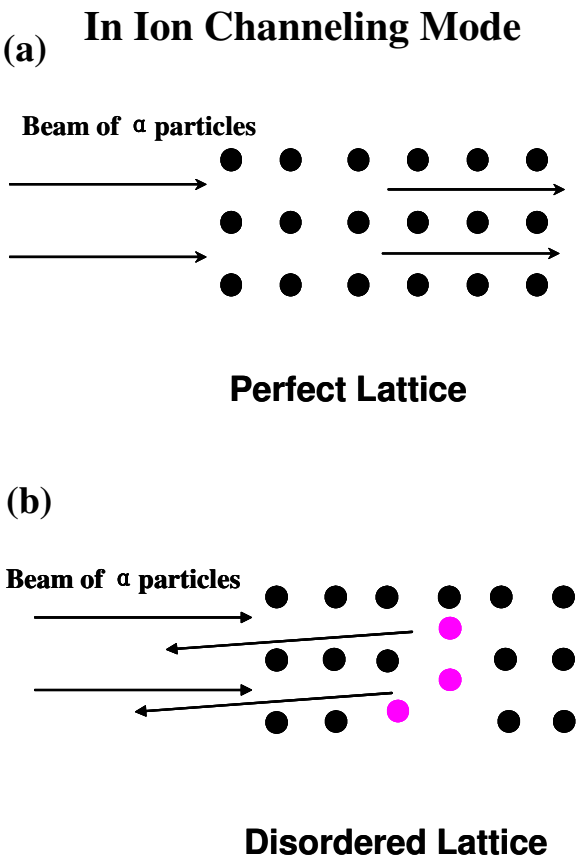

Figure A 3.2: RBS ion channeling mode for (a) a perfect crystalline lattice; (b) a disordered lattice.

erating the system in ion channeling mode. In this model, the sample is aligned with the particle beam (Fig. A. 3. 2 (a)). The beam passes through the sample with significantly reduced backscattering if the atoms are aligned perfectly in the sample. However, if some defects or disorder exist (Fig. A. 3. 2 (a)), some of the α particles will be scattered back leading to measurable intensity of spectrum. This intensity relative to the random (unaligned) backscattered signal (the ratio is called minimum channeling yield χ_{min}) is nearly proportional to the number of disordered atoms or defects and hence indicates the degree of crystallinity of the sample.

Appendix A 4

Atomic Force Microscopy

Atomic force microscopy (AFM) is a scanning probe microscopy for surface mapping with the resolution of fractions of a nanometer. As depicted in Fig. A. 4. 1, a sharp tip at the end of a microscale cantilever is used to scan the sample surface. When the tip is brought into close proximity of a sample surface, forces between the tip and the sample cause a deflection of the cantilever. This deflection is measured using a laser spot reflected from the top of the cantilever into a photodiode.

The AFM can be operated in several modes, such as contact mode and dynamic mode. The contact mode is simple, and used only when the force between the tip and the sample is repulsive. In this model, the pointed tip is brought into proximity to a sample surface. A feedback mechanism is employed to adjust the distance between tip and sample (z-direction) so as to maintain a constant repulsive force. The cantilever is scanned across the sample surface (in x, y directions), yielding a map of z-direction topography of the sample.

In a dynamic mode, the cantilever is oscillated at its mechanical resonance frequency. The variation of tip-sample-force modifies the amplitude, phase and resonance frequency of the oscillation. Thereafter, the changes in oscillation with respect to the external reference oscillation give information about the sample's surface characteristics.

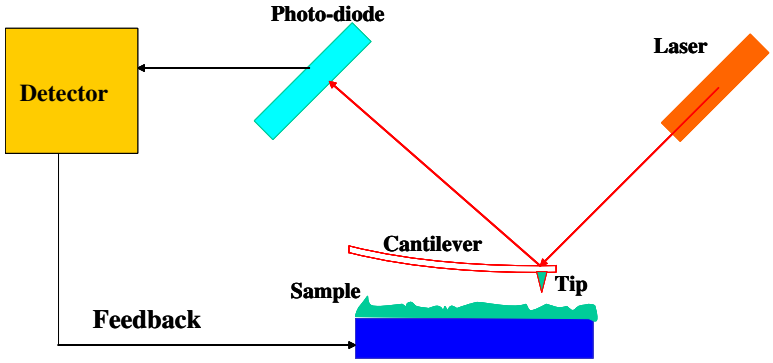

Figure A 4.1: Schematic of an atomic force microscopy system

The root-mean-square (rms) average roughness is calculated by the following equation:

$$rms = \sqrt{\frac{1}{A}\int\int r(x,y)dxdy} \qquad \text{(A 4.1)}$$

where A is the area of interest and r(x,y) is the roughness profile.

Appendix A 5

Transmission Electron Microscopy & Electron Energy Loss Spectroscopy

The transmission electron microscopy (TEM) and electron energy loss spectroscopy (EELS) studies in this thesis were done in collaboration with Prof. Browning at the department of chemical engineering and materials Science, University of California at Davis, and Prof. Salamanca-Riba at the department of Materials Science and Engineering at the University of Maryland, college park.

A 5.1 *Transmission Electron Microscopy*

TEM is an atomic resolution technique to characterize the structure of interface, grain boundaries, and different defects of a material. The basic parts of a TEM system are: an electron source generating a beam of electrons, lenses focusing the electron beam, and a main screen displaying the electron image transmitted through the specimen (Fig. A. 5. 1). The electrons generated by electron source are accelerated by an electric field and focused via condenser lenses (normally electromagnetic lenses) onto the sample. The electrons are scattered by the atoms in the material under investigation and the scattered angle is dependent on the density of atoms. Some portion of the electron beam travels through the specimen. A fluorescent screen is placed below the sample to collect the scattered electrons and

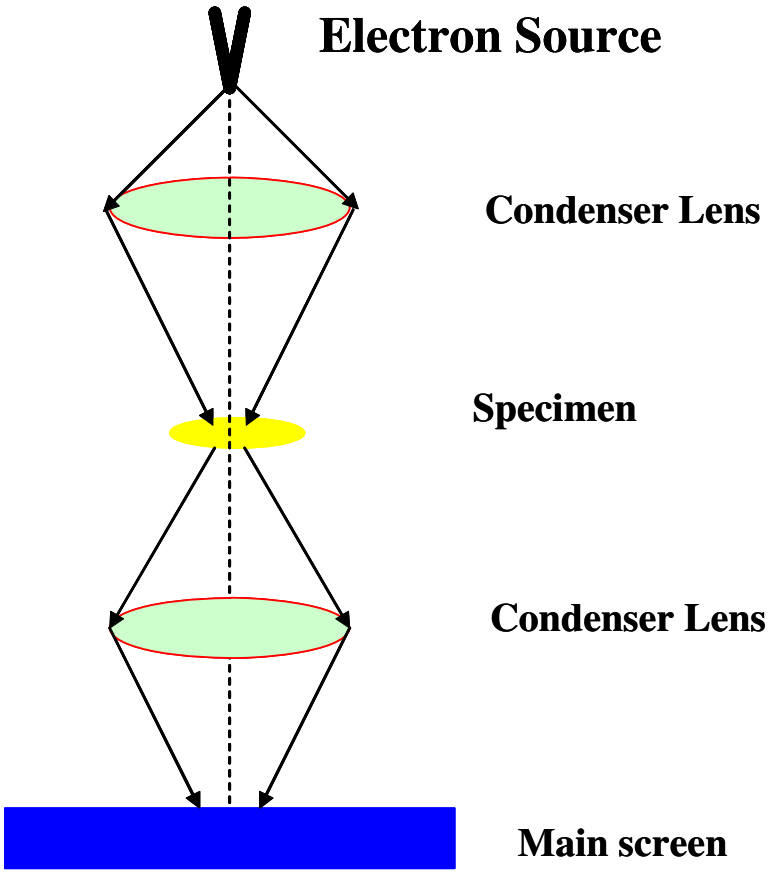

Figure A 5.1: Schematic of a transmission electron microscopy. The black arrows represent electron beams

its darkness at different parts is dependent on the electron density. The diffraction pattern shown in the screen is in the phase model. It can be transferred to a real image. A TEM image gives the information of the distribution of atoms in material. A TEM can be modified into a scanning transmission electron microscopy (STEM) by adding a system that allows the electron beam to scan over the sample in a raster. Detailed information about TEM/STEM technique employed in our work can be found in reference[145].

A 5.2 *Electron Energy Loss Spectroscopy*

Electron energy loss spectroscopy (EELS), usually incorporated with a TEM system, is a powerful tool for performing microanalysis and electronic structure study of a material. When a beam of electrons with a narrow range of kinetic energies strikes a specimen, the electrons can be scattered inelastically by the lattice atoms/ions. During this inelastic scattering, the incident electron transfers its energy to the lattice atom/ion, which gives rise to the inner shell ionizations of the latter. The amount of electron energy loss can be measured via an electron spectrometer. A typical EELS spectrum is the intensity of electrons as a function of the energy loss. Since the energy transferred is related to the ionization potential of the atoms/ions, the EELS spectrum provides information such as the chemical composition, atomic bonding etc. in a material. (For detailed information, please see ref.[145])

Appendix A 6

Magnetic Property Measurement System & Physical Property Measurement System

A 6 .1 *Magnetic Property Measurement System*

All of the magnetic measurements in this work were done by using a commercial Quantum Design magnetic property measurement system (MPMS) with Superconducting Quantum Interference Devices (SQUID) magnetometer. This MPMS system is mainly composed of the following parts: a dewar, a probe, a SQUID assembly, and an electronic control system. The schematic for MPMS is shown in Fig. A. 6. 1. The sample is mounted at one end of a sample rod. The position is adjusted so that the sample is at around the center of pick up coils. The magnetic field generated by a superconducting magnet can reach up to +/- 7 Tesla. Liquid He 4 in the dewar is used both for maintaining the superconducting state of the electromagnet and for cooling the sample space. The temperature can reach as low as 1.8 K, and as high as 400 K achieved by a heater system. The magnetization of a sample is measured via a SQUID magnetometer which consists of tiny loops of superconductors (with Josephson junctions). The schematics of Josephson junction and SQUID are given in Fig. A. 6. 2 (a) and (b), respectively. The Josephson junction contains two weakly coupled superconductors which are separated by a

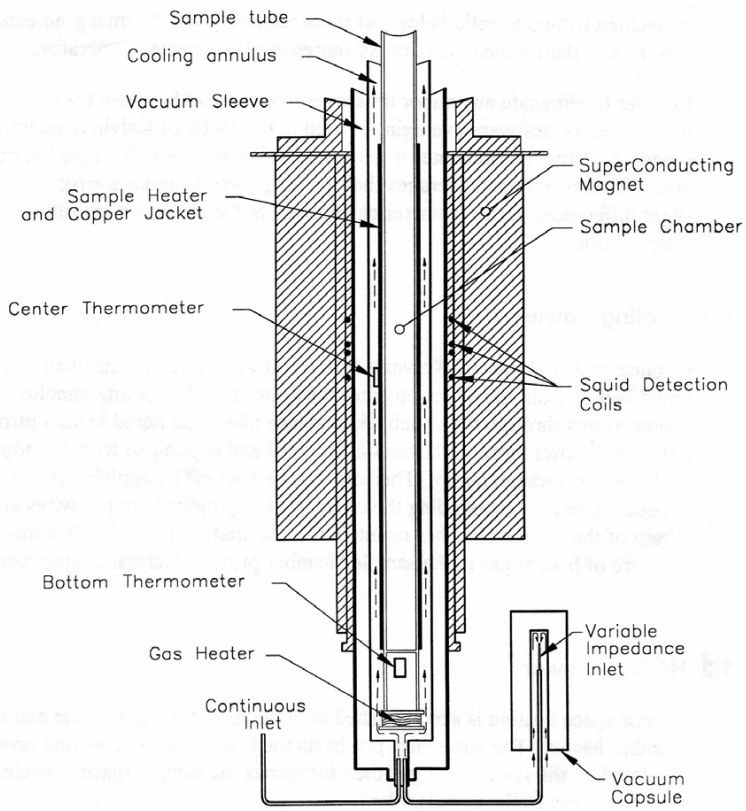

Figure A 6 .1: Schematic of the apparatus in an MPMS system. (Adapted from Quantum Design)

thin layer of insulator. The electron-pairs in superconductors can tunnel across the insulating barrier at zero voltage bias. The tunneling current i relates to the phase difference ($\Delta\phi_j$) between electron-pair wave in each superconductor as:

$$i = i_c sin\Delta\phi_j \qquad \text{(A 6 .1)}$$

where i_c is the critical current of a Josephson junction.

A simple SQUID consists of a closed loop of superconductor with two Joseph-

son junctions. When a magnetic field (B) is applied perpendicular to the plane of the loop, a phase difference $\Delta\phi_B = 4\pi\Phi\frac{h}{e}$, is produced in the electron-pair wave in the superconductor regime, where Φ is the flux across the loop. A small current i is also induced to flow around the loop, producing a phase difference ($\Delta\phi(j)$) across each Josephson junction. Thereby, the total phase difference is:

$$\Delta\phi_{tot} = \Delta\phi_B + 2\Delta\phi(j) \qquad \text{(A 6 .2)}$$

The total phase difference must equal to $2n\pi$. Integrating equation A. 6. 2 into equation A. 6. 1, we get:

$$i = i_c sin\Delta\phi_j = i_c sin(\frac{\Delta\phi_{tot} - \Delta\phi_B}{2}) = i_c sin(2\pi\frac{h}{e}) = i_c sin(\pi\Phi/\Phi_0) \qquad \text{(A 6 .3)}$$

here $\Phi_0 = \frac{2e}{h} = 2.07\times10^{-15}$ Wb is called fluxon. Therefore, the current has a periodic dependence on the magnitude of magnetic flux Φ.

For the direct current (DC) magnetization measurement performed in this work, SQUID sensor is used to measure the global magnetic moment of a sample. The sample is magnetized by an external magnetic field and this magnetized sample with magnetization of M can generate magnetic flux Φ through the SQUID coils and hence causes a electrical output (i). The magnetization (M) of a sample is computed by this electrical output. Since the period of variation Φ_0 in equation A 6. 3 is a very small value, SQUID sensor can detect very weak magnetic moment of a sample (as low as $\sim 10^{-8}$ emu).

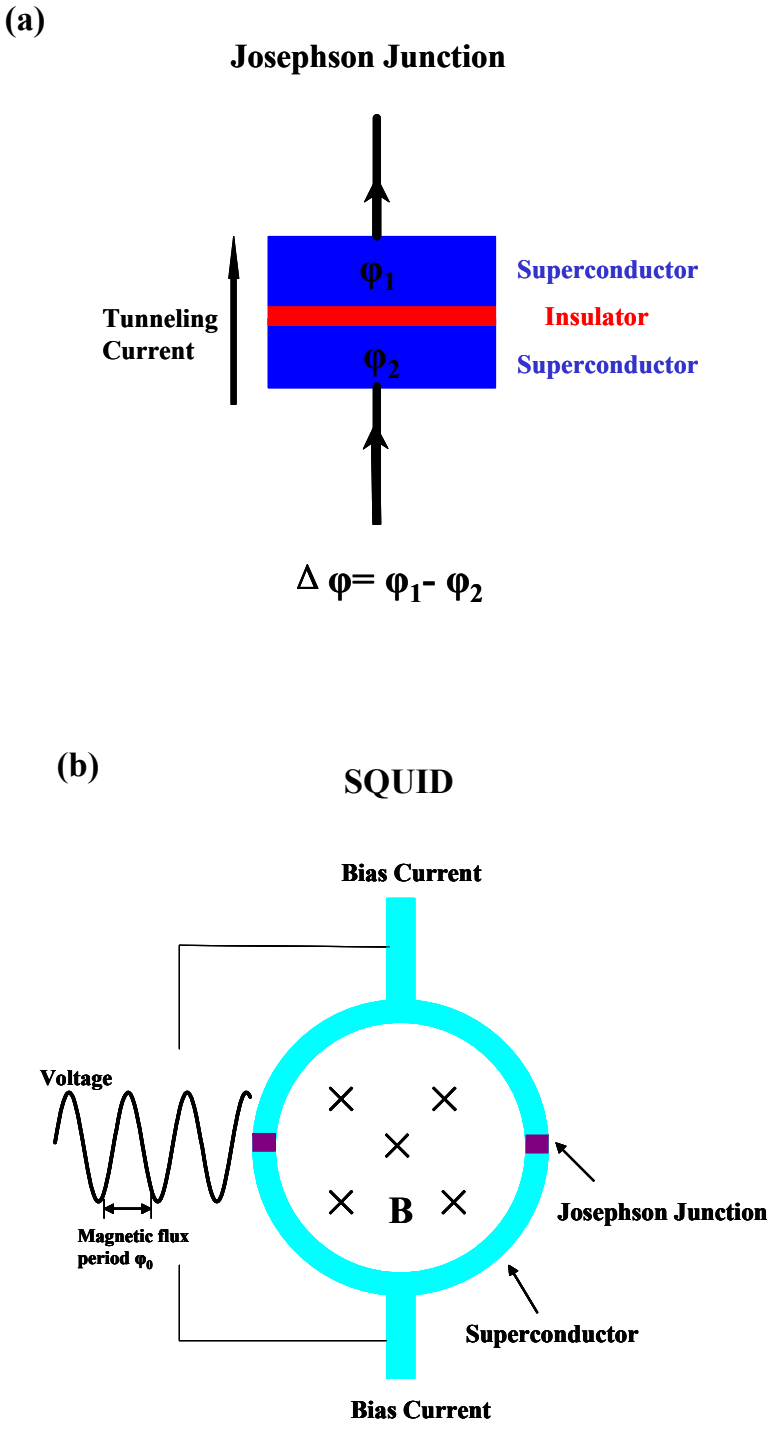

Figure A 6 .2: Schematic of (a) a Josephson junction; (b) a SQUID

A 6 .2 *Physical Property Measurement System*

The electrical transport measurements were performed using DC resistivity option in a Quantum Design physical property measurement system (PPMS). The PPMS is capable of temperatures between 0.35 K and 400 K, and magnetic fields up to +/- 14 T. The sample is mounted on a puck which is loaded in the PPMS chamber during the measurement. A typical pattern for resistivity and Hall measurements is depicted in Fig. A. 6. 3. The standard four-probe (two current contacts, two voltage contacts) method is employed in order to get rid of the contact resistance. Gold wire with a diameter of ~ 0.05 mm is used to connect between the sample and the corresponding channels on the puck. The contacts are usually made by Ag/In solder. The resistivity of the specimen is:

$$\rho_{xx} = R_{xx} t \; w/l \tag{A 6 .4}$$

where t is the thickness of the sample, w and l are the width and length of the sample bridge (shown in Fig. A 6.3). R_{xx} is the resistance of the specimen recorded by PPMS system.

The Hall measurement is performed with the magnetic field (H) perpendicular to the sample plane. To avoid magnetoresistance contribution, the magnetic field is swept from negative to positive and the Hall resistance is obtained by:

$$R_{xy}(H) = \frac{R_{xy}(H) - R_{xy}(-H)}{2} \tag{A 6 .5}$$

And, the Hall resistivity is:

$$\rho_{xy} = R_{xy} t \tag{A 6 .6}$$

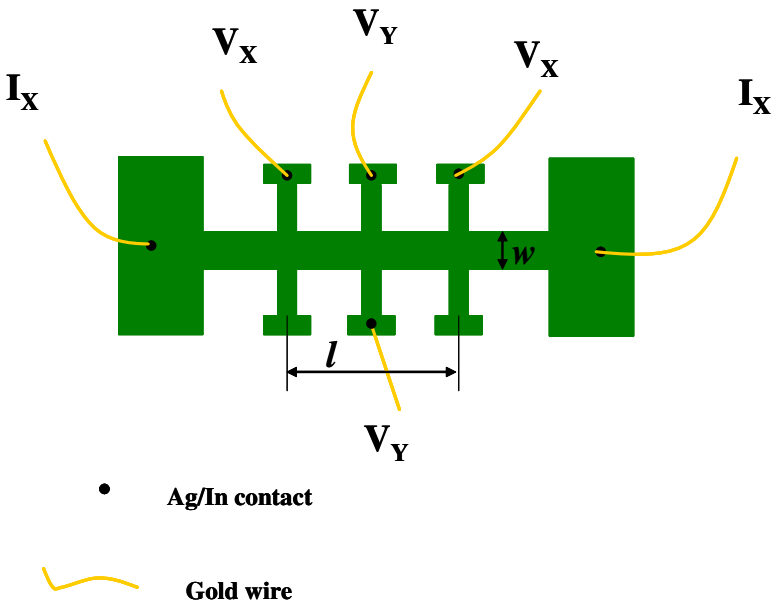

Figure A 6 .3: The Hall bar schematics: V_x and I_x are connected to the voltage and current contacts, respectively, on sample puck for resistance (R_{xx})measurement. V_y and I_x are connected to the voltage and current contacts respectively for Hall (R_{xy})measurement.

In a non-magnetic system, the Hall resistivity is a linear function of the magnetic field (for magnetic systems, see section 7. 2. 1)

$$\rho_{xy} = R_H \mu_0 H \tag{A 6 .7}$$

where μ_0= $4\pi \times 10^{-7}$ N A^{-2} (SI unit) is the permeability of free space, and R_H is called Hall constant which in a simple Drude model is written as

$$R_H = \frac{n\mu_e^2 - p\mu_p^2}{e(n\mu_e + p\mu_p)^2} \tag{A 6 .8}$$

If there is only one type of carriers (or one dominates over the other), the sign of R_H determines the type of carriers, i.e. negative R_H indicates that the carriers are electrons while positive R_H indicates that the carriers are holes. And one can obtain the carrier concentration easily by the following equation (for example, electrons are the major charge carriers)

$$n = \frac{1}{eR_H} \tag{A 6 .9}$$

One can further obtain the mobility of charge carriers by

$$\mu_e = \frac{1}{ne\rho_{xx}} \tag{A 6 .10}$$

Appendix A 7

X-ray Photoelectron Spectroscopy

X-ray photoelectron spectroscopy (XPS) is a technique for determining the elemental composition, chemical state and electronic state of the elements on the surface of a material. The surface layer that XPS can probe is typically below 10 nm. The basic parts of a XPS system are: a source of X-ray, ultra-high vacuum (UHV) stainless steel chamber, an electron energy analyzer and detector(Shown in Fig. A. 7. 1).

The sample is mounted in the chamber under UHV condition. X-ray irradiates the sample and gives rise to an emission of electrons from the core level of the elements at sample surface. The number of electrons representing the proportion of the corresponding elements on the surface is counted by the detector after the electrons are separated by the analyzer according to their energies. The binding energy (E_B) of electrons, reflecting the atomic bonding strength of electrons at material surface and hence the oxidation state of specific elements, is obtained from the measured kinetic energy (E_K) of the emitted electrons according to the following equation:

$$E_B = hv - E_K - \Phi_S \qquad \text{(A 7.1)}$$

where hv is the energy of the incident x-ray photons, Φ_S is the work function of the spectrometer.

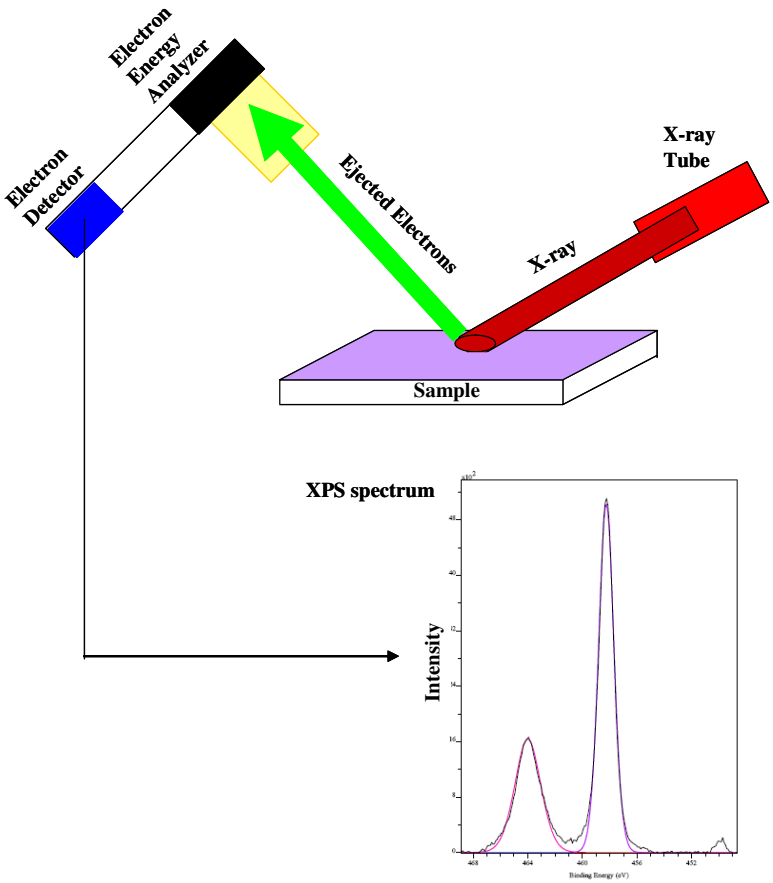

Figure A 7.1: Schematic of an X-ray photoelectron spectroscopy system

A typical XPS spectrum is a plot of the number of detected electrons as a function of the electron binding energies. The XPS peaks correspond to the electron configuration in the atoms, such as 1s, 2s etc. And the binding energy of the peaks enables us to identify the element and its electronic state in the surface material. The ratio of the XPS peaks for different elements tells us the amount information of each element.

Appendix A 8

Ultraviolet-Visible spectroscopy

The Ultraviolet (UV)-Visible spectroscopy is a simple technique to study the fundamental optical properties, such as transmittance and absorption of a material in response to the light in the visible and near UV ranges. A spectrophotometer is mainly composed of: a light source, sample holders, a monochromator, and a detector (Fig. A. 8. 1). A substrate, which is the same as the one used in the sample under investigation, is a reference for subtracting the absorption of substrate in the sample. When light is shining on a sample, if the photon energy is less than the energy gap of the material, light will pass through the material without being absorbed, leading to a high transmittance (T=I_{out}/I_{in}). However, if the photon energy is greater than the energy gap of the material, the electrons absorb the photon energy and jump to higher energy levels. In this case, the transmission of the material is low. The absorption (α) can be derived from transmittance using the following equation,

$$\alpha = -\frac{1}{d}\ln(\frac{T}{1-R}) \qquad \text{(A 8.1)}$$

where d is the thickness of the sample, T is the transmittance and R is the reflection.

A typical UV-visible spectrum is a plot of transmittance or absorption versus

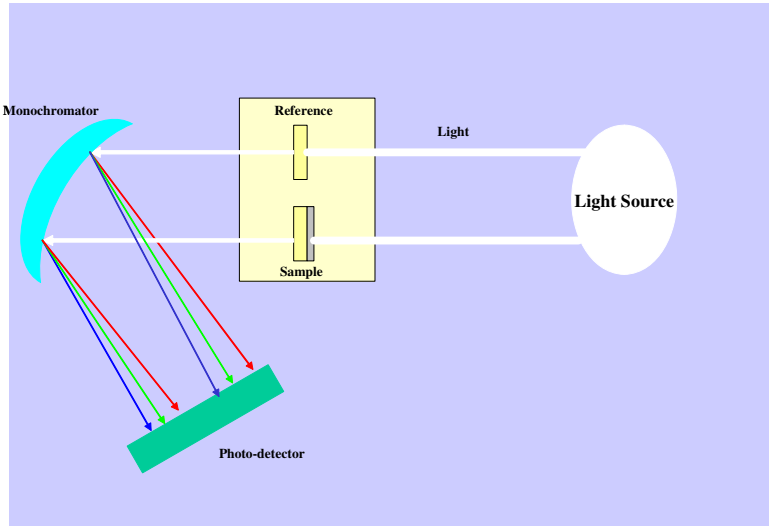

Figure A 8.1: Schematic of an Ultraviolet (UV)-Visible spectrophotometer

light wavelength. From the UV-visible spectrum, one can calculate the optical band gap of the material under study (the details have been included in Chapter 2).

Bibliography

[1] Holger T. Grahn, *Introduction to Semiconductor Physics* (World Scientific, 1999)

[2] Karlheinz Seeger, *Semiconductor Physics: An Introduction* (Springer Series in Solid-State Sciences, 2004)

[3] N. W. Ashcroft & N. D. Mermin, *Solid State Physics* (Saunders College Publishing, 1976).

[4] For a review, see, F. A. Grant, Rev. Mod. Phys. 31, 646 (1959); J. B. Goodenough, Prog. Solid State Chem. 5, 145 (1971); V. E Henrich, Rep. Prog. Phys. 48, 1481 (1985).

[5] J. Muscat, V. Swamy, and N. M. Harrison, Phys. Rev. B, 65, 224112 (2002).

[6] J. K. Burdett, T. Hughbanks, G. J. Miller, J. W. Richardson, and J. V. Smith, J. Am. Chem. Soc. 109, 3639 (1987).

[7] V. K. Rao, S. V. N. Naidu, and L. Iyengar, J. Am. Ceram. Soc. 53, 124 (1970).

[8] C. J. Howard, T. M. Sabine, and F. Dickson, Acta Crystallogr., Sect. B: Struct. Sci. 47, 462 (1991).

[9] S.-D. Mo and W. Y. Ching, Phys. Rev. B 51, 13023 (1995).

[10] K.M. Glassford and J.R. Chelikowsky, Phys. Rev. B 46, 1284 (1992).

[11] M. Ramamoorthy, R.D. King-Smith, and D. Vanderbilt, Phys. Rev. B 49, 7709 (1994).

[12] P.J.D. Lindan, N.M. Harrison, M.J. Gillan, and J.A. White, Phys. Rev. B 55, 15919 (1997).

[13] S.P. Bates, G. Kresse, and M.J. Gillan, Surf. Sci. 385, 386 (1997).

[14] J. Goniakowski, J.M. Holender, L.N. Kantorovich, M.J. Gillan, and J.A. White, Phys. Rev. B 53, 957 (1996).

[15] J. Pascual, J. Camassel, and H. Mathieu, Phys. Rev. B 18, 5606 (1978)

[16] H. Tang, H. Berger, P. E. Schmid, F. Levy, and G. Burri, Solid State Commun. 87, 847 (1993).

[17] R.M. Dreizler and E.K.U. Gross, Density Functional Theory, An Approach to the Quantum Many-Body Problem (Springer-Verlag, Berlin, 1990).

[18] R. Sanjines, H. Tang, H. Berger, F. Gozzo, G. Margaritondo, and F. Levy, J. Appl. Phys. 75, 2945 (1994).

[19] H. Tang, K. Prasad, R. Sanjines, P.E. Schmid, and F. Levy, J. Appl. Phys. 75, 2042 (1994).

[20] L. Forro, O. Chauvet, D. Emin, L. Zuppiroli, H. Berger, and F. Levy, J. Appl. Phys. 75, 633 (1994).

[21] H. Tang, F. Levy, H. Berger, and P.E. Schmid, Phys. Rev. B 52, 7771 (1995).

[22] A. Fujishima and K. Honda, Nature 238, 37 (1972);

[23] For a review, see V. E Henrich, Rep. Prog. Phys. 48, 1481 (1985).

[24] S. J. Tauster, S. C. Fung and R. L. Garten, J. Am. Chem. Soc. 100, 170 (1978).

[25] B. O'Regan and M. Gratzel, Nature 353, 737, (1991).

[26] M. R. Hoffmann, S. T. Martin, W. Choi, and D. W. Bahnemann, Chem. Rev. (Washington, D.C.) 95, 69 (1995) and references therein.

[27] T. Minami, MRS Bulletin 25, 38 (2000).

[28] D. S. Ginley and C. Bright, MRS Bulletin 25, 15 (2000).

[29] R. G. Gordon, MRS Bull. 52, 15 (2000)

[30] T. Minami, Semicond. Sci. Technol. 20, S 35 (2005)

[31] Taken from http://www.techonecomputers.biz/

[32] Taken from www.lightemittingdiodes.org

[33] N. F. Mott, Proc. Phys. Sot. A 62, 416 (1949); Phil. Mag. 6, 287(1961); Adv. Phys. 16, 49 (1967).

[34] For a review, see M. N. Alexander and D. F. Holcomb, Rev. Mod. Phys., 40, 815 (1968)

[35] Y. Pleskov et al. Semiconductor Photoelectrochemistry; Consultant Bureau: New York, 1986.

[36] E. Burstein, Phys. Rev. 93, 632 (1954); T. S. Moss, Proc. Phys. Soc. London, Sect. B 67, 775 (1954)

[37] Y. Furubayashi, T. Hitosugi, Y. Yamamoto, K. Inaba, G. Kinoda, Y. Hirose, T. Shimada, and T. Hasegawa, Appl. Phys. Lett. 86, 252101 (2005).

[38] Q. Wan and T. H. Wang, Appl. Phys. Lett. 88, 226102 (2006)

[39] Y. Furubayashi, T. Hitosugi, and T. Hasegawa, Appl. Phys. Lett. 88, 226103 (2006)

[40] A. Leitner, C. T. Rogers, J. C. Price, David A. Rudman, and D. R. Herman, Appl. Phys. Lett. 72, 3065 (1998).

[41] S. A. Chambers, Y. Gao, S. Thevuthasan, Y. Liang, N. R. Shivaparan and R. J. Smith, J. Vac. Sci. Technol. A 14(3), 1995;

[42] D. Morris, Y. Dou, J. Rebane, C. E. J. Mitchell, and R. G. Egdell, D. S. L. Law, A. Vittadini, and M. Casarin, Phys. Rev. B 61, 13445 (2000)

[43] A. Zunger, Appl. Phys. Lett. 83, 57, (2003).

[44] Y. Matsumoto, M. Murakami, T. Shono, T. Hasegawa, T. Fukumura, M. Kawasaki, P. Ahmet, T. Chikyow, S. Koshihara, and H. Koinuma, Science 291, 854 (2001).

[45] S. R. Shinde, S. B. Ogale, S. D. Sarma, J. R. Simpson, H. D. Drew, S. E. Loafland, C. Lanci, J. P. Biban, N. D. Browning, V. N. Kulkarni, J. Higgins, R. P. Sharma, R. L. Greene, and T. Venkatesan, Phys. Rev. B 67, 115211 (2003)

[46] S. A. Chambers, S. M. Heald, and T. Droubay, Phys. Rev. B 67, 100401 (2003).

[47] S. Na-Phattalung, M. F. Smith, K. Kim, M.-H. Du, S.-H. Wei, S. B. Zhang, and S. Limpijumnong, Phys Rev. B 73, 125205 (2006)

[48] M.A.B. Gomes et al., J. Electrochem. Soc. 137, 3067 (1990); V.I. Nefedov, M.N. Firsov, I.S. Shaplygin, J. Electron Spectrosc. Relat. Phenom. 26, 65 (1982).

[49] D. Gonbeau et al., Surf. Sci. 254, 81 (1991); M. Murata, K. Wakino, S. Ikeda, J. Electron Spectrosc. Relat. Phenom. 6, 459 (1975).

[50] A. Aharoni, *Introduction to the theory of ferromagnetism* (Oxford University Press, Oxford, 1996)

[51] S. Blundell *Magnetism in Condensed Matter (Oxford Maser Series in Condensed Matter Physics)* (Oxford University Press, Oxford, 2001)

[52] Robert M. White, *Quantum theory of magnetism* (Springer-Verlag, 1983)

[53] H. Ohno, Science 281, 951(1998).

[54] S. A. Wolf, D. D. Awschalom, R. A. Buhrman, J. M. Daughton, S. von Molnr, M. L. Roukes, A. Y. Chtchelkanova, and D. M. Treger, Science 294, 1488 (2001).

[55] I. Zutic, J. Fabian and S. Das Sarma, Rev. Mod. Phys. 76, 323 (2004)

[56] M. Julliere, Phys. Lett. 54A, 225C226 (1975)

[57] S. Datta and B. Das, Appl. Phys. Lett. 56, 665 (1990).

[58] R. Fiederling, M. Keim, G. Reuscher, W. Ossau, G. Schmidt, A. Waag, and L. W. Molenkamp, Nature 402, 787 (1999).

[59] G. A. Prinz, Science 282, 1660 (1998)

[60] A. Fert, J.-M. George, H. Jaffrcs, R. Mattana, and P. Seneor, Europhysics News, Vol. 34 No. 6 (2003)

[61] T. Jungwirth, Jairo Sinova, J. Masek, J. Kucera, and A. H. MacDonald, Rev. Mod. Phys. 78, 809 (2006).

[62] J. A. Gaj, J. Ginter, and R. R. Galazka, Phys. Status Solidi B 89, 655 (1978); M. Jaczynski, J. Kossut, and R. R. Galazka, Phys. Status Solidi B 88, 73(1978).

[63] H. Ohno, H. Munekata, T. Penney, S. von Molnar, and L. L. Chang, Phys. Rev. Lett. 68, 2664 (1992)

[64] T. Dietl, A. Haury, and Y. M. d'Aubigne, Phys. Rev. B 55, R 3347 (1997).

[65] D. V. Baxter, D. Ruzmetov, J. Scherschligt, Y. Sasaki, X. Liu, J. K. Furdyna, and C. H. Mielke, Phys. Rev. B 65, 212407 (2002).

[66] M. Tanaka, and Y. Higo, 2001, Phys. Rev. Lett. 87, 026602.

[67] R. Mattana, M. Elsen, J. M. George, H. Jaffrs, F. N. Van, Dau, A. Fert, M. F. Wyczisk, J. Olivier, P. Galtier, B. Lpine, A. Guivarch, and G. Jzquel, Phys. Rev. B 71, 075206 (2005).

[68] H. Saito, S. Yuasa, and K. Ando, Phys. Rev. Lett. 95, 086604 (2005)

[69] K. F. Eid, M. B. Stone, K. C. Ku, P. Schiffer, and N. Samarth, Appl. Phys. Lett. 85, 1556 (2004)

[70] Ohno, H., D. Chiba, F. Matsukura, T. Omiya, E. Abe, T. Dietl, Y. Ohno, and K. Ohtani, Nature (London) 408, 944 (2000);

[71] Chiba, D., M. Yamanouchi, F. Matsukura, and H. Ohno, Science 301, 943 (2003)

[72] Ruster, C., T. Borzenko, C. Gould, G. Schmidt, L. W. Molenkamp, X. Liu, T. J. Wojtowicz, J. K. Furdyna, Z. G. Yu, and M. E. Flatt, Phys. Rev. Lett. 91, 216602 (2003)

[73] T. Dietl, H. Ohno, F. Matsukura, J. Cibert, and D. Ferrand, Science 287, 1019 (2000).

[74] S.A. Chambers, S. Thevuthasan, R. F. C. Farrow, R. F. Marks, J. U. Thiele, L. Folks, M. G. Samant, A. J. Kellock, N. Ruzycki, D. L. Ederer, and U. Diebold, Appl. Phys. Lett. 79, 3467 (2001).

[75] M. Venkatesan, C. B. Fitzgerald, J. G. Lunney, and J. M. Coey, Phys. Rev. Lett. 93, 177206 (2004).

[76] S. R. Shinde, S. B. Ogale, J. S. Higgins, H. Zheng, A. J. Millis, R. Ramesh, R. L. Greene, and T. Venkatesan, Phys. Rev. Lett. 92, 166601 (2004).

[77] J.-Y. Kim, J.-H. Park, B.-G. Park, H.-J. Noh, S.-J. Oh, J. S. Yang, D.-H. Kim, S. D. Bu, T.-W. Noh, H.-J. Lin, H.-H. Hsieh, and C. T. Chen, Phys. Rev. Lett. 90, 017401 (2003).

[78] D. H. Kim, J. S. Yang, K. W. Lee, S. D. Bu, T. W. Noh, S.-J. Oh, Y.-W. Kim, J.-S. Chung, H. Tanaka, H. Y. Lee, and T. Kawai, Appl. Phys. Lett. 81, 2421 (2002).

[79] N. H. Hong, J. Sakai, W. Prellier, and A. Hassini, Appl. Phys. Lett. 83, 3129 (2003).

[80] D. C. Kundaliya, S. B. Ogale, S. E. Lofland, S. Dhar, C. J. Metting, S. R. Shinde, Z. Ma, B. Varughese, K.V. Ramanujachary, L. Salamanca-Riba and T.

Venkatesan, Nature Materials 3, 709 (2004);

[81] S. B. Ogale, R. J. Choudhary, J. P. Buban, S. E. Lofland, S. R. Shinde, S. N. Kale, V. N. Kulkarni, J. Higgins, C. Lanci, J. R. Simpson, N. D. Browning, S. Das Sarma, H. D. Drew, R. L. Greene, and T. Venkatesan, Phys. Rev. Lett. 91, 077205 (2003).

[82] Y. G. Zhao, S. R. Shinde, S. B. Ogale, J. Higgins, R. J. Choudhary, V. N. Kulkarni, R. L. Greene, T. Venkatesan, S. E. Lofland, C. Lanci, J. P. Buban, N. D. Browning, S. Das Sarma, and A. J. Millis, Appl. Phys. Lett. 83, 2199 (2003).

[83] P. A. Stampe, R. J. Kennedy, X. Yan, and J. S. Parker, J. Appl. Phys. 92, 7114 (2002).

[84] Y. L. Soo, G. Kioseoglou, S. Kim, and Y. H. Kao, P. Sujatha Devi, John Parise, R. J. Gambino, and P. I. Gouma, Appl. Phys. Lett. 81, 655 (2002).

[85] J. M. D. Coey, M. Venkatesan, and C. B. Fitzgerald, Nat. Mater. 4,173 (2005).

[86] T. C. Kaspar, S. M. Heald, C. M. Wang, J. D. Bryan, T. Droubay, V. Shutthanandan, S. Thevuthasan, D. E. McCready, A. J. Kellock, D. R. Gamelin, and S. A. Chambers, Phys. Rev. Lett. 95, 217203 (2005); T. C. Kaspar, T. Droubay, V. Shutthanandan, S. M. Heald, C. M. Wang, D. E. McCready, S. Thevuthasan, J. D. Bryan, D. R. Gamelin, A. J. Kellock, M. F. Toney, X. Hong, C. H. Ahn, and S. A. Chambers, Phys. Rev. B 73, 155327 (2006).

[87] J. M. D. Coey, M. Venkatesan, P. Stamenov, C. B. Fitzgerald, and L. S. Dorneles, Phys. Rev. B 72, 024450 (2005).

[88] A. J. Kaminski and S. Das Sarma, Phys. Rev. Lett. 88, 247202 (2002); Phys. Rev. B 68, 235210 (2003);

[89] M. J. Calderon and S. Das Sarma, Phys. Rev. B 75, 235203 (2007).

[90] M. A. Ruderman and C. Kittel, Phys. Rev. 96, 99 (1954)

[91] T. Kasuya, Prog. Theor. Phys. 16, 45 (1956).

[92] K. Yosida, Phys. Rev. 106, 893 (1957).

[93] U. Mizutani, *Introduction to the electron theory of metals* (Cambridge University Press, 2001)

[94] T. Zhao, S. R. Shinde, S. B. Ogale, H. Zheng, T. Venkatesan, R. Ramesh, and S. Das Sarma, Phys. Rev. Lett. 94, 126601 (2005).

[95] G. Shirane and Y. Yamada, Phys. Rev. 177, 858 (1969).

[96] M. Cardona, Phys. Rev. 140, A651 (1965).

[97] O. N. Tufte and P. W. Chapman, Phys. Rev. 155, 796, (1967).

[98] H. P. R. Frederikse, W. R. Thurber, and W. R. Hosler, Phys. Rev. 134, A442 (1964).

[99] J. F. Schooley, W. R. Hosler, E. Ambler, J. H. Becker, M. L. Cohen, and C. S. Koonce, Phys. Rev. Lett. 14, 305 (1965).

[100] Y. Tokura, Y. Taguchi, Y. Okada, Y. Fujishima, T. Arima, K. Kumagai, and Y. Iye, Phys. Rev. Lett. 70, 2126 (1993).

[101] A. Leitner, D. Olaya, C. T. Rogers, and J. C. Price, Phys. Rev. B 62, 1408 (2000)

[102] R. Ranchal, M. Bibes, A. Barthlmy, K. Bouzehouane, S. Guyard, E. Jacquet, J.-P Contour, C. Pascanut, P. Berthet, and N. Dragoe J. Appl. Phys. 98, 013514 (2005)

[103] G. Herranz, R. Ranchal, M. Bibes, H. Jaffres, E. Jacquet, J. L. Maurice, K. Bouzehouane, F. Wyczisk, E. Tafra, M. Basletic, A. Hamzic, C. Colliex, J.-P. Contour, A. Barthelemy, A. Fert, Phys. Rev. Lett. 96, 027207 (2006); G. Herranz, M. Basletic, M. Bibes, R. Ranchal, A. Hamzic, E. Tafra, K. Bouzehouane, E. Jacquet, J. P. Contour, A. Barthlmy, and A. FertPhys. Rev. B 73, 064403 (2006).

[104] Y. Matsumoto, R. Takahashi, M. Murakami, T. Koida, X. J. Fan, T. Hasegawa, T. Fukumur, M. Kawasaki, S. Koshihara and H. Koinuma, Jpn, J. Appl. Phys., 40, L1204 (2001)

[105] J. Inaba and T. Katsufuji, Phys. Rev. B 72, 052408 (2005)

[106] H. Iwasawa, K. Yamakawa, T. Saitoh, J. Inaba, T. Katsufuji, M. Higashiguchi, K. Shimada, H. Namatame, and M. Taniguchi, Phys. Rev. Lett. 96, 067203 (2006)

[107] W. Ramadan, S. B. Ogale, S. Dhar, S. X. Zhang, D. C. Kundaliya, I. Satoh, and T. Venkatesan Appl. Phys. Lett. 88, 142903 (2006)

[108] R. Bouzerar, G. Bouzerar, T. Ziman, Phys. Rev. B 73, 024411 (2006)

[109] W. Wu, F. Lu, K. H. Wong, G. Pang, C. L. Choy, and Yuheng Zhang, J. Appl. Phys. 88, 700 (2000)

[110] M. Sasaki, P. E. Jonsson, H. Takayama, and H. Mamiya, Phys. Rev. B 71, 104405 (2005)

[111] J. P. Bouchaud, J. Phys. I 2, 1705 (1992).

[112] M. Sasaki and K. Nemoto, J. Phys. Soc. Jpn. 69, 2642 (2000).

[113] E. Hall, American Journal of Mathematics vol 2 (1879).

[114] *The Hall effect and Its applications,* edited by C. L. Chien and C.R.Westgate (Plenum, New York, 1979).

[115] for a review, see, Y. Tokura and N. Nagaosa: Science 288 462(2000); N. Nagaosa, J. Phys. Soc. Jpn. 75, 042001 (2006).

[116] R. Karplus and J. M. Luttinger, Phys. Rev. 95 1154 (1954); M. Onoda and N. Nagaosa, J. Phys. Soc. Jpn. 71 19 (2002).

[117] G. Sundaram and Q. Niu, Phys. Rev. B 59, 14915 (1999).

[118] M. Onoda and N. Nagaosa, J. Phys. Soc. Jpn. 71, 19 (2002).

[119] T. Jungwirth, Qian Niu, and A. H. MacDonald, Phys. Rev. Lett. 88, 207208 (2002);

[120] J. Smit, Physica (Amsterdam) 21, 877 (1955).

[121] P. Nozieres and C. Lewiner, J. Phys. (France) 34, 901 (1973).

[122] A. Crepieux and P. Bruno, Phys. Rev. B 64, 014416 (2001).

[123] L. Berger, Phys. Rev. B 2 (1970) 4559;

[124] Z. Wang, W. Wang, and J. Tang, Appl. Phys. Lett. 83, 518 (2003);

[125] H. Toyosaki, T. Fukumura, Y. Yamada, K. Nakajima, T. Chikyow, T. Hasegawa, H. Koinuma, M. Kawasaki, Nature materials, 3, 221 (2004)

[126] J. S. Higgins, S. R. Shinde, S. B. Ogale, T. Venkatesan, R. L. Greene, Phys. Rev. B 69, 073201 (2004).

[127] P. Matl, N. P. Ong, Y. F. Yan, Y. Q. Li, D. Studebaker, T. Baum and G. Doubinina, Phys. Rev. B 57, 10248 (1998).

[128] W.-L. Lee, S. Watauchi, R. J. Cava and N. P. Ong, Science 303, 1647 (2004).

[129] C. Zeng, Y. Yao, Q. Niu, and H. H. Weitering, Phys. Rev. Lett. 96, 037204 (2006).

[130] Y. G. Yao, L. Kleinman, A. H. MacDonald, J. Sinova, T. Jungwirth, D.-S. Wang, E. Wang, and Q. Niu, Phys. Rev. Lett. 92, 037204 (2004); Z. Fang, N. Nagaosa, K. S. Takahashi, A. Asamitsu, R. Mathieu, T. Ogasawara, H. Yamada, M. Kawasaki, Y. Tokura, and K. Terakura, Science 302, 92 (2003); R. Mathieu, A. Asamitsu, H. Yamada, K. S. Takahashi, M. Kawasaki, Z. Fang, N. Nagaosa, and Y. Tokura, Phys. Rev. Lett. 93, 016602 (2004)

[131] F. Matsukura, H. Ohno, A. Shen, and Y. Sugawara Phys. Rev. B 57, R2037 (1998)

[132] S. U. Yuldashev, H. C. Jeon, H. S. Im, T. W. Kang, S. H. Lee, and J. K. Furdyna, Phys. Rev. B 70, 193203 (2004).

[133] D. Ruzmetov, J. Scherschligt, D. V. Baxter, T. Wojtowicz, X. Liu, Y. Sasaki, J. K. Furdyna, K. M. Yu, and W. Walukiewicz, Phys. Rev. B 69, 155207 (2004).

[134] Wang-Kong Tse and S. Das Sarma Phys. Rev. Lett. 96, 056601 (2006).

[135] M. P. Marder, *Condensed Matter Physics* (John Wiley and Sons, Inc., New York, 2000).

[136] Patrick A. Lee and T. V. Ramakrishnan, Rev. Mod. Phys. 57, 287 (1985).

[137] B. L. Altshuler and A. G. Aronov, *Electron-Electron Interaction in Disordered conductors*, edited by A. L. Efros and M. Pollak (North-Holland, Amsterdam, 1985).

[138] J. Kondo, Prog. Theor. Phys. 32, 37-49 (1964).

[139] A. C. Hewson, The Kondo Problem to Heavy Fermions, (Cambridge University Press, 1997)

[140] T. L. Bell, and K. G. Wilson, Phys. Rev. B 10, 3935 (1974)

[141] Kenneth G. Wilson, Rev. Mod. Phys. 47, 773 (1975)

[142] H. R. Krishna-murthy, J. W. Wilkins, and K. G. Wilson, Phys. Rev. B 21, 1003 (1980), Phys. Rev. B 21, 1044 (1980).

[143] K. Winzer, Solid State Commun. 16, 521 (1975); E.W. Fenton, Phys. Rev. B 7, 3144 (1973); T. Sekitani, M. Naito, and N. Miura, Phys. Rev. B 67, 174503 (2003).

[144] J. Osorio-Guillen, S. Lany, S. V. Barabash, and A. Zunger, Phys. Rev. B 75, 184421 (2007)

[145] Lianfeng Fu, Ph. D thesis, University of Califoria at Davis.